

Restoring vision: Therapy and mechanisms of disease

Inauguraldissertation

zur

Erlangung der Würde eines Doktors der Philosophie

vorgelegt der

Philosophisch-Naturwissenschaftlichen Fakultät

der Universität Basel

von

Dasha Elena Nelidova

von Neuseeland

2020

Originaldokument gespeichert auf dem Dokumentenserver der Universität Basel edoc.unibas.ch

Genehmigt von der Philosophisch-Naturwissenschaftlichen Fakultät auf Antrag von

Prof. Dr. Botond Roska

Prof. Dr. Thomas Mrsic-Flogel

Basel, 19.02.2019

Prof. Dr. Martin Spiess

Table of Contents

Introduction	4
Retina	4
Emerging therapies for retinal degeneration	6
Translational considerations	8
Rationale for work undertaken	9
Chapter 1 - Restoring light sensitivity using tunable near-infrared sensors	10
Abstract	10
Manuscript	11
Chapter 2 - miRNAs 182 and 183 are necessary to maintain adult cone photoreceptor outer segments and visual function	62
Abstract	62
Manuscript	63
Curriculum Vitae	78

Introduction

Retina

The mammalian retina is composed of more than 60 cells types. The retina can be viewed as a parallel image processor (Figure 1). Photoreceptors are natural photon detectors. Photons are captured by outer segments of photoreceptor cells. Rods photoreceptors greatly outnumber cone photoreceptors but are saturated at high daytime light intensities. Cone photoreceptors respond during daylight hours. Both rods and cones respond to light by graded hyperpolarization.

Downstream of photoreceptors retinal neurons are assembled into local circuit modules (Figure 1). Circuit modules tile the retina with characteristic spacing between circuits of the same type (Figure 1b). Retinal circuits carry out a large amount of image processing, computing more than a dozen (Figure 1c) neural representations of the image in parallel. Each local circuit extracts a particular feature from the visual scene such as information about the direction of image motion or perception of image edges.

Parallel processing begins at the first visual synapse. Each cone photoreceptor is connected to around ten types of cone bipolar cells. Bipolar cells can be grouped into two categories: ON bipolar cells depolarize in response to light increments, OFF bipolar cells depolarize to light decrements. Each bipolar cell connects to several types of retinal ganglion cells (RGCs). There are ON, OFF and ON-OFF ganglion cells. Inhibitory interneurons modulate synaptic transmission between photoreceptors and bipolar cells (horizontal cells) and between bipolar cells and ganglion cells

(amacrine cells). Each ganglion cell type incorporates a few bipolar and amacrine cell types in its local retinal circuit. Ganglion cells send visual information to higher brain regions.

In humans, the spatial layout of retinal neurons described above is modified in a specialized retinal area, the fovea. The fovea is critical for visual activities requiring high resolution, such as reading. Cone density is highest at the fovea. Other cell types are pushed to the side, leaving cone outer segments unobstructed. Convergence of foveal cones to ganglion cells is lower in the fovea than in the periphery. At the fovea, ganglion cells connect to single cones. Foveal cones are also in contact with the vitreous body, a clear gel situated between the retina and the lens. To the side of the fovea, an inner limiting membrane (ILM) covers inner retinal neurons. This membrane is not easily penetrated by viral vectors.

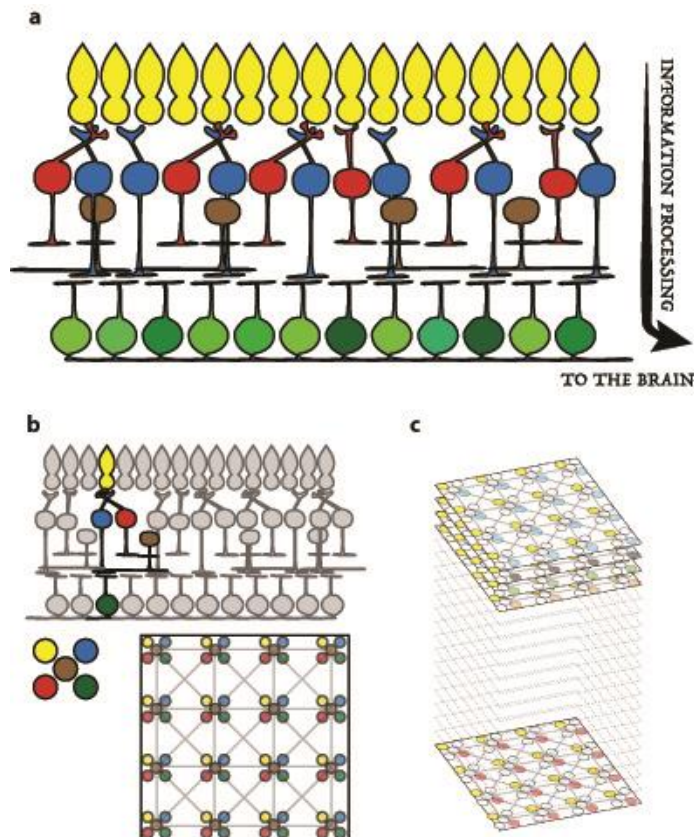


Figure 1. Retinal Overview. **A** General structure of the vertebrate retina. After light detection by photoreceptors (yellow), visual information is passed along to different types of bipolar cells (red and blue). This information is modulated by inhibitory amacrine cells (brown) and is finally transmitted to different classes of ganglion cells (green). Ganglion cells deliver processed visual information to the brain. **B** Each class of ganglion cells transmits a different version of the visual scene to the brain, since it receives information extracted by a specific processing microcircuit, formed by a combination of bipolar and amacrine cells. Microcircuits performing the same processing tile the visual space evenly. **C** Taken together, the ensemble of ~20 different human ganglion cell classes, project to the brain ~20 different version of the visual scene.

Emerging therapies for retinal degeneration

Photoreceptor degeneration, including age-related macular degeneration, is a leading cause of blindness in industrialized countries. There are several emerging therapies for the treatment of photoreceptor degeneration: gene therapy, stem cells, retinal prosthetic devices and optogenetic light sensors. Some take into account the mutated gene and the type of mutation leading to the disease. Others are mutation-independent, concentrating on the structural and functional state of the remaining retinal circuit.

Gene replacement therapy provides a straightforward option for treating inherited retinal degenerative diseases caused by recessive single gene defects. Delivery of a normal copy of the missing gene compensates for loss of gene function. Translational efforts are slowed by the large number of mutations reported in patients with photoreceptor degenerations. Furthermore, dominant mutations require both the correct gene copy and a strategy to eradicate the incorrect version of the gene that antagonizes the wild-type allele. Finally, only some disease-associated genes fit the modest packaging capacities of gene delivery vectors suitable for use in humans.

Stem cell approaches may lead to the generation of new retinal neurons after implantation of neural stem or progenitor cells. Here, appropriate differentiation followed by integration into existing retinal circuits is desirable but to date has been difficult to achieve.

Retinal prosthetic devices operate by injecting charge into excitable tissues in a local area through an array of electrodes. Retinal prosthetic devices enabled low-resolution visual perception in clinical trials with blind human patients. Improving electrode configurations and employing newer semi-conductor and polymer materials may increase resolution.

Optogenetic sensors are single-component light-gated proteins, requiring no externally supplied cofactor. They provide the ability to signal light increments or decrements to photoreceptors that have lost the ability to do so, or else to equip downstream neurons with the ability to respond to light, making them into artificial photoreceptors. A key advantage of optogenetic sensors is the ability to achieve cell-type-specific activation or silencing. Optogenetic tools operate with high spatial and temporal resolution at multiple wavelengths of the visible spectrum. Engineering efforts have led to newer sensors with refined features, however, light intensities required for activation remain high. In most cases of photoreceptor degeneration, the degeneration is incomplete, leading to the presence of light-sensitive and light-insensitive photoreceptor zones next to each other in the same retina. Remaining light-sensitive regions limit the utility of optogenetic therapies since this technology requires bright, visible light that saturates photoreceptors. Nevertheless, relative ease of application is rapidly pushing optogenetics into clinical trials in human patients with advanced disease.

Translational considerations for light sensor therapies

First, since the functional unit of the retina is a mosaic of cell types assembled into local circuits, cell-type-specific interventions are preferable for vision restoration. To preserve normal retinal information processing foveal cones should be stimulated. If cones are degenerated, downstream retinal neurons may be considered. Ultimately, strategy is dictated by the state of the retina in a given patient at a given time. The state of the retina of a particular patient is characterized during the course of clinical investigation. Targeting the right neuron still poses practical difficulties, particularly when moving from mouse to non-human primate to human studies.

Second, it is necessary to optimize therapeutic agent delivery. The most commonly used approach to deliver transgenes is intraocular injection of adeno-associated virus (AAV). Intraocular AAVs were shown to be safe in multiple clinical trials. Viruses may be engineered to improve properties by directed evolution or rational mutagenesis. In general, permissive AAV serotypes are preferred. Specificity of expression is achieved via a cell type specific promoter.

Third, in primates, the inner limiting membrane acts as a strong barrier to AAV diffusion. Removal of the inner limiting membrane may be attempted surgically or non-viral gene transfer may be considered. Currently, non-viral vectors still lag behind viral vectors in terms of transfection efficiencies and ability to generate long-term expression. An alternative approach is to perform subretinal injections of virus. Subretinal injection deposits a large number of AAV particles next to the photoreceptor layer. If foveal cones are to be transduced, virus may be injected intravitreally, though a significant dilution will occur due to the large size of the vitreous body.

Rationale for work undertaken

The retina is a complex sensory structure. Blindness often results from dysfunction of this neural network. At present, degenerative diseases of the retina remain incurable. Patients with these conditions usually suffer progressive visual decline resulting from the ongoing dysfunction or loss of retinal neurons. Retinal photoreceptor degeneration is particularly common. No conventional medical or surgical treatment has the ability to restore high acuity vision. In light of the fact that most of patients seeking visual restoration do have some degree of remaining visual function, a major challenge is the compatibility of therapy with remaining vision. This question is addressed in Chapter 1.

Image-forming vision relies on photoreceptors that detect light using their outer segments. Outer segments are organelles composed of stacks of membrane disks that host photopigment. Photoreceptor dysfunction arises when photoreceptor outer segments degenerate. Despite outer segment loss, light insensitive photoreceptor cell bodies may persist for years or decades in some patients. Additionally, downstream neural circuitry is often sufficiently intact to make prospective sight restoring therapies feasible, if impairments of photoreceptor structure or function can be addressed. One of the central goals of translational retinal research is to develop strategies to repair the retina, including outer segments, yet outer segment formation and maintenance is a process that is not well understood. Understanding this process requires insight into molecular pathways that control cell identity. This question is addressed in Chapter 2.

Chapter 1

Restoring light sensitivity using tunable near-infrared sensors

Dasha Nelidova, Rei K. Morikawa, Cameron S. Cowan, Zoltan Raics, David Goldblum,
Hendrik Scholl, Tamas Szikra, Arnold Szabo, Daniel Hillier, Botond Roska

In Press. Science (April 2020)

Abstract

Enabling near-infrared light sensitivity in a blind human retina may supplement or restore visual function in patients with regional retinal degeneration. We induced near-infrared light sensitivity using gold nanorods bound to temperature-sensitive engineered transient receptor potential (TRP) channels. We expressed mammalian or snake TRP channels in light-insensitive retinal cones in a mouse model of retinal degeneration. Near-infrared stimulation increased activity in cones, ganglion cell layer neurons and cortical neurons, and enabled mice to perform a learned, light-driven behavior. We tuned responses to different wavelengths by using nanorods with different lengths, and to different radiant powers by using engineered channels with different temperature thresholds. We targeted TRP channels to human retinas, which allowed the activation of different cell types by near-infrared light, post-mortem.

Photoreceptor degeneration, including age-related macular degeneration and retinitis pigmentosa, is the leading cause of blindness in industrialized countries. When cone photoreceptors lose light sensitivity, high-resolution vision is affected and it is difficult to carry out activities of daily living. In most cases, photoreceptor degeneration is incomplete, leading to the presence of light-sensitive and light-insensitive photoreceptor zones next to each other in the same retina. Remaining light-sensitive regions limit the utility of optogenetic (1) or light-switch (2) therapies because these technologies require bright, visible light that saturates photoreceptors.

Enabling the detection of near-infrared (NIR) light at wavelengths (>900 nm) outside the human visible spectrum (390–700 nm) could provide a way of supplementing or restoring light sensitivity in the affected retinal region, without interfering with remaining vision. Currently, there is no technology that would allow the induction of NIR sensitivity in a blind retina.

A few species such as boas, pythons and pit vipers can detect infrared light (1–30 μm) using temperature-sensitive TRP cation channels expressed in a specialized organ (3). Thermal and visual images superimpose within the snake's brain (4), presumably enabling the snake to react to the environment with greater precision than with the use of a single image only. TRP channels could potentially be targeted to retinal cell types to make them sensitive to infrared radiation. However, heat transfer to ectopically-expressed TRP channels via direct NIR illumination is inefficient, requiring high intensities that would damage the retina.

To develop a more efficient NIR light detector for retinal cell types, we engineered a two-

component system consisting of a genetic and a nanomaterial component (Fig. 1). The genetic component consisted of temperature-sensitive TRP channels, engineered to incorporate an extracellular epitope recognizable by a specific antibody (Fig. 1A) (5). The nanomaterial component consisted of gold nanorods conjugated to an antibody against the epitope (Fig. 1A) (6). This system uses surface plasmon resonance for heat transfer (7): gold nanorods capture NIR light at their resonant wavelength and produce heat, which is harnessed to open TRP channels in the proximity of the nanorods. The epitope ensures nanorod binding to engineered rather than native TRP channels, because some TRP channels are expressed in the retina (8, 9).

We developed a system based on rat TRPV1 channels and gold nanorods with absorption maxima (λ_{abs}) at 915 nm. 915 nm was selected to ensure low water absorption. We inserted a 6x-His epitope tag in the middle of the first TRPV1 extracellular loop (Fig. 1, C and D), after amino acid 459 or 465 (Fig. S1). Analysis of TRPV1 structure suggested that insertion at these sites would not disrupt protein function.

To measure if tagged channels are functional, we performed whole-cell voltage clamp in HEK cells expressing TRPV1.459-6x-His, TRPV1.465-6x-His or untagged TRPV1 while activating the channels by TRPV1 agonist capsaicin. The sizes of evoked currents were similar between TRPV1.465-6x-His and TRPV1 (Table S1A), but less in TRPV1.459-6x-His (Table S1B and Fig. S2). Therefore, we used TRPV1.465-6x-His (abbreviated as rTRPV1) in subsequent experiments.

We targeted rTRPV1 to cone photoreceptors of *Pde6b*^{rd1} (known as rd1) mice through

subretinal injection of adeno-associated virus (AAV), using a photoreceptor-specific promoter (mCar) to restrict expression (Fig. 1E). Rd1 mice have severe photoreceptor degeneration, with complete loss of rods and dysfunctional, light-insensitive cone photoreceptors by four weeks of age (Fig. 1B) (10). $55 \pm 10\%$ of rd1 cones expressed rTRPV1 in the cell membrane (Table S1C and Fig. 1F). $98 \pm 1.6\%$ of rTRPV1 positive cells were cones (Table S1D). rTRPV1 positive cones expressed the 6x-His tag (Table S1E and Fig. 1, E and F).

To measure if NIR light drives responses in rd1 retinas, we performed two-photon calcium imaging of individual cone cell bodies and axon terminals as well as ganglion cell bodies in wholemount P56-P72 retinas in two conditions: first, rTRPV1 with nanorods ($\lambda_{\text{abs}} = 915 \text{ nm}$) and second, rTRPV1 without nanorods. To measure if NIR light affects normal cones, we performed two-photon calcium imaging of cone axon terminals in wholemount wild-type retinas stimulating cones with NIR (915 nm) and/or visible light. To detect calcium signals in cones, we genetically targeted the calcium indicator GCaMP6s via an AAV that expresses GCaMP6s under a cone-specific promoter (11). For ganglion cells, we used the organic calcium sensor Oregon Green 488 BAPTA-1 (OGB-1).

rTRPV1 expressing rd1 cones showed 915 nm light (“NIR light”) evoked increases of calcium signal in the presence of nanorods (“NIR cone response”) (Fig. 1, G to I). NIR cone response was of opposite polarity compared to the visible light response of wild-type cones (Fig. 1G). Polarity reversal was due to cation selectivity of rTRPV1. NIR cone response was similar in size compared to the visible light response of wild-type cones (Table S1, F and G). NIR light neither activated wild-type cones nor affected wild-type cone visible light responses (Fig. S3). rTRPV1 expressing cones without nanorods did not react to light (Fig. 1, G to I). In the

presence of nanorods, NIR light also induced responses in neurons of the ganglion cell layer (GCL) (Fig. S4). In all subsequent experiments, we used both the TRP channel and the nanorod component (“NIR sensor”), while control mice were uninjected rd1 mice.

To assess if NIR light-induced retinal activity propagates to higher visual centers, we generated rd1 mice with targeted GCaMP6s expression in layer 4 of the primary visual cortex (V1). Layer 4 receives feedforward connections from the lateral geniculate nucleus. We performed two-photon calcium imaging *in vivo* in P51-P83 animals, recording layer 4 activity at single cell resolution during NIR light stimulation of the eye (Fig. 2A). In NIR sensor injected animals, cortical neurons showed NIR light-evoked increases of calcium signal (Fig. 2B), which were light intensity dependent (Fig. 2C and Fig. S5). Neuronal activation was greater in NIR sensor injected animals than in controls (Table S1H and Fig. 2C).

Nanorod absorption spectra can be wavelength-tuned by varying nanorod aspect ratios (length to width ratios) (Fig. 2E and Fig. S6). To test if the action spectra of neuronal activity can also be tuned we selected a second type of gold nanorod with peak absorption at 980 nm (aspect ratio 5.5) and compared to nanorods with peak absorption at 915 nm (aspect ratio 4.0). Both types were paired to rTRPV1. For each nanorod type, we performed layer 4 cortical calcium imaging in P51-P71 rd1 mice twice: once with 980 nm stimulation of the eye, and once with 915 nm stimulation. To classify cortical neurons as 980 nm or 915 nm responsive, we computed a wavelength preference index (WPI) for each NIR light responsive neuron. We found a preference for 980 nm over 915 nm light using nanorods tuned to 980 nm (Table S1I and Fig. 2H and Fig. S7). Similarly, in animals with nanorods tuned to 915 nm, more cortical neurons preferred 915 nm over 980 nm light (Table S1J and Fig. 2H and Fig. S7).

Next, we asked if molecular components can be tuned to increase sensitivity. A variety of TRPA1 channels also serve as heat sensors. TRPA1 from the Texas rat snake (*Elaphe obsoleta lindheimeri*) is activated at a lower temperature than rTRPV1 (3). To determine the suitability of snake TRPA1 as a NIR sensor component, we first engineered TRPA1 to express the peptide epitope tag Ollas (12) within the first or second extracellular loop. Anti-Ollas antibodies show improved immunodetection compared to anti-6x-His and other antibodies for conventional epitope tags (12). To identify loop domains, first, we determined the location of extracellular loop domains of human TRPA1 from its cryo-EM structure (13). Subsequently, we identified potential loop domains of snake TRPA1 after pairwise sequence alignment (14) between human and snake sequences. Ollas was placed after amino acid 755 or 758, corresponding to the first loop, or after amino acid 824, corresponding to the second loop (Fig. S8).

We performed whole-cell voltage clamp in HEK cells expressing TRPA1.755-Ollas, TRPA1.758-Ollas, TRPA1.824-Ollas or untagged TRPA1 while activating the channels by TRPA1 agonist allyl isothiocyanate (AITC). The sizes of evoked currents were similar between TRPA1.755-Ollas and TRPA1 (Table S1K) and between TRPA1.824-Ollas and TRPA1 (Table S1L and Fig. S9). Currents were undetectable for TRPA1.758-Ollas (Fig. S9B). We used TRPA1.755-Ollas (abbreviated as sTRPA1) in subsequent experiments.

We targeted sTRPA1 to cone photoreceptors of rd1 mice using the same AAV-based approach as for rTRPV1 (Fig. 3). To activate the channel, nanorods ($\lambda_{\text{abs}} = 915 \text{ nm}$) were conjugated to anti-Ollas antibodies. $50 \pm 13\%$ of rd1 cone photoreceptors expressed sTRPA1 in the cell membrane (Table S1M and Fig. 3C). $99 \pm 0.8\%$ of Ollas positive cells were cones (Table S1N).

To compare rTRPV1 and sTRPA1 sensitivities, we performed behavioral tests in NIR sensor injected P56-P73 rd1 mice. NIR light of two different intensities cued delayed water appearance for water-restricted, head-fixed animals (Fig. 3D). We evaluated anticipatory lick rates, defined as lick signal after a NIR light flash but before the appearance of water. To measure if NIR light affects the behavior of wild-type animals, we trained wild-type mice with NIR (915 nm or 980 nm) and/or visible light (Fig. S10A). NIR sensor injected mice learned to associate NIR light with water within four days. At the lower NIR intensity, anticipatory lick rates were similar between control mice and mice with rTRPV1 (Table S1O), but higher for mice injected with sTRPA1 (Table S1P and Fig. 3, E and F). At the higher NIR intensity, rTRPV1 led to higher lick rates compared to control mice (Table S1Q), but lower than with sTRPA1 (Table S1R and Fig. 3, E and F). Behavioral performance of rTRPV1 and sTRPA1 mice was similar to wild-type mice trained for four days using visible light (Table S1, S and T and Fig. S10). NIR light neither elicited behavioral responses in wild-type mice nor affected wild-type behavioral responses to visible light (Fig. S10C).

To test safety aspects of inducing NIR light sensitivity, we first evaluated the effect of prolonged NIR light exposure on wild-type retinas by immunostaining. NIR light neither activated microglia nor reduced retinal layer thickness, opsin density or cone density (Fig. S11). Second, we tested nanorod biocompatibility with the rd1 retina 80 and 100 days after subretinal injection by immunostaining. Nanorods neither activated microglia, increased apoptosis nor reduced retinal layer thickness (Fig. S12).

Finally, we sought to induce NIR light sensitivity in blind human retinas (Fig. 4). We targeted

rTRPV1 to adult human *ex vivo* retinal explants, in culture for eight weeks post-mortem (Fig. 4B and Fig. S13). Retinas lose normal light-evoked activity within 24 hours of isolation (15). Using AAV delivery and a CAG promoter, we transduced 2477 ± 889 photoreceptors per mm^2 of human retina (mean \pm s.d, $n = 3$ explants) with rTRPV1 (Fig. 4C). $94.5 \pm 4.2\%$ of rTRPV1 positive cells were photoreceptors (Table S1U and Fig. 4D). To measure if NIR light drives responses in the human retina, we deposited nanorods ($\lambda_{\text{abs}} = 915$ nm) over the photoreceptor side. To record calcium signals, we used the fluorescent calcium dye OGB-1 (16, 17). We then performed two-photon calcium imaging of individual neurons in the outer nuclear layer (ONL), inner nuclear layer (INL) and GCL (Fig. 4A). We observed NIR light-induced activation of different human retinal cell classes (Fig. 4, F to H). Most photoreceptors (73%) showed NIR light-evoked increases of calcium signal (Fig. 4H). Some photoreceptors (27%) showed decreases of calcium signal, likely reflecting horizontal cell feedback to NIR light-insensitive photoreceptors (Fig. 4H). In neurons of the INL and GCL, we observed both increases and decreases in the calcium signal, indicating activation of excitatory and inhibitory retinal pathways (Fig. 4H). More cells responded in the GCL than in the ONL, reflecting convergent retinal circuit organization (Fig. 4G). Sizes of light-evoked calcium responses were comparable to published reports (16, 17).

Here, we described an approach to enable NIR light sensitivity in blind retinas, designed to be compatible with remaining vision (Supplementary Text). We used gold nanorods coupled to temperature-sensitive engineered TRP channels to induce NIR light sensitivity in remaining photoreceptor cell bodies of blind mice and in *ex vivo* human retinas. In mice, NIR light-sensitized photoreceptors activated cortical visual circuits and enabled behavioral responses. By means of distinct nanorods, epitope tags and TRP channel types, we tuned NIR responses to different wavelengths and to different radiant powers. In the human retina, we reactivated light responses in

photoreceptors, and their retinal circuits eight weeks post-mortem. Our recordings of NIR light-evoked activity in the post-mortem human retina provide not only proof-of-principle for translation, but also a model with which the function of human retinal cell types and circuits can be studied.

References and Notes:

1. J. A. Sahel, B. Roska, Gene therapy for blindness. *Annu Rev Neurosci* **36**, 467-488 (2013).
2. I. Tochitsky, M. A. Kienzler, E. Isacoff, R. H. Kramer, Restoring Vision to the Blind with Chemical Photoswitches. *Chem Rev* **118**, 10748-10773 (2018).
3. E. O. Gracheva *et al.*, Molecular basis of infrared detection by snakes. *Nature* **464**, 1006-1011 (2010).
4. E. A. Newman, P. H. Hartline, Integration of visual and infrared information in bimodal neurons in the rattlesnake optic tectum. *Science* **213**, 789-791 (1981).
5. S. A. Stanley *et al.*, Radio-wave heating of iron oxide nanoparticles can regulate plasma glucose in mice. *Science* **336**, 604-608 (2012).
6. P. P. Joshi, S. J. Yoon, W. G. Hardin, S. Emelianov, K. V. Sokolov, Conjugation of antibodies to gold nanorods through Fc portion: synthesis and molecular specific imaging. *Bioconjug Chem* **24**, 878-888 (2013).
7. Z. Qin, J. C. Bischof, Thermophysical and biological responses of gold nanoparticle laser heating. *Chem Soc Rev* **41**, 1191-1217 (2012).
8. M. Lakk *et al.*, Polymodal TRPV1 and TRPV4 Sensors Colocalize but Do Not Functionally Interact in a Subpopulation of Mouse Retinal Ganglion Cells. *Front Cell Neurosci* **12**, 353 (2018).

9. D. A. Ryskamp, S. Redmon, A. O. Jo, D. Krizaj, TRPV1 and Endocannabinoids: Emerging Molecular Signals that Modulate Mammalian Vision. *Cells* **3**, 914-938 (2014).
10. V. Busskamp *et al.*, Genetic reactivation of cone photoreceptors restores visual responses in retinitis pigmentosa. *Science* **329**, 413-417 (2010).
11. J. Juttner *et al.*, Targeting neuronal and glial cell types with synthetic promoter AAVs in mice, non-human primates and humans. *Nat Neurosci* **22**, 1345-1356 (2019).
12. S. H. Park *et al.*, Generation and application of new rat monoclonal antibodies against synthetic FLAG and OLLAS tags for improved immunodetection. *J Immunol Methods* **331**, 27-38 (2008).
13. C. E. Paulsen, J. P. Armache, Y. Gao, Y. Cheng, D. Julius, Structure of the TRPA1 ion channel suggests regulatory mechanisms. *Nature* **520**, 511-517 (2015).
14. L. Zimmermann *et al.*, A Completely Reimplemented MPI Bioinformatics Toolkit with a New HHpred Server at its Core. *J Mol Biol* **430**, 2237-2243 (2018).
15. C. S. Cowan *et al.*, Cell types of the human retina and its organoids at single-cell resolution: developmental convergence, transcriptomic identity, and disease map. *bioRxiv*, 703348 (2019).
16. K. L. Briggman, T. Euler, Bulk electroporation and population calcium imaging in the adult mammalian retina. *J Neurophysiol* **105**, 2601-2609 (2011).
17. T. Baden *et al.*, The functional diversity of retinal ganglion cells in the mouse. *Nature* **529**, 345-350 (2016).
18. M. Liao, E. Cao, D. Julius, Y. Cheng, Structure of the TRPV1 ion channel determined by electron cryo-microscopy. *Nature* **504**, 107-112 (2013).

19. T. Cronin *et al.*, Efficient transduction and optogenetic stimulation of retinal bipolar cells by a synthetic adeno-associated virus capsid and promoter. *EMBO Mol Med* **6**, 1175-1190 (2014).
20. K. Y. Chan *et al.*, Engineered AAVs for efficient noninvasive gene delivery to the central and peripheral nervous systems. *Nat Neurosci* **20**, 1172-1179 (2017).
21. D. Hillier *et al.*, Causal evidence for retina-dependent and -independent visual motion computations in mouse cortex. *Nat Neurosci* **20**, 960-968 (2017).
22. J. Yao, B. Liu, F. Qin, Rapid temperature jump by infrared diode laser irradiation for patch-clamp studies. *Biophys J* **96**, 3611-3619 (2009).
23. A. Drinnenberg *et al.*, How Diverse Retinal Functions Arise from Feedback at the First Visual Synapse. *Neuron* **99**, 117-134 e111 (2018).
24. A. Giovannucci *et al.*, CaImAn an open source tool for scalable calcium imaging data analysis. *Elife* **8**, (2019).
25. Z. V. Guo *et al.*, Procedures for behavioral experiments in head-fixed mice. *PLoS One* **9**, e88678 (2014).
26. F. C. Delori, R. H. Webb, D. H. Sliney, I. American National Standards, Maximum permissible exposures for ocular safety (ANSI 2000), with emphasis on ophthalmic devices. *J Opt Soc Am A Opt Image Sci Vis* **24**, 1250-1265 (2007).
27. E. O. Gracheva *et al.*, Ganglion-specific splicing of TRPV1 underlies infrared sensation in vampire bats. *Nature* **476**, 88-91 (2011).
28. S. N. Leow *et al.*, Safety and Efficacy of Human Wharton's Jelly-Derived Mesenchymal Stem Cells Therapy for Retinal Degeneration. *PLoS One* **10**, e0128973 (2015).

29. H. B. Song *et al.*, Intraocular application of gold nanodisks optically tuned for optical coherence tomography: inhibitory effect on retinal neovascularization without unbearable toxicity. *Nanomedicine* **13**, 1901-1911 (2017).
30. J. H. Kim *et al.*, The inhibition of retinal neovascularization by gold nanoparticles via suppression of VEGFR-2 activation. *Biomaterials* **32**, 1865-1871 (2011).
31. Y. J. Roh, C. R. Rho, W. K. Cho, S. Kang, The Antiangiogenic Effects of Gold Nanoparticles on Experimental Choroidal Neovascularization in Mice. *Invest Ophthalmol Vis Sci* **57**, 6561-6567 (2016).
32. D. H. Jo *et al.*, Nanoparticle-protein complexes mimicking corona formation in ocular environment. *Biomaterials* **109**, 23-31 (2016).
33. S. J. Bakri, J. S. Pulido, P. Mukherjee, R. J. Marler, D. Mukhopadhyay, Absence of histologic retinal toxicity of intravitreal nanogold in a rabbit model. *Retina* **28**, 147-149 (2008).
34. M. Zhou *et al.*, Minute synthesis of extremely stable gold nanoparticles. *Nanotechnology* **20**, (2009).
35. W. Huang, S. M. Chen, Y. S. Liu, H. Y. Fu, G. Z. Wu, The controlled synthesis of stable gold nanoparticles in quaternary ammonium ionic liquids by simple heating. *Nanotechnology* **22**, (2011).
36. A. Gupta *et al.*, Ultrastable and Biofunctionalizable Gold Nanoparticles. *Acs Appl Mater Inter* **8**, 14096-14101 (2016).
37. L. D. Huang *et al.*, Fabrication of Highly Stable Glyco-Gold Nanoparticles and Development of a Glyco-Gold Nanoparticle-Based Oriented Immobilized Antibody Microarray for Lectin (GOAL) Assay. *Chem-Eur J* **21**, 3956-3967 (2015).

38. K. Rahme *et al.*, Highly stable PEGylated gold nanoparticles in water: applications in biology and catalysis. *Rsc Adv* **3**, 21016-21024 (2013).
39. F. Masse *et al.*, Synthesis of Ultrastable Gold Nanoparticles as a New Drug Delivery System. *Molecules* **24**, (2019).
40. J. Deka *et al.*, Surface passivation improves the synthesis of highly stable and specific DNA-functionalized gold nanoparticles with variable DNA density. *ACS Appl Mater Interfaces* **7**, 7033-7040 (2015).

Acknowledgments: We thank organ and tissue donors and their families for their generous contributions to science; T. Vögele, J. Sprachta and P. Blaschke for organizing organ donations; H. Gut and R. Bunker for advice on TRP channel design; J. Jüttner, C. Patino-Alvarez, Ö. Keles, N. Ledergerber for technical assistance; J. Krol for advice on molecular assays; E. Macé and F. Esposti for assistance with recordings; P. Argast and P. Buchmann for electrical and mechanical engineering in support of the experiments; K. Franke, T. Euler and Z. Zhao for advice on loading of calcium indicators by electroporation; F. Müller for statistical advice; W. Baehr for sharing of antibodies; D. Dalkara, C. Cepko and E. Bamberg for plasmids; FMI and NIBR core facilities for their support, especially the microscopy facility, in particular C. Genoud and A. Graff-Meyer for electron microscopy; V. Juvin from SciArtWork for illustrations; M. Munz and T. Rodrigues for commenting on the manuscript. **Funding:** This work was supported by a Swiss National Science Foundation Synergia grant, a European Research Council advanced grant, a Louis-Jeantet Foundation award, a Swiss National Science Foundation grant, the NCCR ‘Molecular Systems Engineering’ network, a private donation from Lynn and Diana Lady Dougan to B.R., a NKFIH 129120 and 2017-1.2.1-NKP-2017-00002 grants to D.H., a Swiss Academy of Medical Sciences Fellowship to D.N. **Author contributions:** D.N. designed and performed experiments and wrote the paper. C.S.C. performed human retina recordings, R.K.M. performed mouse photoreceptor recordings, Z.R. wrote software, D.G., H.S., and A.S. contributed to human retina experiments, T.S. performed HEK cell recordings, D.H. performed cortical recordings and analyzed data. B.R. designed experiments and wrote the paper. **Competing interests:** D.N. and B.R. have a patent application on NIR sensors. **Data and materials availability:** TRP plasmid materials are available from B. Roska under an agreement with the Institute of Molecular and Clinical Ophthalmology Basel. All data are available in the manuscript or the supplementary materials.

Fig. 1. Near-infrared light responses in mouse cone photoreceptors. **(A)** Components of the NIR light sensor. Engineered TRP channels (blue) express protein epitope tags (orange) in extracellular domains and bind antibody (black) conjugated gold nanorods (gold). **(B)** Left, healthy retina, photons are captured by outer segments (OS) of photoreceptor cells. Right, retinal degeneration, loss of OS and blindness. In the rd1 mouse model of degeneration (*Pde6b*^{rd1}) rod cell bodies are lost but cone cell bodies persist. ONL, outer nuclear layer; INL, inner nuclear layer; GCL, ganglion cell layer. **(C, D)** Structure of TRPV1.465-6x-His (rTRPV1) channel. **(C)** Top view. Orange arrows, 6x-His epitope tag in each subunit of the TRPV1 tetramer. Four subunits are in different colors (yellow, blue, grey, green). Red asterisk, channel pore. **(D)** Right, side view. Left, 6x-His epitope tag (orange) within the first extracellular loop of the blue subunit is enlarged. **(E)** Top row, top views of rd1 retinas transduced with both rTRPV1 and nanorods, immunostained for TRPV1 (left, blue), 6x-His (middle, orange), and merging the two (right). Grey, Hoechst nuclear stain. Bottom row, cross-sections of the retinas shown in top. Scale bars 25 μm . **(F)** Number of rTRPV1 (blue) and 6x-His positive (orange) cones per mm^2 in rd1 retinas transduced with both rTRPV1 and nanorods ($n = 5$ mice) or in control, uninjected rd1 retinas ($n = 5$ mice). Dotted arrow, maximum cone density in rd1 mice at postnatal day 70 (10). Each data point is collected from a different region of a retina (3 regions per retina) **(G)** Example calcium responses (mean $\Delta F/F$, 2-3 repetitions) recorded from cone axon terminals in P56-P71 rd1 mice transduced with rTRPV1 and nanorods (left, λ_{abs} nanorod = 915 nm), rd1 mice transduced with rTRPV1 only (middle) or in wild-type mice (right). TRP, $n = 4$ mice; wild-type, $n = 3$ mice. Stimulus, full-field NIR light (915 nm, \log_{10} light intensity = 18.9, left and middle) or visible light (405 nm, \log_{10} light intensity = 14, right). Black bars (2 s) and arrows (100 ms), stimulus timing. Two-photon images of GCaMP6s-expressing cone axon terminals (white circles), left of the response curves. Scale bar 5 μm . White asterisks, cell bodies. **(H)** Cumulative frequency of responding rTRPV1 transduced rd1 cones with

(black) and without (grey) nanorods ($\lambda_{\text{abs}} = 915 \text{ nm}$). **(I)** Cone response amplitudes ($\Delta F/F$). Light intensities as in G. x/y cones refers to x responding cones of the y measured.

Fig. 2. Near-infrared light responses in mouse primary visual cortex. **(A)** Schematic of the experiments in the primary visual cortex (V1). Cortical neuron calcium responses to 100 ms full-field NIR light stimulation of the contralateral eye were recorded in P51-P83 rd1 mice. **(B)** Example calcium responses (mean $\Delta F/F$, 5 repetitions) to 915 nm light stimulation recorded in rd1 mice transduced with rTRPV1 and nanorods (left, $\lambda_{\text{abs}} = 915$ nm, $n = 3$ mice) and in control, uninjected rd1 mice (right, $n = 5$ mice). Vertical lines at bottom, stimulus timing. Two-photon images of GCaMP6s-expressing neuronal cell bodies in layer 4 of V1 (white circles), left of the response curves. Scale bar 25 μm . **(C)** Cumulative frequency of responding cortical neurons in mice transduced with both rTRPV1 and nanorods (black, $\lambda_{\text{abs}} = 915$ nm) and in control, uninjected mice (grey). **(D)** Cortical neuron response amplitudes ($\Delta F/F$). Log_{10} light intensity = 18.3. x/y neurons refers to x responding neurons of the y measured. **(E)** Morphology of nanorods tuned to 915 nm (left) and 980 nm (right) measured by transmission electron microscopy. **(F)** Schematic showing nanorod absorption spectra relative to visual pigment of the human retina. **(G)** Example cortical calcium responses (mean $\Delta F/F$, 5 repetitions) to 915 nm and 980 nm light stimulation (log_{10} light intensity = 18.3). Left, mice transduced with rTRPV1 and nanorods with $\lambda_{\text{abs}} = 915$ nm ($n = 3$ mice). Right, mice transduced with rTRPV1 and nanorods with $\lambda_{\text{abs}} = 980$ nm ($n = 4$ mice). Arrows indicate stimulus timing. Two-photon images of GCaMP6s-expressing neuronal cell bodies in layer 4 of V1 (white circles), left of the response curves. Scale bar 25 μm . **(H)** Frequency of cortical neurons as a function of the wavelength preference index (WPI) in mice transduced with rTRPV1 and nanorods with $\lambda_{\text{abs}} = 915$ nm (pink) or nanorods with $\lambda_{\text{abs}} = 980$ nm (grey). For nanorods with $\lambda_{\text{abs}} = 915$ nm, larger fraction of 915 nm (WPI < 0) over 980 nm (WPI > 0) light preferring neurons. For nanorods $\lambda_{\text{abs}} = 980$ nm, larger fraction of 980 nm (WPI > 0) over 915 nm (WPI < 0) light preferring neurons. Light intensities as in G.

Fig. 3. Near-infrared light guided mouse behavior. **(A)** Schematic showing location of TRP channel expressing, infrared-sensitive pit organ. Information is overlaid in the optic tectum. **(B)** Expression of sTRPA1 in cones of rd1 mice. Top, top view of a retina transduced with both sTRPA1 and nanorods, immunostained for Ollas (orange), overlaid with Hoechst nuclear stain (grey). Bottom, cross-section of the retina shown in top. Scale bars 25 μm . **(C)** Number of Ollas (orange) positive cones per mm^2 in rd1 retinas transduced with both sTRPA1 and nanorods ($n = 5$ mice) or in control, uninjected rd1 retinas ($n = 5$ mice). Dotted arrow, maximum cone density in rd1 mice at postnatal day 70 (10). Each data point is collected from a different region of a retina (3 regions per retina). **(D)** Schematic of behavioral task. NIR full-field stimulation of one eye (915 nm, 200 ms) cues water presentation for head-fixed, water-restricted P56-P73 rd1 animals. Mice respond by licking before (anticipation) or after the appearance of water. **(E)** Lick response heat maps. Rows, responses of different mice. Columns, responses in 100 ms time bins. Top, rd1 mice transduced with both sTRPA1 and nanorods ($\lambda_{\text{abs}} = 915$ nm, $n = 9$ mice). Middle, rd1 mice transduced with both rTRPV1 and nanorods ($\lambda_{\text{abs}} = 915$ nm, $n = 9$ mice). Bottom, control, uninjected rd1 mice ($n = 10$ mice). Left, stimulus \log_{10} light intensity = 17.9. Right, stimulus \log_{10} light intensity = 18.3. **(F)** Mean anticipatory lick rates quantified from (E) as a function of light intensity. Error bars, s.e.m.

Fig 4. Near-infrared light responses in the *ex vivo* human retina. **(A)** Schematic of a human retinal explant eight weeks post-mortem. Long-term culture leads to loss of outer segments and no light responses. ONL, outer nuclear layer; INL, inner nuclear layer; GCL, ganglion cell layer. **(B)** Top, top view of a human retina transduced with both rTRPV1 and nanorods, immunostained for TRPV1 (blue), overlaid with Hoechst nuclear stain (grey). Bottom, cross-section of the retina shown in top. Scale bars 10 μm . **(C)** Number of rTRPV1 (blue) positive photoreceptors per mm^2 in human retinas transduced with both rTRPV1 and nanorods or in control, untransduced human retinas. Each data point is collected from a different region of a retina (5 regions per retina). **(D)** Distribution of rTRPV1 positive cells across retinal layers. **(E)** Scanning electron microscopy image of gold nanorods bound to a rTRPV1 transduced human retina. Scale bar 1 μm . Inset, transmission electron microscopy image showing an anti-6x-His antibody touching a gold nanorod with its Fc domain. Scale bar 20 nm. **(F)** Example calcium responses recorded from human retinal neurons in ONL, INL and GCL in response to full-field, NIR light. Vertical lines at bottom, stimulus (915 nm, 100 ms) timing. Two-photon images of Oregon Green 488 BAPTA-1 (OGB-1) filled cell bodies (white circles), left of the response curves. Scale bar 10 μm . **(G)** Cumulative frequency of responding neurons in different layers of human retinas transduced with both rTRPV1 and nanorods ($\lambda_{\text{abs}} = 915 \text{ nm}$) or in control, untransduced human retinas. **(H)** Response amplitudes ($\Delta F/F$) by retinal layer. Increase (\uparrow) and decrease (\downarrow) of calcium signal are shown separately. x/y neurons refers to x responding neurons of the y measured. Log_{10} light intensity = 18.9.

Figure 1

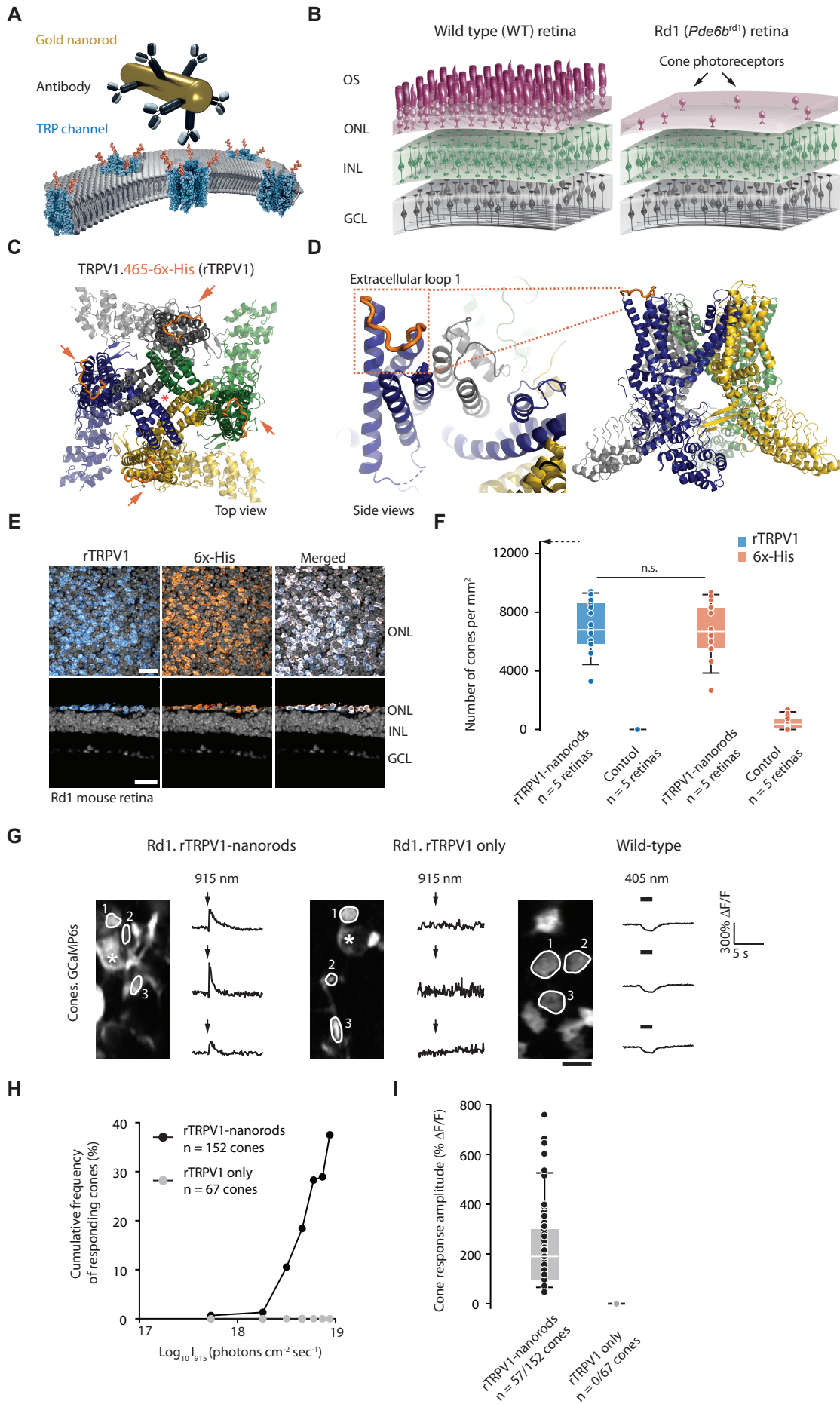


Figure 2

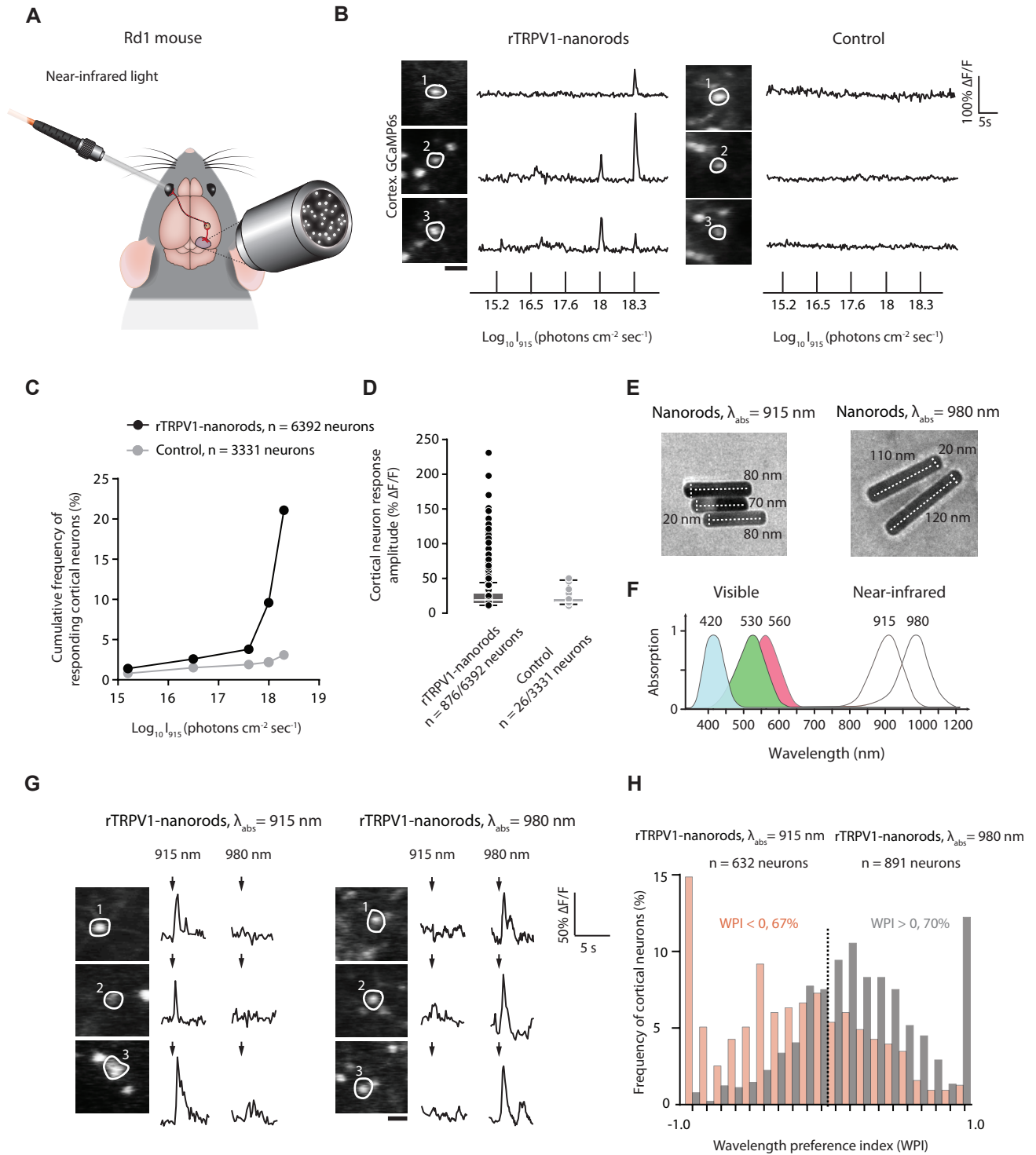


Figure 3

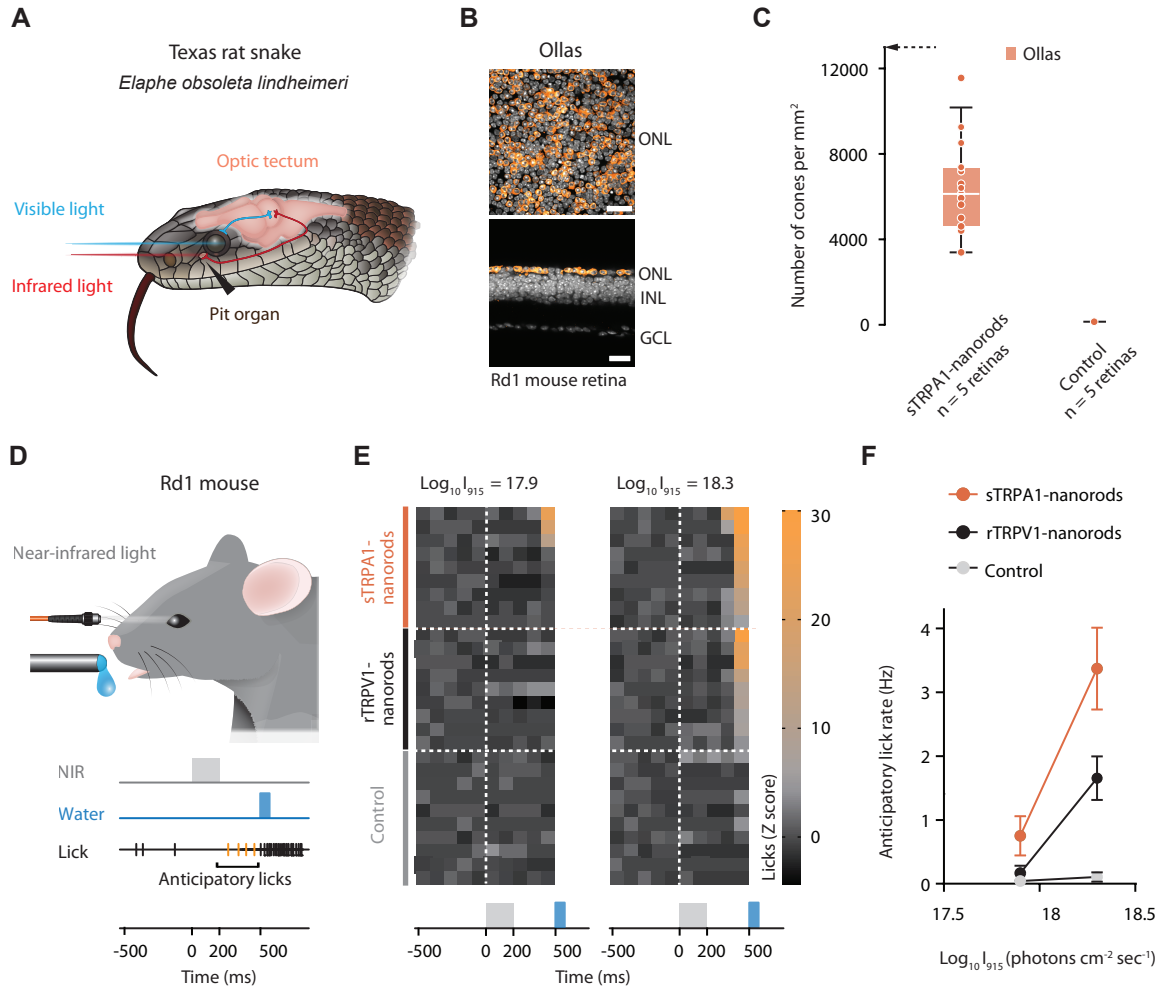
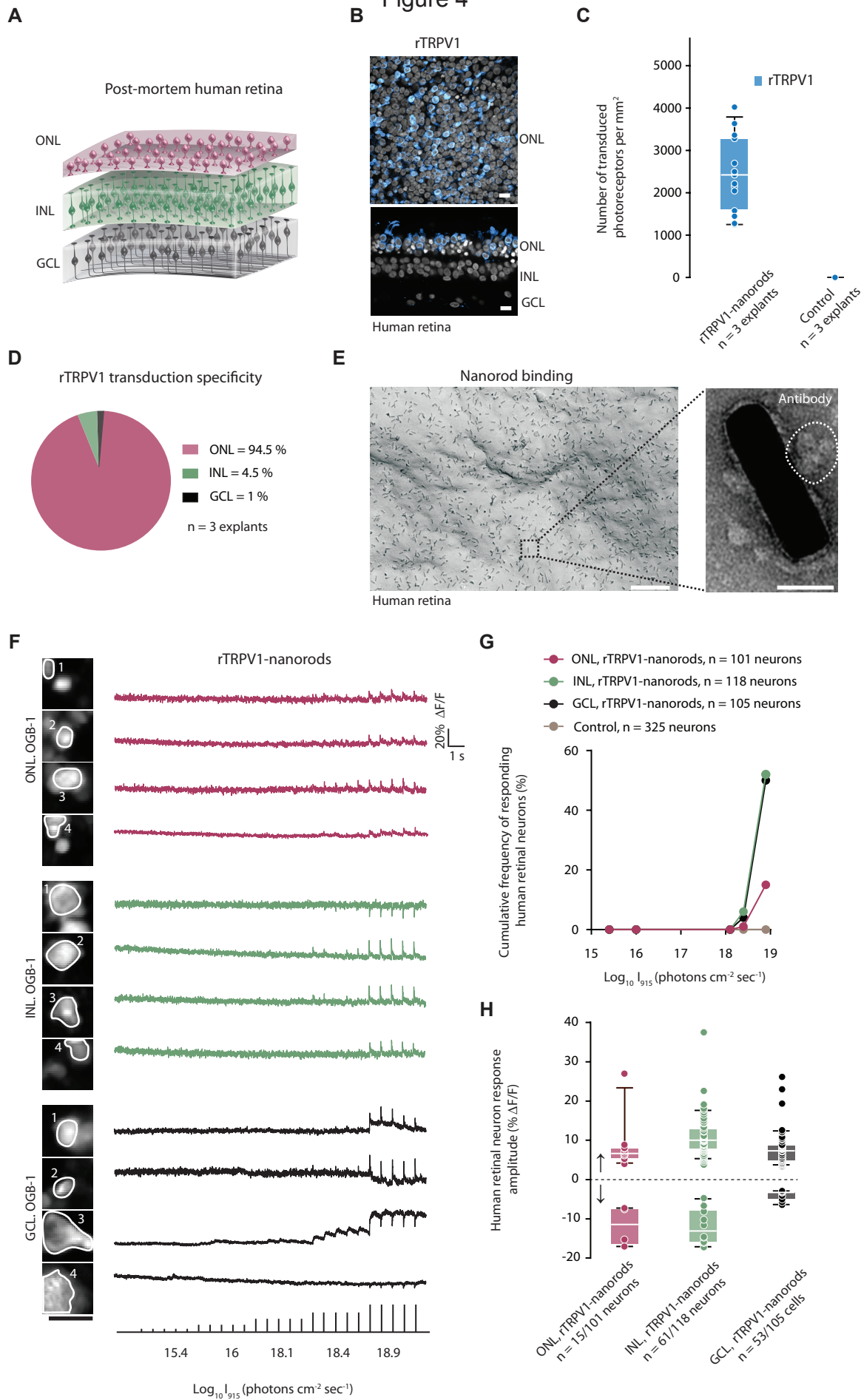


Figure 4





Supplementary Materials for

Restoring light sensitivity using tunable near-infrared sensors

Authors: Dasha Nelidova, Rei K. Morikawa, Cameron S. Cowan, Zoltan Raics, David Goldblum, Hendrik Scholl, Tamas Szikra, Arnold Szabo, Daniel Hillier, Botond Roska.

Correspondence to: daniel.hillier@iob.ch, botond.roska@iob.ch

This PDF file includes:

Materials and Methods
Supplementary Text
Figs. S1 to S13
Tables S1 to S4

Materials and Methods

Animals

Wild-type (strain: C57BL/6J, stock number: 632) and rd1 mice (strain: C3H/HeNCrL, stock number: 025) were obtained from Charles River. Scnn1a-Cre mice (strain: B6;C3-Tg(Scnn1a-cre)3Aibs/J, stock number: 009613) and Ai94(TITL-GCaMP6s)-D mice (strain: B6.Cg-Igs7.tm94.1(tetO-GCaMP6s)Hze.IJ, stock: 024104) were purchased from Jackson Laboratory. Ai94(TITL-GCaMP6s)-D mice were initially crossed to Scnn1a-Cre mice to obtain mice hemizygous for each gene. Hemizygous offspring were subsequently crossed to rd1 mice. Mice used for cortical calcium imaging experiments were hemizygous for Cre and GCaMP6s and homozygous for the rd1 mutation. Access to water was restricted for behavioral training but was otherwise freely available. Animal experiments were performed according to standard ethical guidelines and were approved by the Veterinary Department of Canton Basel Stadt.

Human retinal tissue

Human retinal tissue was obtained after corneal tissue procurement from adult multi-organ donors with no reported history of eye disease. All tissue samples were obtained in accordance with the tenets of the Declaration of Helsinki. Personal identifiers were removed and samples were coded before processing. All procedures and experimental protocols were approved by the local ethics committee. The study includes $n = 2$ eyes from $n = 2$ donors. After cornea isolation, the iris, lens, and vitreous were removed and the retina was submerged in flowing Ames' medium (Sigma, A1420) saturated with 95% O₂ and 5% CO₂. Time elapsed from central retinal artery clamp to artificial *ex vivo* perfusion did not exceed 5 min. Samples used for tissue culture were of mid-peripheral origin, midway between the fovea and the anterior retinal border. For organotypic retinal culture, 4×4 mm retinal pieces were isolated and placed photoreceptor-side-up on polycarbonate membranes inserts (Corning, 3412). The cultures were maintained at 37°C and 5% CO₂ in DMEM/F12 medium (Thermo Fisher Scientific), supplemented with 0.1% bovine serum albumin (BSA), 10 μM *O*-acetyl-L-carnitine hydrochloride, 1 mM fumaric acid, 0.5 mM galactose, 1 mM glucose, 0.5 mM glycine, 10 mM HEPES, 0.05 mM mannose, 13 mM sodium bicarbonate, 3 mM taurine, 0.1 mM putrescine dihydrochloride, 0.35 μM retinol, 0.3 μM retinyl acetate, 0.2 μM (+)- α -tocopherol, 0.5 mM ascorbic acid, 0.05 μM sodium selenite, 0.02 μM hydrocortisone, 0.02 μM progesterone, 1 μM insulin, 0.003 μM 3,3',5-triiodo-L-thyronine, 2 000 U penicillin and 2 mg streptomycin (Sigma). For AAV infection 40 μL of virus was applied per retinal explant 4–5 days after plating. The culture medium was renewed every 48 hours. Light responses were recorded from samples 8 weeks post-mortem.

Nanorods

Gold nanorods tuned to 915 nm or 980 nm were purchased from Nanopartz Inc (Loveland, USA) and were functionalized by conjugation to anti-Histidine (Millipore, mouse monoclonal anti-polyHis, 05949) or anti-Ollas (Novus Biologicals, rat monoclonal anti-Ollas epitope tag L2, NBP1-06713) antibodies. 10¹⁰ nanorods were administered per eye. Additional nanorod related information can be found in Table S2.

TRP channel design

Rat TRPV1 (NM 031982.1) and snake *Elaphe (Pantherophis) obsoleta lindheimeri* TRPA1 (GU 562966) open reading frame sequences were chemically synthesized by Genewiz Inc (South Plainfield, USA). The snake sequence was codon optimized for *Mus musculus* (Java Codon Adaptation Tool, www.jcat.de). Rat TRPV1 protein was tagged by 6x-His introduced in the first extracellular loop, after amino acid 459 or 465. Extracellular loop location was determined based on the cryo-EM structure of rat TRPV1 (PDB 3J5P) (18). Snake TRPA1 protein was tagged by Ollas (SGFANELGPRLMGK) (12) flanked by GSG linkers, introduced after amino acid 755 or 758 (first loop) or 824 (second loop). To identify loop domains, first, the location of extracellular loop domains of human TRPA1 (PDB 3J9P) were determined from its cryo-EM structure (13). Subsequently, predicted loop domains of snake TRPA1 were identified after pairwise sequence alignment, generated using HHPRED (14), between C-terminal domains of human (Uniprot O75762) and snake TRPA1 (Uniprot D4P382).

Plasmids

For *in vitro* HEK293T cell experiments, sequences encoding TRP variants were fused to T2A self-cleaving peptide (LEGRGSLTTCGDVEENPGPAPGST) and either mCherry or GFP fluorescent protein. Variants were inserted into linearized pAAV-EF1a-CatCh-GFP plasmid via restriction sites and homologous recombination, replacing the CatCh-GFP sequence. pAAV-EF1a-CatCh-GFP plasmid was constructed by adaptor PCR and the Clontech In-Fusion kit using pcDNA3.1(-)-CatCh-GFP (a kind gift of E. Bamberg, MPI, Frankfurt) and pAAV-EF1a-GFP (B. Roska lab plasmid collection). To generate pAAV-mCAR-TRPV1.465-6x-His (rTRPV1), plasmid pAAV-mCar-MAC-mCherry (B. Roska lab plasmid collection) was linearized with NotI/HindIII. Subsequently, PCR amplified TRPV1.465-6x-His (from pAAV-EF1a-TRPV1.465-6x-His-T2A-mCherry) was inserted, replacing the MAC-mCherry sequence. To generate pAAV-mCAR-TRPA1.755-Ollas (sTRPA1), plasmid pAAV-mCar-MAC-mCherry was linearized with NotI/MluI. Subsequently, PCR amplified TRPA1.755-Ollas (from pAAV-EF1a-TRPA1.755-Ollas-T2A-mCherry) was inserted, replacing the MAC-mCherry sequence. To generate pAAV-CAG-TRPV1.465-6x-His, plasmid pAAV-CAG-ChrimsonR-tdtomato (a kind gift of D. Dalkara, Vision Institute, Paris) was linearized with ClaI/HindIII. Subsequently, PCR amplified TRPV1.465-6x-His (from pAAV-EF1a-TRPV1.465-6x-His-T2A-mCherry) was inserted, replacing the ChrimsonR-tdtomato sequence. The names of TRP plasmids generated are listed in Table S3. To induce GCaMP6s expression in cortical experiments, AAV-pCAG-FLEX2-tTA2 plasmid was obtained from Addgene (65458).

AAV production

AAV production was carried out as described previously (11). Briefly, HEK293T cells were co-transfected with an AAV transgene plasmid, an AAV helper plasmid encoding the AAV Rep2 and Cap proteins for the selected serotype, and the pHGT1-Adeno1 helper plasmid harboring adenoviral genes (kindly provided by C. Cepko, Harvard Medical School, Boston) using branched polyethyleneimine (PEI, Polysciences). The AAVs were isolated using a discontinuous iodixanol gradient (OptiPrep, Sigma, D1556) and ultracentrifugation. AAV particles were purified and concentrated in Millipore Amicon 100K columns. Genome copy number titration was performed

using real-time PCR (Applied Biosystems, TaqMan reagents). AAVs were used when titer was equal to or greater than 10^{13} genome copies per mL. We used serotype BP2 to deliver TRP channels to photoreceptors (19). To induce GCaMP6s expression in cortical experiments, serotype PHP.eB (20) was used to deliver AAV-pCAG-FLEX2-tTA2.

Injections

Ocular injections to deliver AAVs with TRP transgenes were performed on ~4 week old mice anesthetized with 2.5% isoflurane. When required, nanorods were co-injected. A small incision was made with a sharp 30 gauge needle at the nasal corneoscleral junction and AAV, with or without nanorods, was injected through this incision into the subretinal space using a blunt 5 μ L Hamilton syringe held in a micromanipulator. For cone photoreceptor activity monitoring, cone specific AAV-GCaMP6s was co-injected subretinally with rTRPV1 AAV. A maximum volume of 2.5 μ L was administered per eye. For primary visual cortex activity monitoring, AAV-pCAG-FLEX2-tTA2 was delivered by intravenous retro-orbital injection as previously described (21) 2 weeks after initial ocular injection of rTRPV1 and nanorods. There was a minimum incubation time of 3 weeks after intraocular injection before performing experiments on AAV injected animals.

Surgery for *in vivo* two-photon imaging and behavior

Craniotomy surgery for *in vivo* two-photon imaging was performed as described previously (21). Briefly, mice were anesthetized with a mixture of fentanyl (Mepha) (0.05 mg/kg), medetomidine (Virbac) (0.5 mg/kg) and midazolam (Roche) (5.0 mg/kg) and were head-fixed in a stereotaxic frame (Narishige, SR-5M-HT). A circular craniotomy of ~3.5 mm diameter was made above the primary visual cortex. After removal of the skull flap, the cortical surface was kept moist with a cortex buffer containing 125 mM NaCl, 5 mM KCl, 10 mM glucose, 10 mM HEPES, 2 mM MgSO₄ and 2 mM CaCl₂. The cortex was then covered with a 3 mm diameter glass coverslip and sealed with dental acrylic cement (Paladur, Kulzer). A metal bar for head fixation during imaging was glued to the skull (Vetbond, 3M) followed by further dental cement treatment. For behavioral experiments, a custom-made titanium headbar was attached to the skull with tissue adhesive and dental cement.

HEK293T cell current recordings

For HEK293T cell experiments, cells were maintained at 37°C on poly-D-lysine/laminin coated coverslips (GG-12-Laminin, Neuvitro) in DMEM supplemented with 10% fetal bovine serum. Cells were transfected with plasmids containing TRP variants using branched PEI. Cells were perfused in oxygenated Ringer's medium containing 110 mM NaCl, 2.5 mM KCl, 1 mM CaCl₂, 1.6 mM MgCl₂, 10 mM D-glucose and 22 mM NaHCO₃ at ~36°C for the duration of the experiment. Recordings were made in whole-cell voltage clamp mode with borosilicate pipettes (Sutter Instrument Company) pulled to between 4–6 M Ω resistance, voltage clamping the cells to –60 mV. The intracellular solution contained 115 mM potassium gluconate, 9.7 mM KCl, 1 mM MgCl₂, 0.5 mM CaCl₂, 1.5 mM EGTA, 10 mM HEPES, 4 mM ATP-Na₂, 0.5 GTP-Na₂ at pH 7.2. For comparison of currents between tagged and untagged channels, TRPV1 agonist capsaicin (Sigma, 360376) and TRPA1 agonist allyl isothiocyanate (AITC, Sigma, W203408) were bath

applied at 2.5 μM and 700 μM , respectively, using a valve system (VC-6, Warner Instruments). Electrophysiological recordings were made using an Axon Multiclamp 700B amplifier (Molecular Devices). Signals were digitized at 10 kHz (National Instruments). Data was analyzed offline using MATLAB (MathWorks).

Near-infrared stimulation

Near-infrared (NIR) pulses were produced by two custom-made, single wavelength NIR diode lasers emitting at 915 nm or 980 nm, modelled after (22). The laser diode was driven by a pulsed quasi-CW current power supply (Lumina Power, Bradford, USA). The controller had a rise time of 25 μs . Laser emission from the diode was collimated using an aspherical lens ($f \frac{1}{4}$ 11.5 mm, 0.25 NA). For *ex vivo* retinal experiments, laser output was launched into a fiber optic patch cable (Thorlabs, M79L01) interconnected with a fiber optic cannula (Thorlabs, CFM14L20) (both 400 μm , 0.39 NA). The cannula was positioned 300 μm above and 300 μm lateral to the imaging plane, at angle of 30–35°. Full-field, 100 ms pulses were delivered every 2–10 s. For *in vivo* cortical and behavioral experiments lasers were connected to a fiber optic patch cable positioned 6 mm from the cornea (550 μm , 0.22 NA) (Thorlabs, M37L02). A visible laser line (532 nm), coupled to both NIR lasers, aided alignment over the center of the pupil. Full-field, 100 ms or 200 ms pulses were delivered every 1–30 s. Total laser power output, as a function of driving voltage, was measured by placing cannula (CFM14L20) and patch cable (M37L02) output at the entrance of an integrating sphere photodiode power sensor (Thorlabs, S142C) with a PM100D read-out unit. Oscilloscope read-out of laser response time was obtained by applying a step control voltage to the lasers. Light intensities are indicated in the text and in Table S4.

Two-photon calcium imaging of mouse cone photoreceptors

Wild-type and *rd1* retinas were isolated in oxygenated Ringer's medium. For cone photoreceptor calcium-based activity monitoring mouse retinas were mounted ganglion cell-layer-up on filter paper (MF-membrane, Millipore, HAWP01300) with a 2 \times 2 mm aperture to allow for light stimulation of the photoreceptors. To expose photoreceptors, the pigment epithelium layer was peeled away. In *rd1* experiments, nanorods were reapplied to the photoreceptor side after peeling (10^{10} nanorods). During imaging, the retina was continuously perfused with oxygenated Ringer's medium at $\sim 36^\circ\text{C}$. The calcium sensor GCaMP6s was targeted to cone photoreceptors virally, using cell-type specific promoter ProA1 or ProA7 (11) to restrict expression to cones. GCaMP6s-expressing cone cell bodies and axon terminals were imaged in a wholemount preparation of the retina. NIR light recordings in wild-type cones were made in light adapted retinas. The two-photon microscope system used was equipped with a two-photon laser scanning at 920 nm (Spectra Physics, Santa Clara, USA) and a 60 \times objective (Fluor, 1.0 NA, Nikon). Images were acquired using software developed by SELS Software (Hungary), taking images of 150 \times 150 pixels at 10 Hz. Fluorescence was analyzed semi-online using software written in Python (23). Cone axon terminals and cell bodies were segmented manually. Fluorescence values were then normalized as $\Delta F/F$, where F represents baseline fluorescence (mean fluorescence of a 1–2 s time window before the onset of the stimulus). Full-field, 915 nm, 100 ms stimulus was presented 2–3 times at each intensity. Full-field, 405 nm, 2 s stimulation was used for wild-type cones. Responses to different trials were averaged before calculating peak responses. Responses were analyzed offline using MATLAB. NIR induced *rd1* responses were the means of 3 $\Delta F/F$ values within 2 s of stimulation

onset, including the maximum value and its immediately adjacent 2 data points. Visible light responses were calculated as the mean of $\Delta F/F$ values during the second half of the stimulation period. Cells were considered responsive when Z scores exceeded 1.5 for each of the stimulus repetitions.

Two-photon calcium imaging of mouse retinal ganglion cells

Rd1 retinas were isolated in oxygenated Ringer's medium. Oregon Green 488 Bapta-1 (OGB-1) calcium dye (Invitrogen, O-6806) was bulk electroporated into retinal ganglion cells as described before (16, 17). Briefly, the retina was flat mounted on anodisc filter membranes (#13, 0.2 μm pore size, GE Healthcare, Maidstone, UK) ganglion cell-layer-up. Nanorods were added to the photoreceptor side (10^{10} nanorods). Retinas were electroporated between 3 mm horizontal plate electrodes (Sonidel, CUY700P3E) with 10 μL of 5 mM OGB-1 in Ames' medium using 10–12 pulses (9 V, 100 ms, 1 Hz) from TGP110 Pulse Generator (Aim & TTI, Cambridge, England). The tissue was left to recover for 60 min before recording activity. Calcium-based activity was recorded using the same two-photon microscope system as for cone photoreceptor recordings. Full-field, 915 nm, 100 ms stimulus was presented 5 times at each intensity. Fluorescence was analyzed offline using software written in Python. Raw traces were corrected for slow drifts in baseline fluorescence. NIR responses were evaluated using a 3-sample average of the peri-stimulus activity. Peak responses within a 1 s post-stimulus interval were extracted for every trial and averaged. Cells were considered responsive if at least one third of the pairwise Pearson correlation coefficients across repeated trials exceeded 0.25 with $P < 0.05$.

Two-photon calcium imaging in mouse primary visual cortex

For primary visual cortex calcium-based activity monitoring, Cre- and Tet- dependent Ai94-GCaMP6s mice were crossed to Scnn1a-Cre mice and to rd1 mice (see "Animals"). Tetracycline-controlled transactivator (tTA2), delivered by intravenous retro-orbital injection (see "Injections"), induced layer 4 specific GCaMP6s expression 7–10 days later. GCaMP6s expressing neurons were imaged using a two-photon laser scanning at 920 nm (Femto2D RC, Femtonics, Budapest, Hungary), equipped with a 16 \times Nikon water-immersion objective (0.8 NA). During imaging, mice were anesthetized with chlorprothixene (Sigma, C1671) (2.5 mg/kg) and maintained with 0.25% isoflurane. A Python-based user interface controlled visual stimulation, data recording and alignment. Layer 4 imaging was performed in steps of 20 μm , at depths of 300–440 μm below the pial surface. 250 \times 350 pixel images were acquired at 6–10 Hz. Eyes were dilated with atropine 0.5% (Thea, 2094264) 15 min before imaging. Full-field, 100 ms NIR light was presented 5 times at each intensity to the contralateral eye. Detection of active cells was performed online as previously described (21) and subsequently refined and deconvolved offline (24). Trials with deconvolved calcium transients between 200–1500 ms after stimulus onset were considered responsive. Cells were considered responsive when at least 60% of trials were responsive for any light intensity. Normalized $\Delta F/F$ from raw fluorescence was calculated using the mean of fluorescent samples 150 ms before stimulus onset as the baseline. NIR responses were evaluated using a 3-sample average of the peri-stimulus activity. Peak responses within a 600 ms post-stimulus interval were extracted for every trial and averaged. To evaluate cortical wavelength preference, NIR stimulation was performed with wavelengths matched to and offset from nanorod absorption maxima. The same layer 4 population was imaged twice, once with 980 nm

stimulation of the eye and once with 915 nm stimulation. To establish response correspondence during wavelength preference experiments, imaging planes were manually aligned to image the same neurons across two conditions (matched and unmatched stimulation wavelengths). Wavelength preference index (WPI) was defined as:

$$\text{WPI} = (\Delta F/F_{980} - \Delta F/F_{915}) / (\Delta F/F_{980} + \Delta F/F_{915}).$$

Light intensity preference index was defined as:

$$\text{LPI} = (\Delta F/F_{\text{lower intensity}} - \Delta F/F_{\text{higher intensity}}) / (\Delta F/F_{\text{lower intensity}} + \Delta F/F_{\text{higher intensity}}).$$

Mouse behavior

Rd1 mice underwent surgery to attach a titanium headbar to the skull and were left to recover for 2–3 days before being placed on a water restriction schedule. Thereafter, mice were handled daily and received ~ 0.5–1 mL of water per session, until body weight reached ~ 80% of the *ad libitum* weight (typically within 5–7 days). Health status and weight were monitored daily. Before starting behavioral evaluation, mice were progressively habituated to the experimental setup, including head fixation and enclosure within a ‘body’ tube (25). Enclosure of the mouse body within a cylindrical acrylic tube was found to maximize animal comfort during head fixation. Eyes were dilated with atropine 0.5% 15 min before behavioral evaluation. Rd1 experiments were performed in the dark. NIR experiments in wild-type mice were performed in ambient light. Visible light experiments in wild-type mice were performed in the dark. Mice performed a voluntary action NIR detection task by licking a waterspout (blunt 18G needle, 5 mm from mouth) in response to full-field, 200 ms stimulation of one eye (915 nm, 980 nm, white light). Water (~7 μL) was automatically dispensed 500 ms after light onset, through a calibrated gravity water system gated with a solenoid pinch valve. NIR intensities were randomly interleaved. Inter-trial intervals ranged between 10–30 s. Training lasted 4 days for NIR light and/or 4 days for visible light. Typical sessions lasted ~ 40 min during which mice performed 80–100 trials. To assess the impact of the light cue, lick rates were calculated after stimulus onset but before water valve opening. Spontaneous background lick rates (1 s time window before stimulus onset) were subtracted from stimulus-driven lick rates. For Z scores, mean and standard deviation of a 500 ms background time interval were used. An Arduino Uno board provided control of the behavioral protocol, including lick detection, water valve opening, and variation of NIR stimulus intensities. Lick events were detected by a transistor-based circuit and recorded by a USB 6002 (National Instruments, Austin) data acquisition device. Custom control software was written in Python (SELS Software).

Two-photon calcium imaging in *ex vivo* human retina

OGB-1 calcium dye was bulk electroporated into human retinal explants as described above (see “Two-photon calcium imaging of mouse retinal ganglion cells”). Electroporation was observed to introduce OGB-1 into all 3 nuclear layers of the retina. Low melting temperature 1% agarose gel (Sigma, A2790) was added to the ganglion cell side to stabilize the retina and was kept in place throughout the experiment. Nanorods were added to the photoreceptor side (10^{10} nanorods). During activity monitoring, the human retina was continuously perfused with

Ames' solution bubbled with 95% O₂ and 5% CO₂ at ~37°C. For acousto-optic imaging, a z-stack was taken before NIR stimulation with the acousto-optic deflector two-photon (AOD) microscope (Femtonics, Budapest, Hungary) using a 16× water immersion objective (0.8 NA) to capture the 3D volume of the retina. Within this volume, the experimenter manually selected cell soma positions of OGB-1 filled cells. Full-field, 915 nm, 100 ms light stimulus was presented 5 times at each intensity. During stimulation the AOD scanned a set of square XY planes encompassing each cell body at ~50 Hz. Fluorescence values were analyzed offline by custom software in MATLAB. Neurons were segmented by selecting a cell center manually and applying Chan-Vese segmentation. NIR responses were evaluated using a 3-sample moving average of the peristimulus activity. Peak responses within an 800 ms post-stimulus interval were extracted for every trial and averaged. Cells were considered responsive when peak absolute fluorescence was > 4.5 standard deviations above the pre-stimulus fluorescence in at least 80% of trials.

Immunofluorescence and confocal imaging

HEK293T cells and retinas were fixed overnight in 4% paraformaldehyde and washed overnight with phosphate buffered saline (PBS) at 4°C. To improve antibody penetration, wholemount retinas were subjected to freeze-thaw cycles after cryoprotection with 30% sucrose. After washing in PBS, retinal wholemounts, 3% agarose-embedded (SeaKem, Lonza, 50004) 150 μm thick retinal vibratome sections (Leica VT1000 S) or HEK293T cells on coverslips were incubated for 2–4 h in blocking buffer containing 10% normal donkey serum (NDS, Chemicon), 1% BSA, 0.5% TritonX-100, and 0.01% sodium azide (Sigma) in PBS. Primary antibody treatment was performed for 5–7 days at room temperature in buffer containing 3% NDS, 1% BSA, 0.01% sodium azide, and 0.5% TritonX-100 in PBS. Primary antibodies used in this study were: rat monoclonal anti-GFP (Nacalai, 04404-84), rabbit polyclonal anti-GFP (Thermo Fisher Scientific, A11122), rabbit polyclonal anti-Cone Arrestin (Millipore, AB15282), rat monoclonal anti-RFP (Chromotek, 5F8-100), rabbit anti-RFP (Rockland, 600-401-379), goat polyclonal anti-Opn1mw/mw2/lw (Santa Cruz, sc22117), goat polyclonal anti-Opn1sw (Santa Cruz, sc14365), rabbit polyclonal anti-Capsaicin receptor (Millipore, AB5370), rat monoclonal anti-OLLAS (Novus Biologicals, NBP1-06713), mouse monoclonal anti-polyHis (Millipore, 05949), rabbit polyclonal anti-Iba1 (Genetex, GTX100042). Hoechst was used to stain cell nuclei. Apoptotic cells were detected using the *In Situ* Cell Death Detection Kit, Fluorescein (Roche, 11684795910). DNase I recombinant (Promega, M6101) digestion was used to induce DNA strand breaks in the positive control. For microscopy retinas were mounted on glass slides with ProLong Gold antifade reagent (Invitrogen, P36982). A Zeiss LSM 700 laser scanning confocal microscope was used to acquire images of antibody stained cells and tissues with an EC Plan-Neofluar 40×/1.30 oil M27 objective at up to 4 excitation laser lines according to secondary antibody specification. Expression was assessed from 1024×1024 pixel images in a z-stack with 0.75 μm steps. Images were processed using Imaris (Bitplane) and Image J (Fiji). AAV transduction was quantified from retinal wholemounts. In each sample the entire thickness of the retina was scanned by confocal microscopy at 3 or 5 randomly chosen areas in AAV transduced regions.

Transmission electron microscopy

To measure nanorod sizes 4 μL of nanorod stock solution was adsorbed for 2 min to glow-discharged formvar carbon-coated copper grids (Ted Pella Inc, Redding, USA, 01753-F). The

grids were then blotted and negatively stained on 2 droplets of 2% uranyl acetate solution (Electron Microscopy Sciences, 22400) for 20 s. Samples were imaged at a nominal magnification of 30000× using a Tecnai Spirit electron microscope (FEI, Eindhoven, Netherlands) operating at 120 kV. Electron micrographs were recorded using a bottom mount 4K×4K CCD FEI Eagle camera.

Scanning electron microscopy

Retinal samples were placed on glass slides. Nanorod stock solution was applied for 40 min at room temperature, followed by extensive rinses with deionized H₂O. The retina was dehydrated progressively for 30–50–70–90–95–100 (2×) and immersed in hexamethyldisilazane (Sigma, 440191) for 10 min (2×). Subsequently, the samples were dried for 90 min at 60°C. Samples were metalized with gold palladium (Quorum, SC7620) for 15 s and imaged in a scanning electron microscope (FEI Versa 3D) at 5 kV and 3 nm per pixel with an ETD detector. Lookup tables were inverted in post-processing.

Statistical Analysis

We used the following statistical tests: Mann-Whitney U test (two-tailed) and Wilcoxon Matched-Pairs Signed Rank Test. P values are stated in the text and in Table S1. n.s refers to $P \geq 0.05$. In all figures; boxplots: center line, median; box edges, first and third quartiles; whiskers, 10th and 90th percentile.

Safety

NIR exposures are governed by ocular laser safety standards (ANSI Z136.1-2000). We calculated maximum permissible exposures according to ANSI-Z136.1 (26). Maximum permissible radiant power ($MP\Phi$) which may be chronically delivered to the retina is:

$$MP\Phi = 6.93 \times 10^{-5} C_T C_E P^{-1}$$

where $C_T = 10^{0.002(\lambda[nm]-700)}$ in the 700 - 1050 nm range, with $C_T = 2.7$ at $\lambda = 915$ nm and $C_T = 3.6$ at $\lambda = 980$ nm. C_E depends on the angular spread of the incident beam and for retinal spot sizes greater than 1.7 mm in diameter, $\alpha = \alpha_{\max} = 100$ mrad and $C_E = 6.67 \times 10^{-3} \alpha^2 = 66.7$ W (26). P is the pupil size factor, $P = 1$ for NIR wavelengths. Maximum permissible exposure for 915 nm light is 0.0125 Watts (12.5 mW). Maximum permissible exposure for 980 nm light is 0.0166 Watts (16.6 mW). In Maxwellian ophthalmic illumination the maximum permissible retinal radiant exposure MPH_r is given by the power entering the pupil Φ divided by the retinal exposure area. For $\alpha = \alpha_{\max} = 100$ mrad the dimension of the exposed retina is assumed to be 1.7 mm in diameter. Thus for chronic exposure $MPH_r = 5.5$ mW mm⁻² (5500 W m⁻²) for 915 nm and $MPH_r = 7.3$ mW mm⁻² (7300 W m⁻²) for 980 nm. rTRPV1 activation *in vivo* requires 4060 W m⁻² of NIR 915 nm light (Table S4). sTRPA1 activation *in vivo* requires 1840 W m⁻² of NIR 915 nm light (Table S4). Both intensities are below ocular safety limits for NIR 915 nm light.

To assess thermal aspects, we calculated temperatures at the nanorod. We assumed a monolayer of gold nanorods equally spaced. We calculated nanorod absorption cross-sections from measured optical densities and number of nanorods in the eye. Mouse eye optical properties were assumed

to be similar to water, absorption coefficient = $6.6 \times 10^{-6} \mu\text{m}^{-1}$ at 915 nm, except for pigmented tissues. Absorption coefficient for pigmented tissue was taken as 0.2 mm^{-1} . We then solved the 1D heat differential equation:

$$Q = (\kappa T^{(0,1)} [x, t] / \alpha) - \kappa T^{(2,0)} [x, t]$$

where Q is heat flux, κ is thermal conductivity, α is thermal diffusivity, x is distance, t is time and T is temperature. Mouse eye thermal properties were assumed to be similar to water, with thermal diffusivity = $150.87 \mu\text{m}^2/\text{ms}$, thermal conductivity = $6.26 \times 10^{-4} \text{ kg } \mu\text{m}/(\text{ms}^3\text{K})$, mass density = $9.93 \times 10^{-16} \text{ kg}/\mu\text{m}^3$. For TRPV1, nanorod temperatures reach a maximum of 43.0°C . For TRPA1, nanorod temperatures reach a maximum of 39.7°C . Published reports of TRPV1 and TRPA1 thermosensitivity report activation temperatures of $\sim 43^\circ\text{C}$ for TRPV1 and $\sim 39^\circ\text{C}$ for TRPA1 (3, 27).

Supplementary Text

Near-infrared light stimulation

For human patients with retinal degeneration visual patterns can be projected onto the retina by biomimetic eye goggles (<https://www.gensight-biologics.com>, Medical Device GS030; Clinical Trials ID: NCT03326336). The device consists of an external camera, a signal processing unit and a high-brightness, near-to-eye display that is NIR light compatible. Light patterns are projected by micromirror arrays. In this way, natural scenes are converted to modified NIR images. A device with similar properties but small enough to fit a mouse eye is currently not available. In addition, NIR LEDs positioned in the environment are not bright enough to activate TRP channels. It is therefore not possible to present structured stimuli or perform behavioral tests with freely moving animals.

Compatibility with remaining vision

To prevent superimposition of visible and NIR responses in light sensitive retinal regions, two solutions may be considered. First, in conventional human subretinal surgery, the procedure is a vitrectomy followed by formation of a subretinal bleb. Since bleb formation involves separation of tightly apposed photoreceptor and retinal pigment epithelial layers, blebs have defined perimeters, which spatially restrict virus and nanorod deposition to specific, pre-determined sites. Central retina (macula) may be transduced while peripheral retinal regions remain unmodified. Second, NIR vision requires NIR images to be projected by stimulator eye goggles into the patient eye. Images can be focused onto the macula via an eye tracker based projection system. In nearby regions NIR intensities would be reduced by the inverse square law. Since lower NIR intensities do not generate enough heat to activate TRP channels, unfocussed NIR light is unlikely to lead to activation.

Nanorod stability *in vivo*

Cytotoxicity studies report low or no toxicity of nanorods up to 70 days post intravitreal or subretinal injection (28-33). Longer-term effects in the eye are not yet known. Stable, covalent polymer bridges bind antibodies to nanorods. Antibody-epitope binding relies on weaker, non-covalent bonds. Gold nanoparticle stability (plasmon band, hydrodynamic diameter, core diameter) ranges from highly-stable to ultra-stable (34-38). Ultra-stable gold nanoparticles maintain stability in various environments including solubilization in ionic media, freeze-drying, heating (65°C), ultracentrifugation and autoclave sterilization (39-40). Preclinical studies will be required to determine stability precisely.

Nanorod tuning

We tuned responses to different wavelengths for several reasons. First, enabling light sensitivity in a blind human retina requires specialized projector eye goggles (Medical Device GS030; Clinical Trials ID: NCT03326336) that utilize specific wavelengths. Compatibility with current and future NIR projector goggles requires tunable NIR detectors. Second, over time it may be found that some NIR wavelengths are better tolerated by patients than others. It is then

advantageous to know that nanorod manufacturing technologies can be exploited to tune responses to different wavelengths, if required. Third, if it is possible to segregate nanorods by type around cone photoreceptors, in the future this could be used for inducing color vision. Fourth, since maximum permissible radiant exposures vary with incident wavelength, tuning responses to different NIR wavelengths plays an important role in compliance with safety standards.

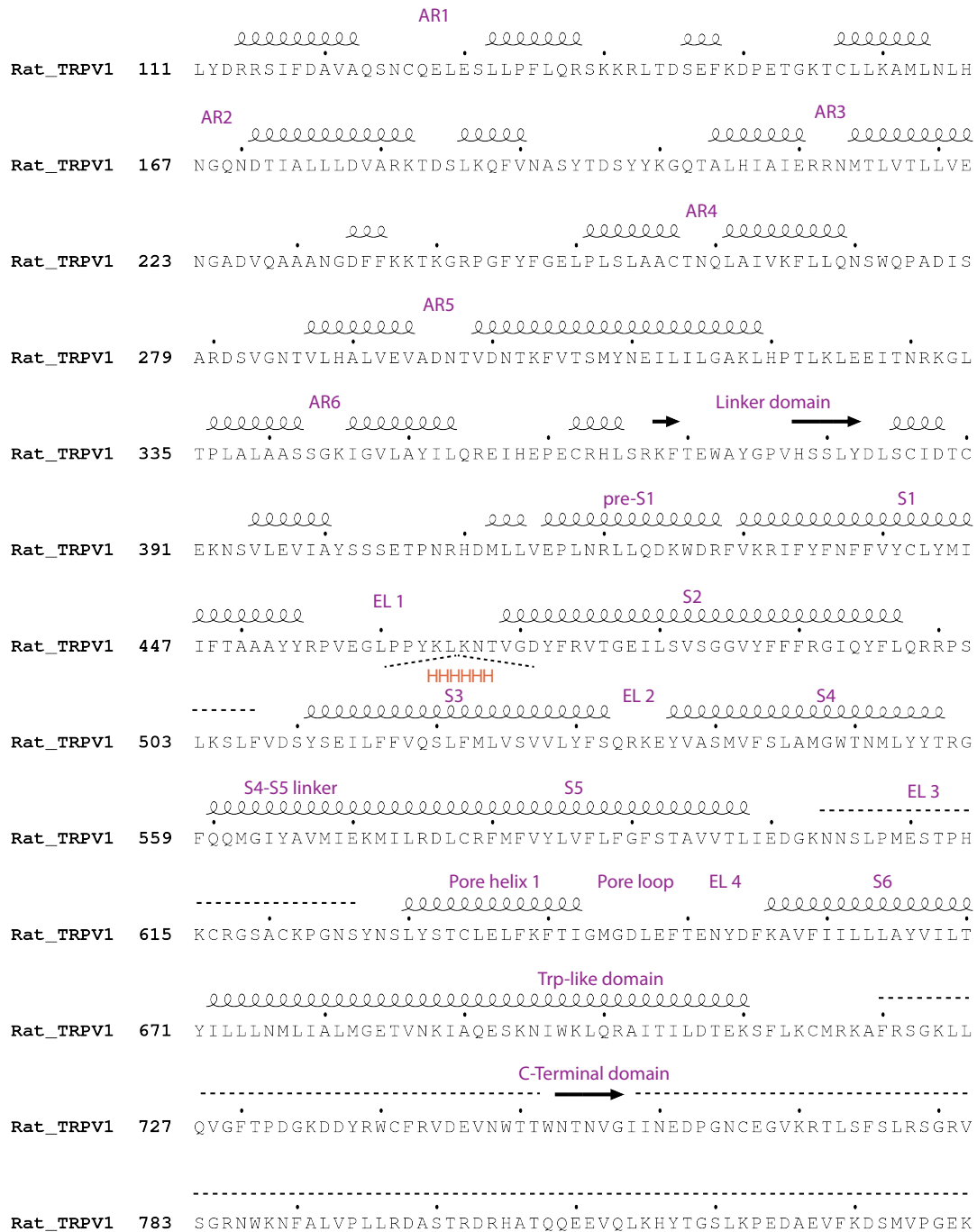


Fig. S1. Peptide sequence of rat TRPV1, starting at amino acid 111. 6x-His (HHHHHH) epitope tag insertion at amino acid 465 (EL1) is highlighted with tilted dashed lines. Secondary structure elements are indicated above the sequence as spirals (helices) and arrows (β strands). Regions with no assigned secondary structure are indicated by horizontal dashed lines. Black dots mark the position of every tenth amino acid. EL refers to extracellular loop, AR to ankyrin repeat, S to transmembrane domain.

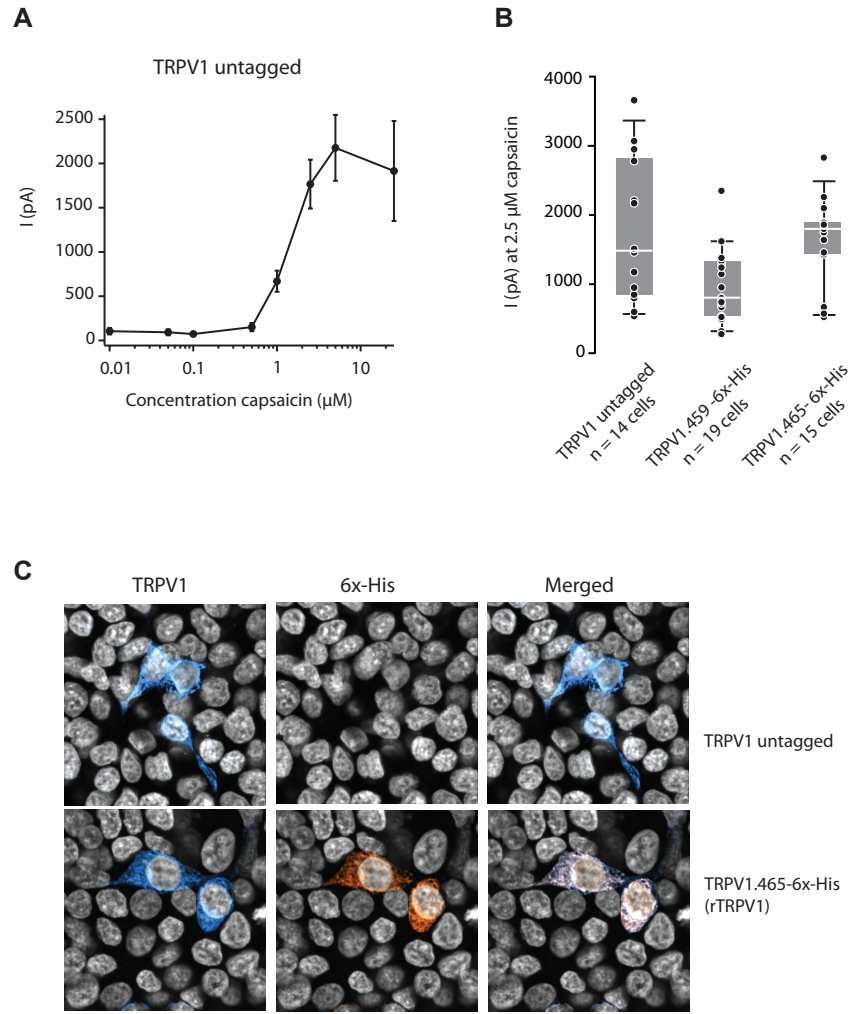


Fig. S2. Capsaicin-evoked whole-cell currents in HEK293T cells expressing rat TRPV1 channel variants. **(A)** Capsaicin dose-response curve for untagged rat TRPV1. Error bars, s.e.m. **(B)** Comparison of untagged TRPV1 with tagged variants at 2.5 μM capsaicin. **(C)** Top row, top views of HEK293T cells transduced with untagged TRPV1, immunostained for TRPV1 (left, blue), 6x-His (middle, orange), and merging the two (right). Grey, Hoechst nuclear stain. Bottom row, same views for HEK293T cells transduced with TRPV1.465-6x-His (rTRPV1). Scale bar 10 μm .

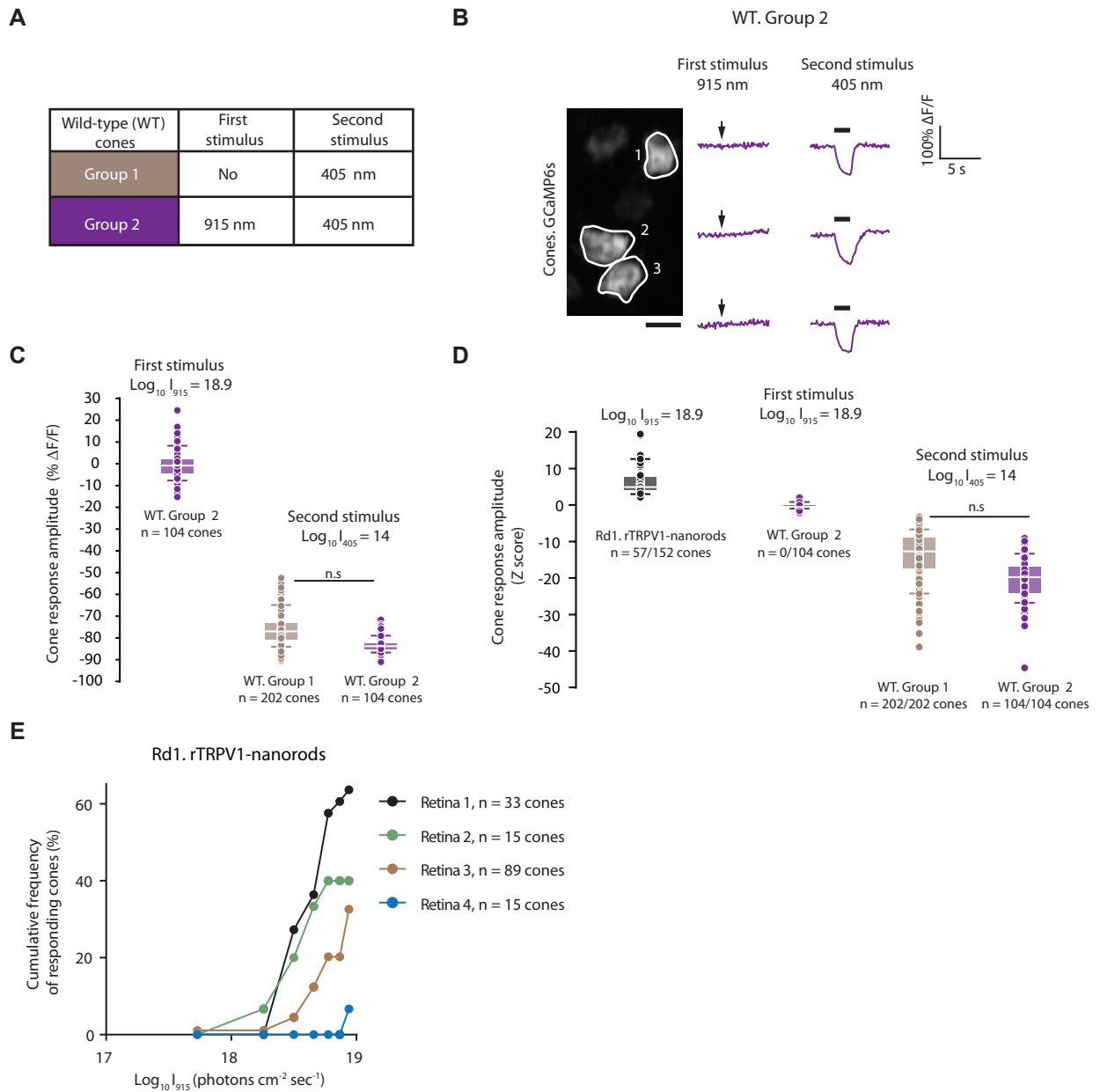


Fig. S3. Near-infrared and visible light responses in mouse cone photoreceptors. **(A)** Wild-type (WT) cone experiments. Group 1 (brown, $n = 3$ mice), visible light only. Group 2 (purple, $n = 3$ mice), first NIR then visible light. **(B)** Example calcium responses (mean $\Delta F/F$, 3 repetitions) recorded from cone axon terminals in WT retinas. Stimulus, full-field. Left, 915 nm, \log_{10} light intensity = 18.9. Right, 405 nm, \log_{10} light intensity = 14. Black bars (2 s) and arrows (100 ms), stimulus timing. Two-photon images of GCaMP6s-expressing cone axon terminals (white circles), left of the response curves. Scale bar 5 μm . **(C)** WT cone response amplitudes ($\Delta F/F$) for Group 1 and 2. Note that two-photon functional imaging may lead to NIR light adaptation in wild-type cones, which may then not show strong responses to additional NIR light stimulation. **(D)** Rd1 ($n = 4$ mice) and WT (Group 1 and 2) cone response amplitudes (Z score). Rd1 cones transduced with rTRPV1 and nanorods ($\lambda_{\text{abs}} = 915$ nm). Note that due to low baseline fluorescence, rd1 cone responses were recorded with higher PMT gain, leading to lower Z scores in rTRPV1-nanorod injected rd1 retinas compared to wild-type retinas. x/y cones refers to x responding cones of the y measured. Cones were considered responding when absolute Z score values exceeded 1.5 for each stimulus repetition. **(E)** Cumulative frequency of responding rTRPV1 transduced rd1 cones with nanorods ($\lambda_{\text{abs}} = 915$ nm) for single retinas.

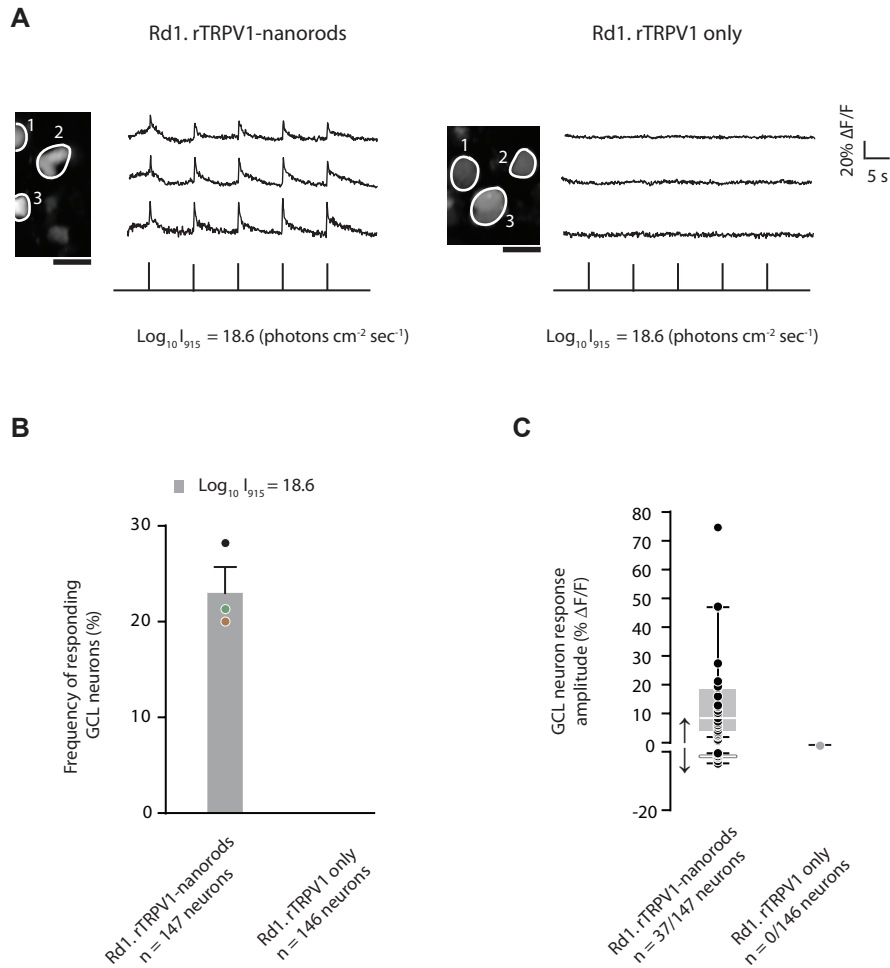


Fig. S4. Near-infrared light responses in neurons of the mouse retinal ganglion cell layer (GCL). **(A)** Example calcium responses (mean $\Delta F/F$, 5 repetitions) recorded from GCL neurons in P69-P72 rTRPV1-nanorods (left) and rTRPV1 only (right) transduced rd1 retinas in response to full-field NIR light. Vertical lines at bottom, stimulus (915 nm, 100 ms) timing. Two-photon images of Oregon Green BAPTA-1 (OGB-1) filled cell bodies (white circles), left of the response curves. Scale bar 20 μm . **(B)** Frequency of responding GCL neurons in retinas transduced with both rTRPV1 and nanorods ($\lambda_{\text{abs}} = 915$ nm, $n = 3$ mice) or with rTRPV1 only ($n = 3$ mice). Each data point (colored black, green, brown) represents the response of a single retina. **(C)** GCL neuron response amplitudes ($\Delta F/F$) at \log_{10} light intensity = 18.6. Increase (\uparrow) and decrease (\downarrow) of calcium signal are shown separately. x/y neurons refers to x responding GCL neurons of the y measured.

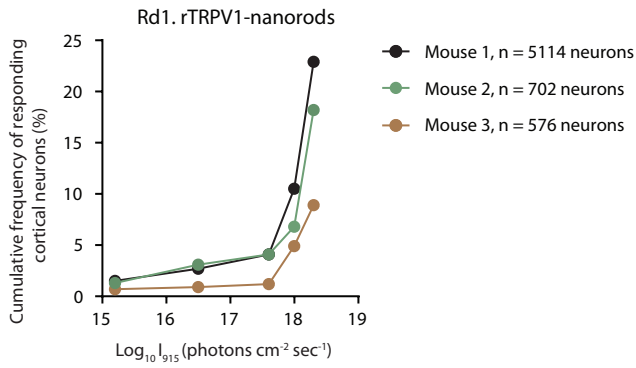
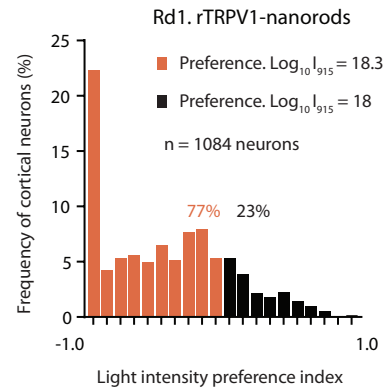
A**B**

Fig. S5. Near-infrared light responses in mouse primary visual cortex. **(A)** Cumulative frequency of responding cortical neurons in individual P51-P83 rd1 mice transduced with both rTRPV1 and nanorods ($\lambda_{\text{abs}} = 915 \text{ nm}$). **(B)** Frequency of cortical neurons as a function of the light intensity preference index (LPI) in mice transduced with rTRPV1 and nanorods ($\lambda_{\text{abs}} = 915 \text{ nm}$, $n = 3$ mice). Larger fraction (orange, LPI < 0, 77%) of neurons prefer higher intensity light (log_{10} light intensity = 18.3) over lower intensity light (log_{10} light intensity = 18) (black, LPI > 0, 23%).

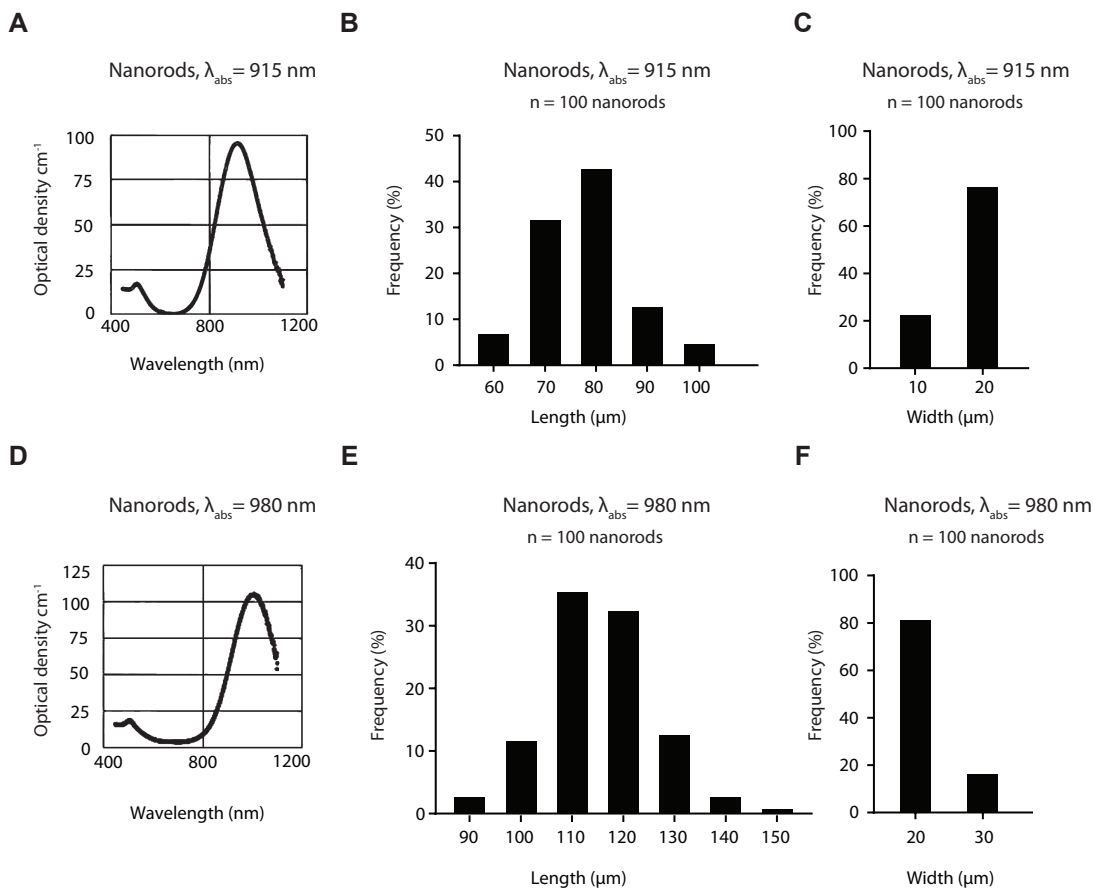


Fig. S6. Nanorod properties. **(A)** Optical density of gold nanorods tuned to 915 nm. **(B, C)** Histograms of length (B) and width (C) distributions giving rise to optical density in (A). **(D)** Optical density of gold nanorods tuned to 980 nm. **(E, F)** Histograms of length (E) and width (F) distributions giving rise to optical density in (D).

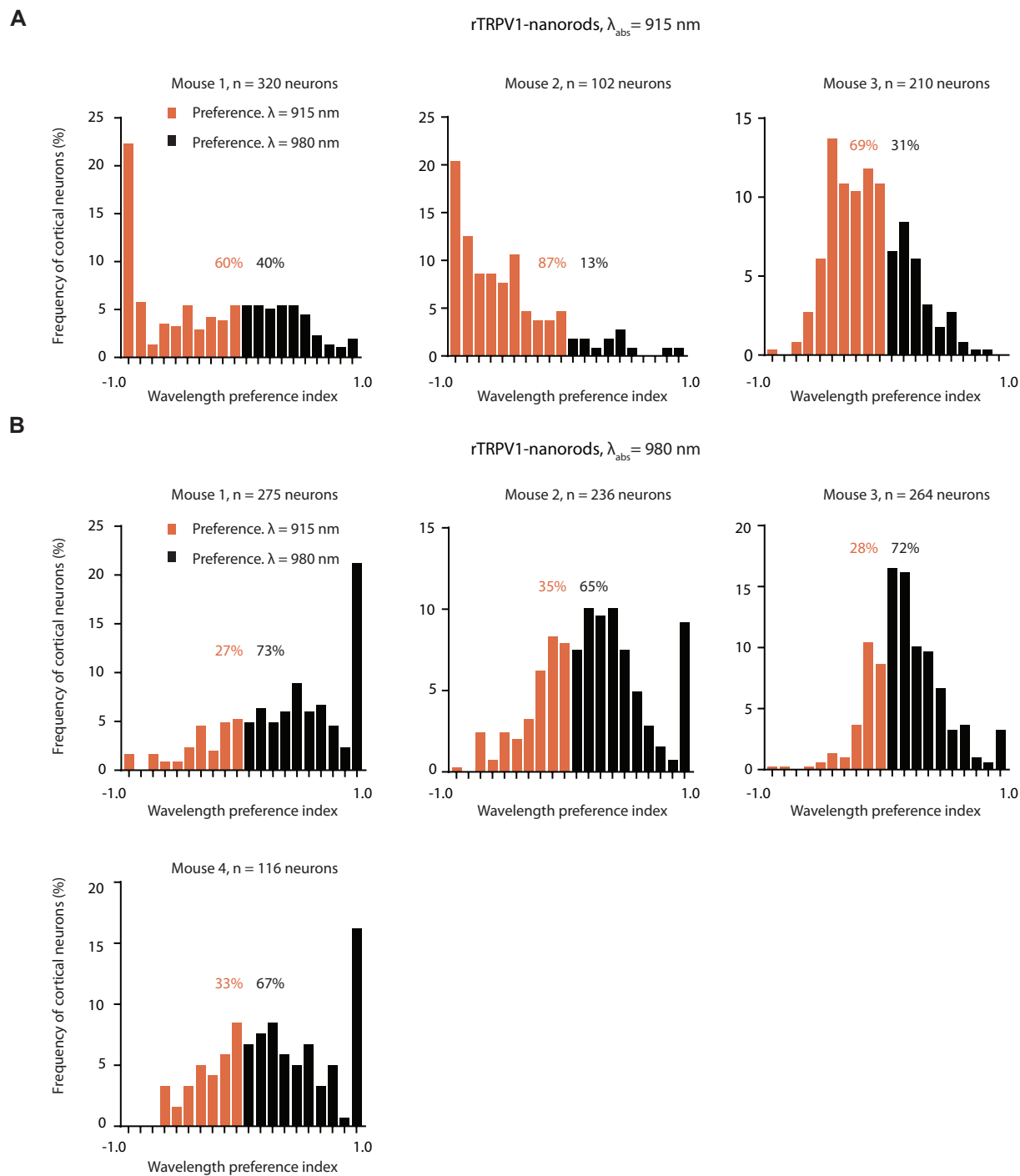


Fig. S7. Near-infrared light responses in mouse primary visual cortex. **(A)** Frequency of cortical neurons as a function of the wavelength preference index (WPI) in mice transduced with rTRPV1 and nanorods with $\lambda_{\text{abs}} = 915 \text{ nm}$ for individual animals. Log_{10} light intensity = 18.3. Larger fraction of 915 nm (WPI < 0) over 980 nm (WPI > 0) light preferring neurons. **(B)** Frequency of cortical neurons as a function of the wavelength preference index (WPI) in mice transduced with rTRPV1 and nanorods with $\lambda_{\text{abs}} = 980 \text{ nm}$ for individual animals. Log_{10} light intensity = 18.3. Larger fraction of 980 nm (WPI > 0) over 915 nm (WPI < 0) light preferring neurons. Experiments performed in P51-P71 rd1 mice.



Fig. S8. Pairwise sequence alignment between C-terminal domains of human and snake TRPA1. Ollas epitope tag insertions at amino acid 755 (EL1) and 824 (EL2) are highlighted with tilted dashed lines and the tag sequence is indicated. White text marks identical amino acid residues. Red text marks similar amino acid residues. Secondary structure elements of human TRPA1 are indicated above the sequence as spirals (helices). Regions with no assigned secondary structure are indicated by horizontal dashed lines. Black dots mark the position of every tenth amino acid of human TRPA1. EL refers to extracellular loop, AR to ankyrin repeat, S to transmembrane domain.

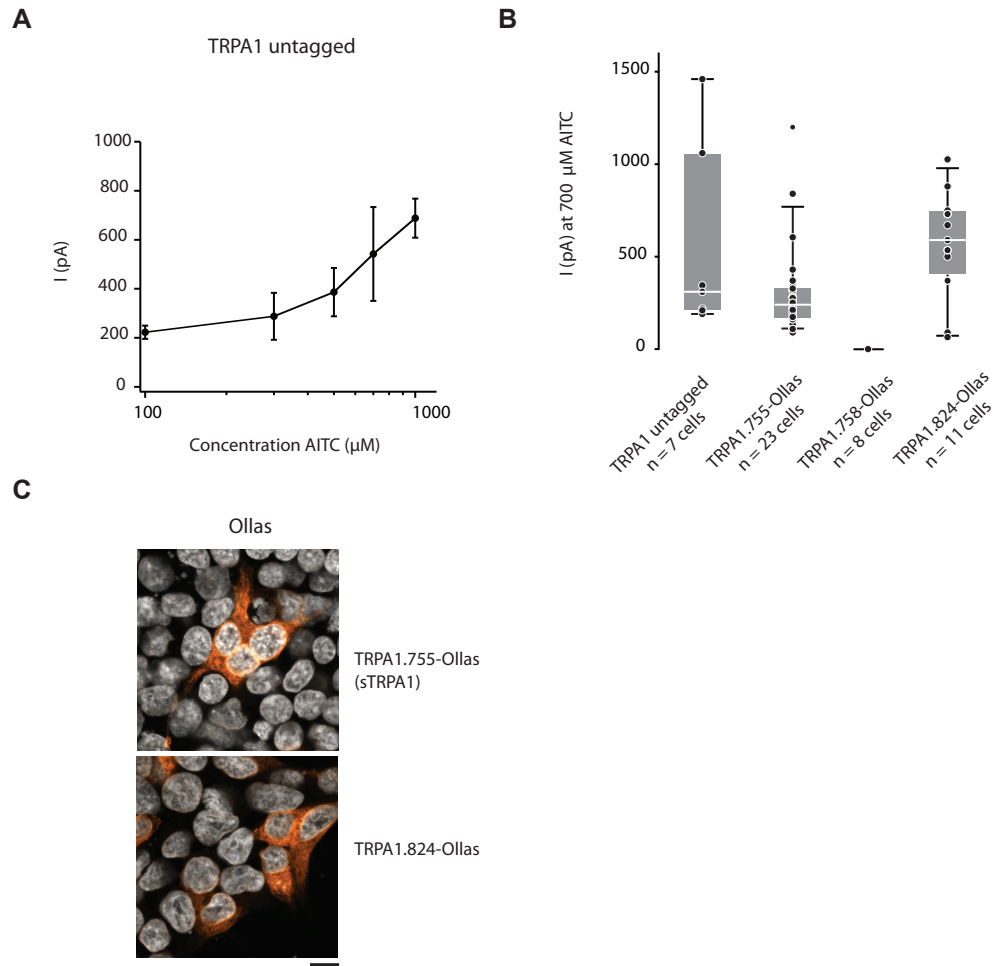


Fig. S9. Allyl isothiocyanate (AITC)-evoked whole-cell currents in HEK293T cells expressing snake TRPA1 channel variants. **(A)** AITC dose-response curve for untagged snake TRPA1. Error bars, s.e.m. **(B)** Comparison of untagged TRPA1 with tagged variants at 700 μM AITC. **(C)** Top, top views of HEK293T cells transduced with TRPA1.755-Ollas (sTRPA1), immunostained for Ollas (orange). Bottom, same views for HEK293T cells transduced with TRPA1.824-Ollas. Grey, Hoechst nuclear stain. Scale bar 10 μm .

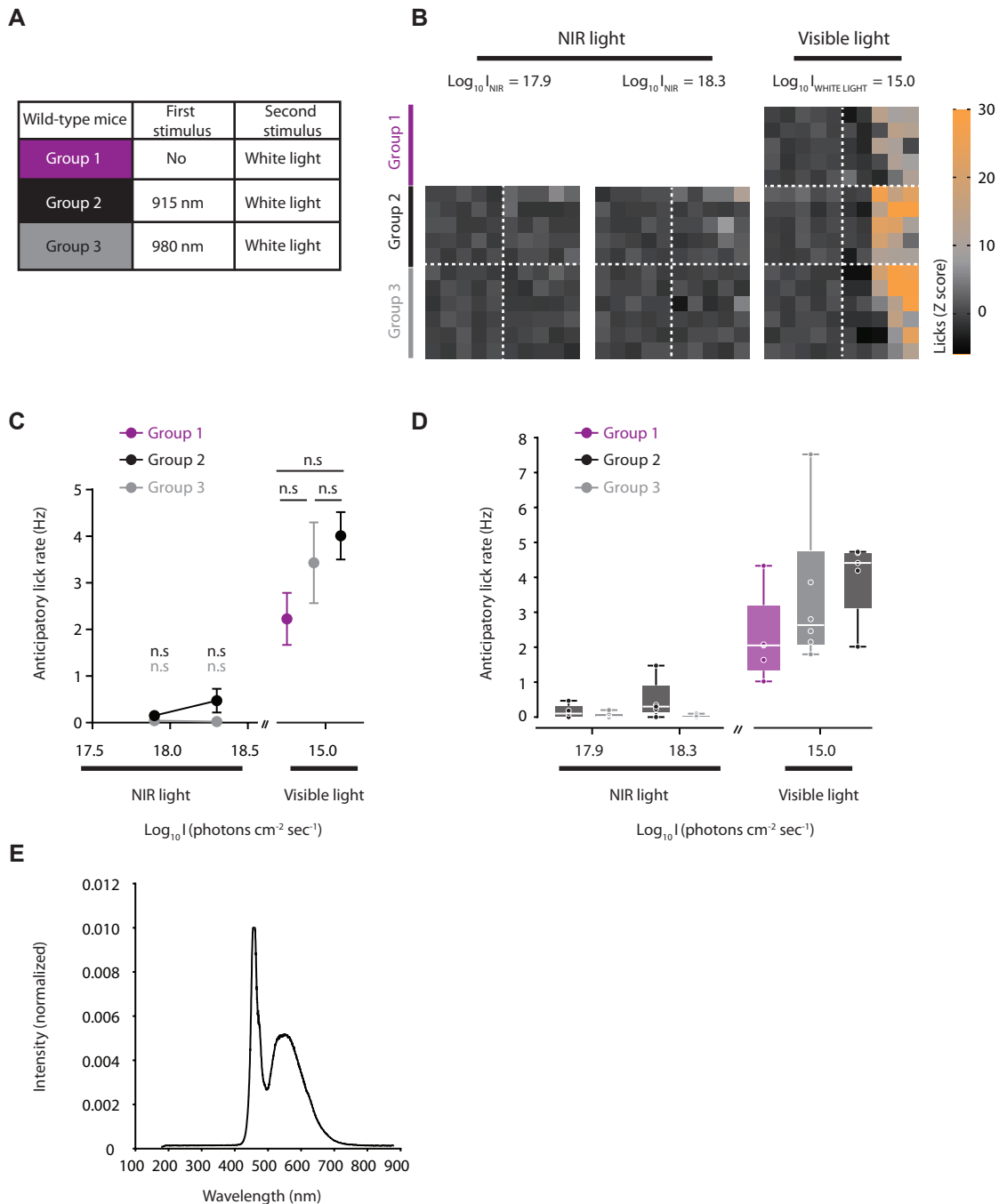


Fig. S10. Light guided wild-type mouse behavior. **(A)** Group 1 (purple, $n = 5$ mice), visible light stimulation only. Group 2 (black, $n = 5$ mice), NIR 915 nm and visible light stimulation. Group 3 (grey, $n = 6$ mice), NIR 980 nm and visible light stimulation. Full-field stimulation of one eye (200 ms) cues water presentation for head-fixed, water-restricted animals. Mice respond by licking before (anticipation) or after the appearance of water. **(B)** Lick response heat maps. Rows, responses of different mice. Columns, responses in 100 ms time bins. Responses shown separately for Group 1, 2 and 3. Left, stimulus \log_{10} light intensity = 17.9. Middle, stimulus \log_{10} light intensity = 18.3. Right, stimulus \log_{10} light intensity = 15.0 **(C)** Mean anticipatory lick rates quantified from **(B)** as a function of light intensity. Error bars, s.e.m. **(D)** Anticipatory lick rates from **(C)** for single animals. **(E)** Spectral composition of white light used in mouse behavior experiments, normalized to yield an area of one under the curve.

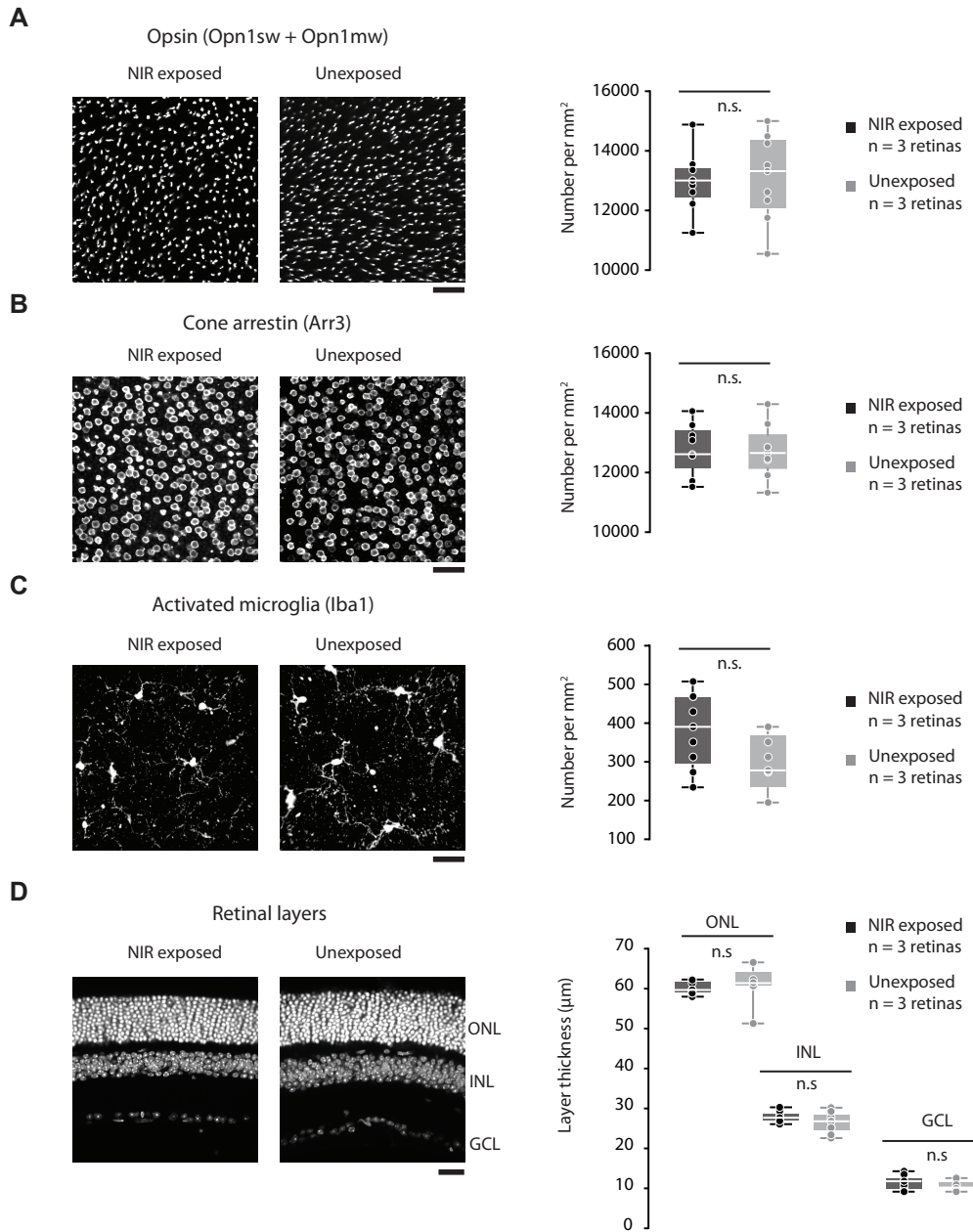


Fig. S11. Safety of prolonged near-infrared light exposure in the mouse retina. **(A, B, C)** Left, top views of wild-type retinas exposed to NIR light (915 nm) during behavioral training ($n = 3$ mice). Middle, top views of control, unexposed wild-type retinas ($n = 3$ mice). Right, number of immunostained cells per mm² in wild-type retinas exposed to NIR light (black) and control, unexposed wild-type retinas (grey). **(A)** Immunostained for short wavelength (sw) and medium wavelength (mw) Opsin (white). **(B)** Immunostained for cone photoreceptor marker, Cone arrestin (white). **(C)** Immunostained for activated microglia marker, Iba1 (white). **(D)** Cross-sections of NIR light exposed (left, $n = 3$ mice) and control, unexposed (middle, $n = 3$ mice) wild-type retinas. White, Hoechst nuclear stain. Right, thickness of retinal layers in wild-type retinas exposed to NIR light (black) and control, unexposed wild-type retinas (grey). ONL, outer nuclear layer; INL, inner nuclear layer; GCL, ganglion cell layer. In all microscopy panels, scale bars = 25 µm. In all quantification panels, each data point is collected from a different region of a retina (3 per retina).

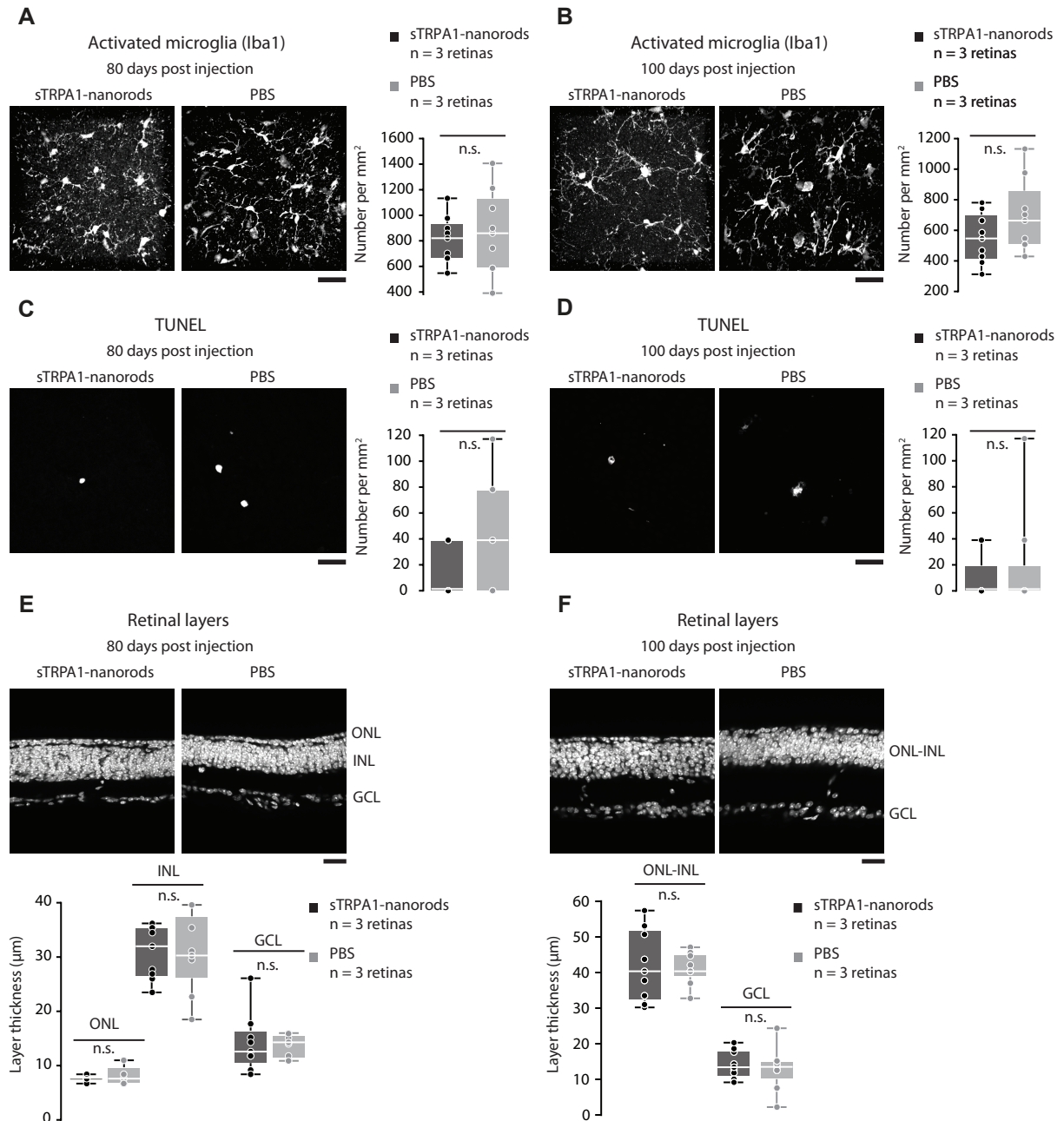


Fig. S12. Safety of intraocular sTRPA1-nanorods injection in the mouse retina. **(A-D)** Left, top views of rd1 retinas injected with sTRPA1-nanorods at P30 ($n = 3$ mice). Middle, top views of control rd1 retinas injected with PBS at P30 ($n = 3$ mice). Right, number of detected cells per mm² in rd1 retinas injected with sTRPA1-nanorods (black) and control, PBS injected rd1 retinas (grey). **(A, B)** Immunostained for activated microglia marker, Iba1 (white) 80 (A) and 100 days (B) post injection. **(B, C)** TUNEL apoptosis assay (white) 80 (C) and 100 days (D) post injection. **(E, F)** Left top, cross-sections of rd1 retinas injected with sTRPA1-nanorods at P30 ($n = 3$ mice). Right top, cross-sections of control rd1 retinas injected with PBS at P30 ($n = 3$ mice). White, Hoechst nuclear stain. Bottom, thickness of retinal layers in rd1 retinas injected with sTRPA1-nanorods at P30 (black) and control rd1 retinas injected with PBS at P30. ONL, outer nuclear layer; INL, inner nuclear layer; GCL, ganglion cell layer. **(E)** 80 days post injection. **(F)** 100 days post injection, when ONL and INL converge. In all microscopy panels, scale bars = 25 μm. In all quantification panels, each data point is collected from a different region of a retina (3 per retina).

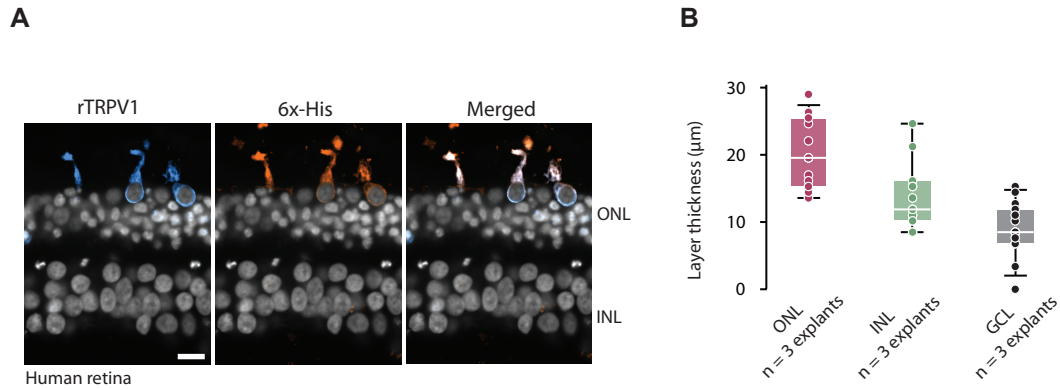


Fig. S13. Expression of rTRPV1 in photoreceptors of the *ex vivo* human retina. **(A)** Cross-sections of human retina transduced with both rTRPV1 and nanorods, immunostained for TRPV1 (left, blue), 6x-His (middle, orange), and merging the two (right). Grey, Hoechst nuclear stain. Scale bar 10 μm . **(B)** Retinal layer thickness at eight weeks post-mortem. Each data point is collected from a different region of a retinal explant (5 regions per explant). ONL, outer nuclear layer; INL, inner nuclear layer; GCL, ganglion cell layer.

	Quantification
A	Mann-Whitney U test, $P = 0.86$; TRPV1.465-6x-His, 1633 ± 164 pA, $n = 15$ cells; TRPV1, 1766 ± 276 pA, $n = 14$ cells; mean \pm s.e.m
B	Mann-Whitney U test, $P = 0.021$; TRPV1.459-6x-His, 976 ± 118 pA, $n = 19$ cells; mean \pm s.e.m
C	$55 \pm 10\%$, mean \pm s.d; $n = 12813$ cones per mm^2 (IO), $n = 7042$ TRPV1 positive cones per mm^2
D	$98 \pm 1.6\%$, mean \pm s.d; $n = 7216$ TRPV1 positive cells per mm^2 , $n = 7042$ TRPV1 positive cones per mm^2
E	Mann-Whitney U test, $P = 0.71$; $n = 7042$ TRPV1 positive cones per mm^2 , $n = 6820$ 6x-His positive cones per mm^2
F	Mann-Whitney U Test, $P = 0.057$; $\Delta F/F$; rTRPV1-nanorods, $325 \pm 59\%$, $n = 4$ mice; WT, $75 \pm 0.5\%$, $n = 3$ mice; mean \pm s.e.m
G	Z score; rTRPV1-nanorods, 6.2 (2.1-19.5), $n = 4$ mice; WT, 14 (3.1-38.9), $n = 3$ mice; mean (range)
H	Mann-Whitney U Test, $P = 0.036$; rTRPV1-nanorods, 21.1%, $n = 3$ mice; control, 3.1%, $n = 5$ mice
I	Wilcoxon Matched-Pairs Signed Rank Test, $P = 0.031$; 70% of neurons with WPI > 0 , $n = 4$ mice
J	Wilcoxon Matched-Pairs Signed Rank Test, $P = 0.031$; 67% of neurons with WPI < 0 , $n = 3$ mice
K	Mann-Whitney U test, $P = 0.22$; TRPA1.755-Ollas, 315 ± 56 pA, $n = 23$ cells; TRPA1, 542 ± 192 pA, $n = 7$ cells; mean \pm s.e.m
L	Mann-Whitney U test, $P = 0.52$; TRPA1.824-Ollas, 566 ± 83 pA, $n = 11$ cells; mean \pm s.e.m
M	$50 \pm 13\%$, mean \pm s.d; $n = 12813$ cones per mm^2 (IO), $n = 6362$ Ollas positive cones per mm^2
N	$99 \pm 0.8\%$, mean \pm s.d; $n = 6403$ Ollas positive cells per mm^2 , $n = 6362$ Ollas positive cones per mm^2
O	Mann-Whitney U test, $P = 0.70$; rTRPV1-nanorods, 0.17 ± 0.12 Hz, $n = 9$ mice; control, 0.043 ± 0.02 Hz, $n = 10$ mice; mean \pm s.e.m
P	Mann-Whitney U test, $P = 0.019$; sTRPA1-nanorods, 0.75 ± 0.31 Hz, $n = 9$ mice; mean \pm s.e.m
Q	Mann-Whitney U test, $P = 0.001$; rTRPV1-nanorods, 1.7 ± 0.34 Hz, $n = 9$ mice; control, 0.11 ± 0.057 Hz, $n = 10$ mice; mean \pm s.e.m
R	Mann-Whitney U test, $P = 0.019$; sTRPA1-nanorods, 3.4 ± 0.64 Hz, $n = 9$ mice; mean \pm s.e.m
S	Mann-Whitney U test, $P = 0.19$; sTRPA1-nanorods, 3.4 ± 0.64 Hz, $n = 9$ mice; wild-type group 1, 2.2 ± 0.56 Hz, $n = 5$ mice; mean \pm s.e.m
T	Mann-Whitney U test, $P = 0.52$; rTRPV1-nanorods, 1.7 ± 0.34 Hz, $n = 9$ mice; wild-type group 1, 2.2 ± 0.56 Hz, $n = 5$ mice; mean \pm s.e.m
U	$94.5 \pm 4.2\%$, mean \pm s.d; $n = 2583$ rTRPV1 positive cells per mm^2 , $n = 2477$ rTRPV1 positive photoreceptors per mm^2

Table S1. Details of quantification and statistical tests.

Nanorod properties	Nanorods $\lambda_{\text{abs}} = 915 \text{ nm}$ Anti-6x-His	Nanorods $\lambda_{\text{abs}} = 980 \text{ nm}$ Anti-6x-His	Nanorods $\lambda_{\text{abs}} = 915 \text{ nm}$ Anti-Ollas
Surface plasmon resonance (nm)	905–915	980–990	903–915
Concentration (nanorods per mL)	10^{13}	10^{13}	10^{13}
IgG (per nanorod)	18–22	24–25	19–20
pH	7	7	7
Solution	PBS	PBS	PBS
Zeta Potential (mV)	-18	-15	-16

Table S2. Nanorod properties.

Plasmids generated	TRP origin	Promoter	Experiment
pAAV-EF1a-TRPV1-T2A-GFP	rat	EF1a	HEK293T
pAAV-EF1a-TRPV1.459-6x-His-T2A-mCherry	rat	EF1a	HEK293T
pAAV-EF1a-TRPV1.465-6x-His-T2A-mCherry	rat	EF1a	HEK293T
pAAV-EF1a-TRPA1-T2A-GFP	snake	EF1a	HEK293T
pAAV-EF1a-TRPA1.755-Ollas-T2A-mCherry	snake	EF1a	HEK293T
pAAV-EF1a-TRPA1.758-Ollas-T2A-mCherry	snake	EF1a	HEK293T
pAAV-EF1a-TRPA1.824-Ollas-T2A-mCherry	snake	EF1a	HEK293T
pAAV-mCar-TRPV1.465-6x-His (rTRPV1)	rat	mCar	Mouse
pAAV-mCar-TRPA1.755-Ollas (sTRPA1)	snake	mCar	Mouse
pAAV-CAG-TRPV1.465-6x-His	rat	CAG	Human

Table S3. TRP plasmid list. mCar refers to photoreceptor specific mouse cone arrestin promoter.

Experiment	I₉₁₅ (photons cm ⁻² s ⁻¹)	Log₁₀ I₉₁₅ (photons cm ⁻² s ⁻¹)	I₉₁₅ (photons m ⁻² s ⁻¹)	Power (Watts m ⁻²)	Photoisomerization cone, λ _{abs} = 510 nm (R* cone ⁻¹ s ⁻¹)	Photoisomerization cone, λ _{abs} = 360 nm (R* cone ⁻¹ s ⁻¹)
Mouse retina, cones	5.36E+17	17.73	5.36E+21	1.16E+03	1.32E-02	4.57E-11
	1.81E+18	18.26	1.81E+22	3.93E+03	4.45E-02	1.54E-10
	3.17E+18	18.50	3.17E+22	6.88E+03	7.80E-02	2.70E-10
	4.57E+18	18.66	4.57E+22	9.92E+03	1.12E-01	3.90E-10
	5.97E+18	18.78	5.97E+22	1.30E+04	1.47E-01	5.09E-10
	7.38E+18	18.87	7.38E+22	1.60E+04	1.82E-01	6.29E-10
	8.74E+18	18.94	8.74E+22	1.90E+04	2.15E-01	7.45E-10
Mouse retina, ganglion cells	3.73E+18	18.57	3.73E+22	8.09E+03	9.18E-02	3.18E-10
Mouse V1, cortical neurons	1.68E+15	15.23	1.68E+19	3.65E+00	4.13E-05	1.43E-13
	3.00E+16	16.48	3.00E+20	6.51E+01	7.38E-04	2.56E-12
	4.24E+17	17.63	4.24E+21	9.20E+02	1.04E-02	3.61E-11
	9.33E+17	17.97	9.33E+21	2.02E+03	2.30E-02	7.95E-11
	2.00E+18	18.30	2.00E+22	4.34E+03	4.92E-02	1.71E-10
Mouse behavior	8.48E+17	17.93	8.48E+21	1.84E+03	2.09E-02	7.23E-11
	1.87E+18	18.27	1.87E+22	4.06E+03	4.60E-02	1.59E-10
Human retina	2.25E+15	15.35	2.25E+19	4.88E+00	5.54E-05	1.92E-13
	9.06E+15	15.96	9.06E+19	1.97E+01	2.23E-04	7.72E-13
	1.17E+18	18.07	1.17E+22	2.54E+03	2.88E-02	9.97E-11
	2.46E+18	18.39	2.46E+22	5.34E+03	6.05E-02	2.10E-10
	8.74E+18	18.94	8.74E+22	1.90E+04	2.15E-01	7.45E-10

Table S4. Light intensities. V1 refers to primary visual cortex.

Chapter 2

miRNAs 182 and 183 are necessary to maintain adult cone photoreceptor outer segments and visual function

Busskamp V, Krol J, Nelidova D, Daum J, Szikra T, Tsuda B, Jüttner J, Farrow K, Scherf BG, Alvarez CP, Genoud C, Sothilingam V, Tanimoto N, Stadler M, Seeliger M, Stoffel M, Filipowicz W, Roska B.

Neuron. (August 2014)

Abstract

The outer segments of cones serve as light detectors for daylight color vision, and their dysfunction leads to human blindness conditions. We show that the cone-specific disruption of DGCR8 in adult mice led to the loss of miRNAs and the loss of outer segments, resulting in photoreceptors with significantly reduced light responses. However, the number of cones remained unchanged. The loss of the outer segments occurred gradually over 1 month, and during this time the genetic signature of cones decreased. Reexpression of the sensory-cell-specific miR-182 and miR-183 prevented outer segment loss. These miRNAs were also necessary and sufficient for the formation of inner segments, connecting cilia and short outer segments, as well as light responses in stem-cell-derived retinal cultures. Our results show that miR-182- and miR-183-regulated pathways are necessary for cone outer segment maintenance in vivo and functional outer segment formation in vitro.

miRNAs 182 and 183 Are Necessary to Maintain Adult Cone Photoreceptor Outer Segments and Visual Function

Volker Busskamp,^{1,5,6} Jacek Krol,^{1,5} Dasha Nelidova,^{1,2} Janine Daum,^{1,2} Tamas Szikra,¹ Ben Tsuda,¹ Josephine Jüttner,¹ Karl Farrow,^{1,7} Brigitte Gross Scherf,¹ Claudia Patricia Patino Alvarez,¹ Christel Genoud,¹ Vithiyanjali Sothilingam,³ Naoyuki Tanimoto,³ Michael Stadler,¹ Mathias Seeliger,³ Markus Stoffel,⁴ Witold Filipowicz,^{1,2,*} and Botond Roska^{1,*}

¹Neural Circuit Laboratories, Friedrich Miescher Institute for Biomedical Research, 4058 Basel, Switzerland

²University of Basel, 4058 Basel, Switzerland

³Division of Ocular Neurodegeneration, Institute for Ophthalmic Research, Department of Ophthalmology, Eberhard-Karls University, 72076 Tübingen, Germany

⁴Institute for Molecular Health Sciences, ETH, 8093 Zürich

⁵Co-first author

⁶Present address: Department of Genetics, Harvard Medical School, Boston, MA 02115, USA

⁷Present address: Neuro-Electronics Research Flanders, 3001 Leuven, Belgium

*Correspondence: witold.filipowicz@fmi.ch (W.F.), botond.roska@fmi.ch (B.R.)

<http://dx.doi.org/10.1016/j.neuron.2014.06.020>

SUMMARY

The outer segments of cones serve as light detectors for daylight color vision, and their dysfunction leads to human blindness conditions. We show that the cone-specific disruption of DGCR8 in adult mice led to the loss of miRNAs and the loss of outer segments, resulting in photoreceptors with significantly reduced light responses. However, the number of cones remained unchanged. The loss of the outer segments occurred gradually over 1 month, and during this time the genetic signature of cones decreased. Reexpression of the sensory-cell-specific miR-182 and miR-183 prevented outer segment loss. These miRNAs were also necessary and sufficient for the formation of inner segments, connecting cilia and short outer segments, as well as light responses in stem-cell-derived retinal cultures. Our results show that miR-182- and miR-183-regulated pathways are necessary for cone outer segment maintenance in vivo and functional outer segment formation in vitro.

INTRODUCTION

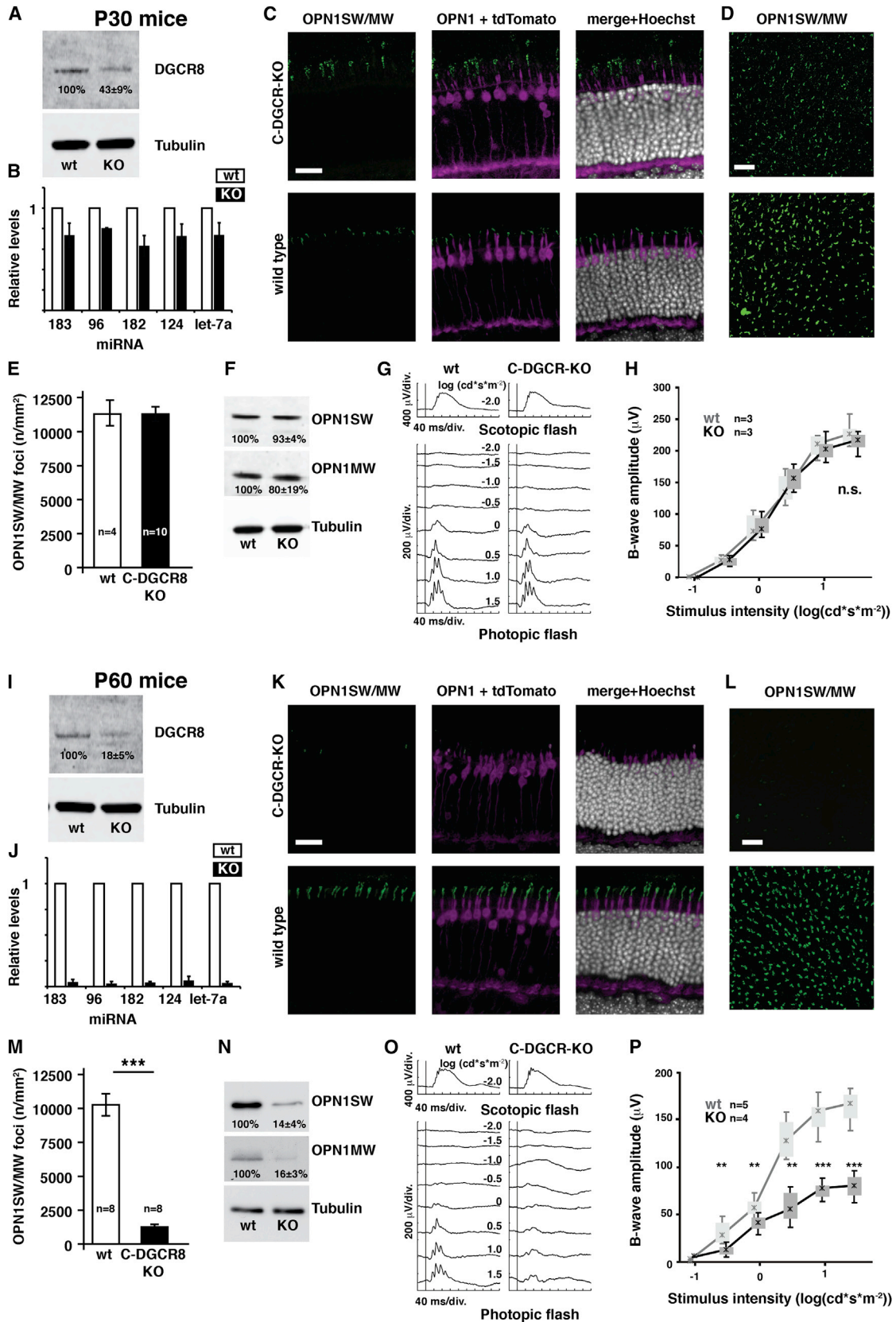
Vertebrate image-forming vision relies on two types of photoreceptors, cones and rods, which capture light using their outer segment, an organelle with a stack of membrane disks that host the photopigments. The light-induced signal travels via an intracellular route, including the connecting cilium, the inner segment, the cell body, the axon, and the axon terminal, before it is transmitted to downstream retinal cells. The connecting cilium is a microtubule-containing structure that is anchored to a basal body derived from a centrosome, and it connects the

mitochondria-rich inner segment and the outer segment (Pearring et al., 2013). The outer segment is dynamically renewed: new membrane folds are added from the end that interfaces the connecting cilium, and old membrane folds are phagocytized by pigment epithelial cells from the other end (Mustafi et al., 2009).

Cones are less sensitive to light than rods and, therefore, operate at higher light intensities, characteristic of daytime, while rods are used during nighttime conditions. In humans, high-resolution daylight vision, which is necessary for reading and for recognizing faces, depends almost entirely on cones. The loss of cone outer segments or their function in adulthood occurs in many photoreceptor diseases and can lead to blindness (Léveillard and Sahel, 2010; Sahel and Roska, 2013). To preserve these organelles, or to regenerate them, entirely or partially (Thompson et al., 2014), requires knowledge of the molecular pathways that control their maintenance in healthy adults (Léveillard and Sahel, 2010).

MicroRNAs (miRNAs) are posttranscriptional repressors of gene expression. Their biogenesis occurs in two steps. The primary RNA transcripts, pri-miRNAs, are cleaved by the Drosha/DGCR8 complex into pre-miRNAs, which are further processed by Dicer to become mature miRNAs (Krol et al., 2010a). In animals, the majority of investigated miRNAs base pair imperfectly with messenger RNA (mRNA) sequences in the 3' UTR, which leads to translational repression, deadenylation, and degradation of target mRNAs. miRNAs function as part of ribonucleoprotein (RNP) complexes, miRNPs, with the best-characterized components of miRNPs represented by proteins from the Argonaute (AGO) and GW182 families.

The lack of all, or particular, miRNAs during development leads to various defects in the retina (Sundermeier and Palczewski, 2012), including retinal degeneration (Damiani et al., 2008; Lumayag et al., 2013; Zhu et al., 2011) or cone death (Sanuki et al., 2011). Targeted disruption of *Rnrc3*, the dominant source of miR-124, alters the maturation of cone photoreceptors, which results in increased apoptosis and improper cone migration



(legend on next page)

(Sanuki et al., 2011). A transgenic anti-miRNA “sponge” mouse model that reduced the activities of all three miRNAs in the miR-183/96/182 cluster, which is mainly expressed in sensory neurons (Xu et al., 2007), showed increased bright-light-induced retinal degeneration, although neither morphological nor functional differences have been observed under laboratory lighting conditions between transgenic and wild-type mice (Zhu et al., 2011). Characterization of a mouse line in which a gene-trap construct was inserted downstream of the first exon of the miR-183/96/182 gene revealed an almost complete lack of all three miR-183/96/182 cluster miRNAs in the retina. This mouse line showed age-dependent retinal degeneration, as well as increased susceptibility to light damage. Functional defects have been observed at the photoreceptor synapse at 5 weeks of age, while photoreceptor dysfunction was detectable in 6-month-old animals. Analysis of gene expression at times when there was no detectable histological evidence of retinal degeneration identified decreased expression of genes involved in synaptogenesis as well as in cone phototransduction (Lumayag et al., 2013). Another study (Jin et al., 2009) did not find any obvious defect in mice with a knockout of only miR-182, possibly because of developmental compensation since miR-182 and miR-183 have similar seed sequences.

So far, all studies relating the effects of specific miRNAs to retinal structure and function have been performed in animal models in which genetic manipulation has led to miRNA changes during both development and adulthood. Many of these studies, which have been performed cell-type-nonspecifically, concluded that the developmental loss of specific miRNAs leads to photoreceptor degeneration.

How miRNAs contribute to the function of adult cones is not understood. To address this question, we developed a mouse model in which miRNA depletion occurs specifically in cones, after the full development of the retina. We used this model to dynamically follow the subcellular structure, function, and transcriptome of cones. We found that the depletion of miRNAs in adult cones led to two major changes. First, the cone outer segments were lost and, therefore, the light responses of cones were significantly reduced. The loss of the outer segments occurred gradually over a 1-month period. However, cones did not degenerate, the number of cone cell bodies did not change when most of the outer segments were lost, and apoptotic markers did not increase. Importantly, the reexpression of the sensory-cell-specific miR-182 and miR-183 in cones prevented

outer segment loss. Second, the genetic identity of cones, quantified by the expression of cone-specific genes, decreased significantly after miRNA depletion.

Furthermore, we found that miRNAs of the miR-183/96/182 cluster accelerated the formation of photoreceptor distal structures, such as the inner segments and connecting cilia, in embryonic stem (ES)-cell-derived retinal cultures. Remarkably, in ES-cell-derived cultures, these miRNAs also induced the formation of short outer segments that contained a stack of membrane disks, which are characteristic structures of outer segments in normal photoreceptors. The miRNA-transduced photoreceptors of ES-cell-derived cultures responded to light with the same response polarity, i.e., hyperpolarization, as normal photoreceptors. Our findings suggest that miR-183/96/182 cluster miRNAs regulate the supply of molecular components to the apical membranes of photoreceptors in order to control the maintenance of outer segments.

RESULTS

Depletion of miRNAs in Adult Cones Leads to the Loss of Outer Segments

To deplete miRNAs from adult cones, we genetically disrupted the Drosha/DGCR8 miRNA-processing machinery by crossing mice with conditional null *Dgcr8* alleles (Yi et al., 2009) and mice expressing *Cre* recombinase postnatally specifically in cones (D4-Cre; Le et al., 2004). We call the mouse line that is homozygous for the conditional null *Dgcr8* allele and heterozygous for the *Cre* allele C-DGCR-KO. The morphology of cones in the C-DGCR-KO mice was revealed by crossing it with the reporter mouse line (Ai9; Madisen et al., 2010) conditionally expressing fluorescent tdTomato protein. D4-Cre mice or D4-Cre mice crossed with Ai9 mice, served as “wild-type” controls. We expressed various genes specifically in C-DGCR-KO or wild-type cones by infection with conditional adeno-associated viral vectors (AAVs). Cones were examined in retinal sections, in retinal whole mounts, and in isolation after fluorescence-activated cell sorting. We detected *Cre* expression earliest at postnatal day 6 (P6) (Figure S1A available online). However, at P30, a time when the retina is fully developed, immunohistochemistry revealed no appreciable difference in DGCR8 signal between C-DGCR-KO and wild-type cone nuclei (Figures S1B–S1D). Quantitative western blot analysis of isolated cones showed 43% DGCR8 levels compared to wild-type (Figure 1A), but the

Figure 1. Cones of P60 C-DGCR-KO Mice Lose Their Outer Segments and Their Function

(A–H) P30 mice.

(I–P) P60 mice.

(A and I) Quantitative DGCR8 western blots of isolated wild-type (WT) and knockout (KO) cones (n = 3). Tubulin protein served as a loading control.

(B and J) qPCR measurement of selected mature miRNAs (n = 3).

(C and K) Cross-sections of immunostained C-DGCR-KO (top row) and wild-type (bottom row) retinas for OPN1SW/MW (green), merged with tdTomato-labeled cones (magenta), and additionally merged with Hoechst dye stained nuclei (white).

(D and L) Top view of corresponding OPN1SW/MW (green) signal.

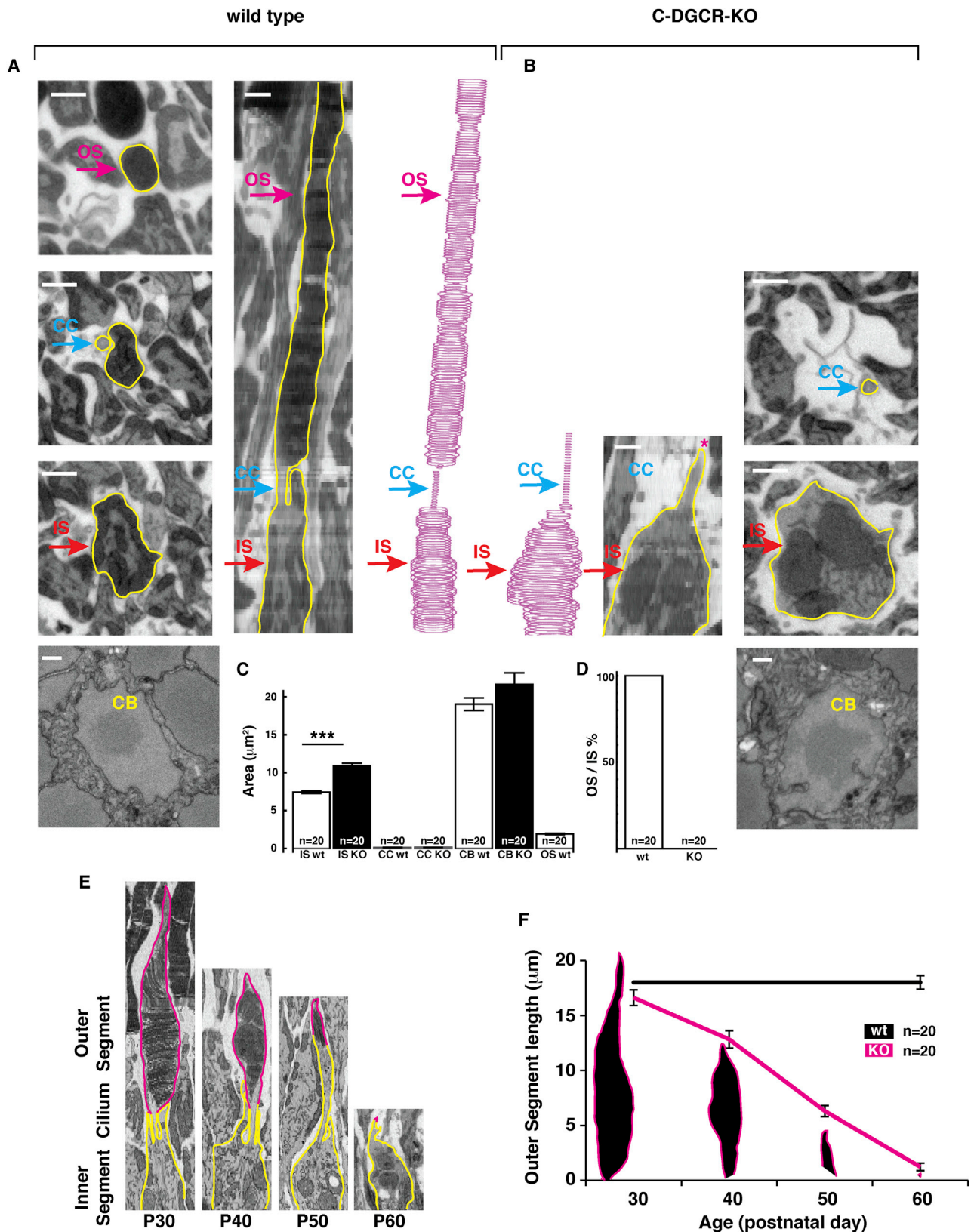
(E and M) Quantification of immunostained OPN1SW/MW foci, corresponding to outer segments.

(F and N) Quantitative OPN1SW and OPN1MW western blots of isolated WT and KO cones (n = 3).

(G and O) Photopic (reflecting mostly cone activity) electroretinogram of WT and KO retinas stimulated with light of indicated intensities. As a control, a scotopic (reflecting mostly rod activity) electroretinogram is shown at the top.

(H and P) Quantification of electroretinogram b-wave amplitudes, data for each light intensity are shown in box-whisker plots.

(O and P) Animals tested at P56. Scale bar, 20 μ m. Error bars, SEM. See also Figure S1.



(legend on next page)

levels of mature miRNAs decreased by only 20%–25% (Figure 1B). The slow depletion of DGCR8 protein (and consequently the miRNAs) is likely due to its high stability. DGCR8 stability is known to be modulated by its phosphorylation and interactions with other proteins (Cheng et al., 2014; Han et al., 2009; Herbert et al., 2013): these phenomena possibly also stabilizing the protein in cones.

At P30, cone morphology and their opsin-labeled (OPN1SW and OPN1MW) outer segment distribution in whole-mount retinas assayed by immunohistochemistry, the opsin mRNA and protein levels in isolated cones tested by quantitative PCR (qPCR) and western blot, and cone function tested in vivo using electroretinography were similar in C-DGCR-KO and wild-type mice (Figures 1C–1H and S1E–S1H). The observation that adult cones of C-DGCR-KO mice at P30 had nearly normal mature miRNA levels (Figure 1B), as well as normal structure and function (Figures 1 and S1), indicated a proper development and functional maturation of cone photoreceptors and allowed us to investigate the effect of progressive loss of mature miRNAs in adult cones.

In contrast to P30, DGCR8 immunostaining in cone nuclei was not detectable on retinal sections at P60 (Figure S1B) and amounted to only 18% of wild-type levels in a western blot analysis of isolated cones (Figure 1I). Moreover, miRNA levels in isolated P60 C-DGCR-KO cones, tested by qPCR, were 95% lower than in wild-type cones (Figure 1J; see also below). Hence, at P60 the DGCR8 function was largely lost and, consequently, miRNAs were depleted from cones. Importantly, in this miRNA-depleted cone state, we found that the number of cone outer segments labeled with cone opsins was reduced by 90% (Figures 1K–1M). Opsin mRNA and protein expression in isolated cones were also markedly reduced (Figures 1M, 1N, and S1F). Since the number of cones counted in whole-mount retinas was similar in C-DGCR-KO and wild-type mice (Figures S1G and S1H), the loss of opsin staining was not due to the death of cones.

Outer segments and opsin expression are important for light detection. We therefore tested the ability of the P60 C-DGCR-KO retina to respond to light stimuli in vivo and ex vivo. In vivo, cone-mediated photoresponses were significantly reduced compared to wild-type and P30 C-DGCR-KO retinas (Figures 1O and 1P). Similar to in vivo recordings, ex vivo single ganglion cell responses measured using whole-cell patch clamp at high light levels, reflecting cone vision, were significantly reduced (Figure S1I). Therefore, by P60 the majority of cones from C-DGCR-KO mice had lost their opsin expression and become nonfunctional but had not died.

To reveal fine morphological changes in the P60 opsin-less cones, we reconstructed $50 \times 50 \times 170 \mu\text{m}^2$ cubes of the outer retina of P30 and P60 C-DGCR-KO and of P60 wild-type mice

using serial block-face scanning electron microscopy (EM) (Denk and Horstmann, 2004). This allowed us to visualize cones and rods at the ultrastructural level in 3D (Figures 2A and 2B). Cones could be distinguished from rods based on a number of criteria (Carter-Dawson and LaVail, 1979), the most robust being the organization of heterochromatin in the nucleus (Solovei et al., 2009) (Figures S1C, S1D, and S2A–S2C). All P60 C-DGCR-KO cones lacked outer segments (Figures 2B–2D). The diameter of inner segments was larger than in wild-type mice (Figures 2B and 2C), and we detected oversized mitochondria (Figures 2B and S2D). Cone cell bodies and their nuclear organization were intact and did not appear to be different from wild-type (Figures 2A, 2B, and S2C). Cone morphology in P30 C-DGCR-KO mice and rod photoreceptor morphology in both P30 and P60 C-DGCR-KO mice appeared normal (data not shown), with the exception of the enlarged mitochondria in P30 C-DGCR-KO cones (Figure S2C). To determine the time course of outer segment loss, we 3D-reconstructed the outer retina at 10-day intervals between P30 and P60. P30 C-DGCR8-KO cone outer segments had similar length to wild-type, but at subsequent time points they shortened in a linear fashion until they became undetectable at P60 (Figures 2E and 2F). This indicates that DGCR8-dependent pathways are necessary to maintain cone outer segments in adult mice.

To test whether the loss of opsin can be prevented when outer segments are shortening, we reintroduced *Dgcr8* to P45 C-DGCR-KO cones via conditional AAV-mediated delivery (Figure 3A). At P90, DGCR8 and opsin protein levels in cones were significantly higher in AAV-infected C-DGCR-KO retinas than in uninfected control retinas, and opsin localized to the distal tip of cones (Figures 3B and 3C). Therefore, the reexpression of DGCR8 was sufficient to reinitiate opsin expression and to target this protein to the distal compartments of cones.

miR-182 and miR-183 Are Sufficient for the Maintenance of Outer Segments

The lack of DGCR8 could cause defects either through miRNA-dependent or -independent pathways (Macias et al., 2012). If the loss of outer segments was due to miRNA deficiency, reexpressing the relevant miRNA in the absence of DGCR8 should prevent the loss. We used next-generation sequencing of RNA from isolated wild-type P60 cones to determine the most highly expressed miRNAs as candidates for controlling outer segment maintenance. We then designed a strategy to express miRNAs in the absence of DGCR8 in vivo. The expression pattern of miRNAs was highly uneven, with a single miRNA, miR-182, representing 64% of all miRNA reads (Figure 3D). Only four other miRNAs were found in more than 1% of reads. Since miR-182 and miR-183 (third most abundant, 4% of reads) are processed (jointly with miR-96) from the same primary transcript and have

Figure 2. Cone Outer Segments of C-DGCR-KO Mice Shorten Gradually from P30 to P60

(A and B) Cone morphology revealed by serial block-face scanning electron microscopy in P60 WT (A) and P60 KO (B) mice. Outer segment (OS), connecting cilium (CC), inner segment (IS), and cell body (CB) are highlighted. Asterisk in (B) indicates the tip of the connecting cilium. Scale bar, 1 μm . (C) Quantification of IS, CC, CB, and OS cross-section area of P60 WT (white) and P60 KO (black) cones. (D) Quantification of the OS to IS ratio. (E) Side views of reconstructed C-DGCR8-KO cones at P30, P40, P50, and P60. (F) Quantification of OS length at P30, P40, P50, and P60. Error bars, SEM. See also Figure S2.

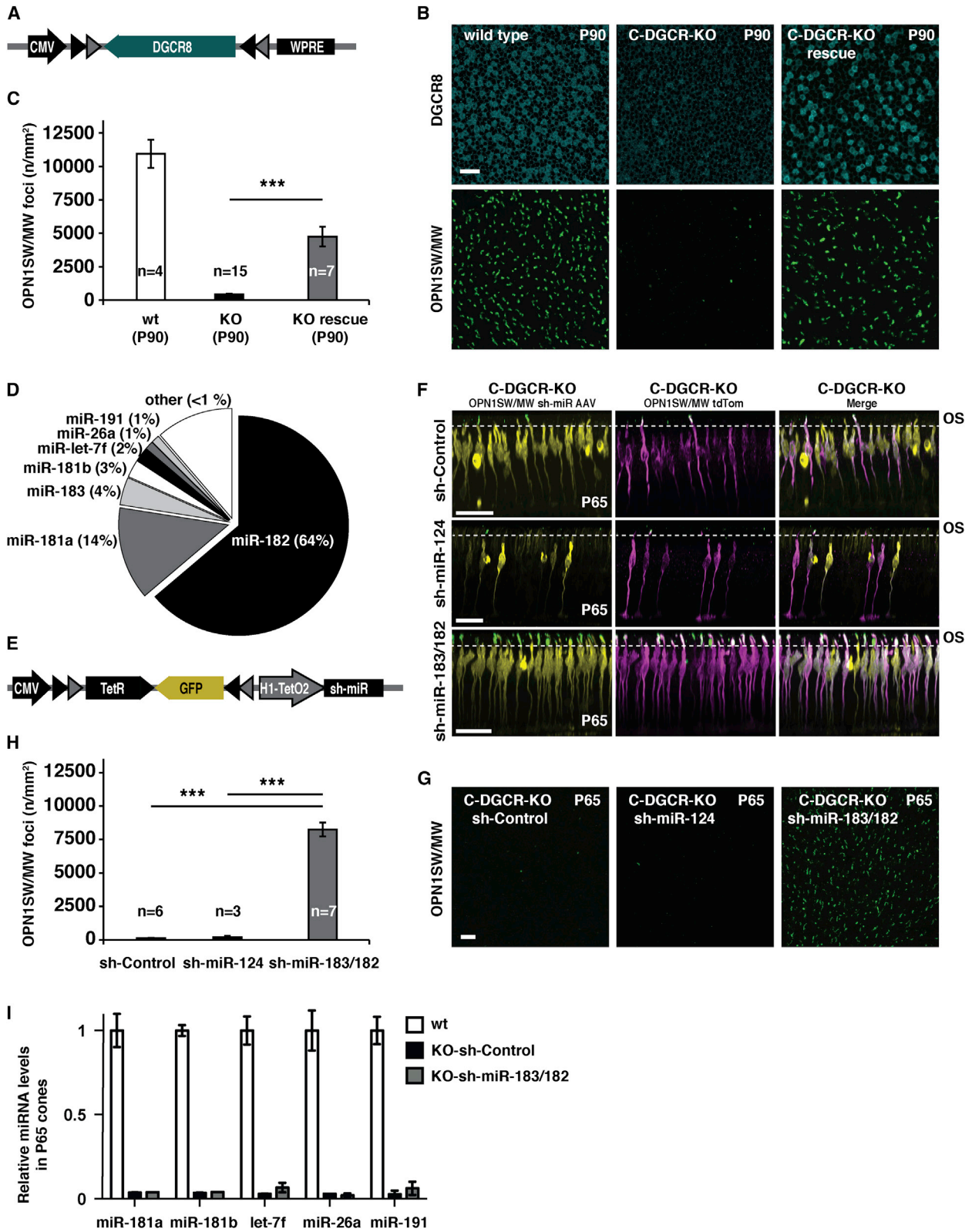


Figure 3. The Reintroduction of miR-182/183 Is Sufficient to Maintain Cone Outer Segments

(A) Conditional DGCR8 AAV expression cassette driven by the CMV promoter. In the presence of Cre, the DNA segment flanked by two different loxP sites (gray and black triangles) is inverted (Atasoy et al., 2008), enabling DGCR8 expression. WPRE, woodchuck hepatitis virus posttranscriptional regulatory element.

(legend continued on next page)

related seed sequences (Karali et al., 2007; Ryan et al., 2006; Xu et al., 2007), we expressed these two together. We also expressed miR-124, since a lack of miR-124 during development has been shown to lead to the loss of opsin expression and to cone death (Sanuki et al., 2011). To bypass the need for Drosha/DGCR8, we generated short hairpin RNAs resembling pre-miRNAs (sh-miRs), which only need Dicer to produce mature miRNA mimics (Figures 3E, S3A, and S3B). We verified that expression of these sh-miRs in HEK293 cells leads to the specific repression of reporter mRNAs bearing miRNA sites (Figures S3C–S3F). Next, using conditional AAVs, we expressed either miR-182/183 or miR-124 mimics specifically in C-DGCR-KO cones at P30. miR-182/183, but not miR-124, mimics prevented the loss of outer segments and cone opsins at P60 (Figures 3F–3H). Expression of miR-182/183 mimics in C-DGCR-KO mice did not increase the level of other tested miRNAs (Figure 3I), indicating that the availability of miR-182/183 was sufficient to maintain outer segments.

We investigated whether reexpression of miR-182/183 mimics can rescue outer segment loss and opsin expression in C-DGCR-KO cones. We administered AAVs expressing the miR-182/183 mimics at P60, i.e., after the loss of the outer segments. Inspection of mouse retinas at P90 indicated that outer segments were not restored (Figure S4A). Expression of Argonaute (AGO) proteins is often coregulated with the cellular availability of miRNAs (Martinez and Gregory, 2013), and we found that Argonaute levels were indeed strongly decreased in C-DGCR-KO mice at P60, when cones are depleted of miRNAs (Figure S4B). Since without Argonautes the miRNA mimics could not function, we attempted to regenerate outer segments by AAV-mediated coexpression of both miR-182/183 mimics and AGO2 at P60. Although this manipulation did not restore outer segments, it significantly increased opsin protein levels in the distal part of cones in AAV-infected C-DGCR-KO P90 retinas compared to controls (Figures S4C and S4D).

Depletion of miRNAs Leads to the Gradual Loss of the Genetic Identity of Cones

To gain a mechanistic insight into the altered molecular pathways that lead to outer segment loss and decreased opsin expression, we followed the dynamics of changes in miRNA and mRNA expression in cones between P30 and P90. We isolated cones from C-DGCR-KO and wild-type mice at five time points, P30, P40, P50, P60, and P90, and performed miRNA qPCR, next-generation RNA sequencing (RNA-seq), and mRNA array experi-

ments using RNA obtained from the isolated cones. We first confirmed that the levels of miRNAs gradually decreased in C-DGCR-KO cones, reaching 1%–3% of starting values at P90 (Figure 4A). As expected, the decrease in mature miRNAs was accompanied by an accumulation of respective pri-miRNAs (Figure 4B). Next, we followed mRNA expression in the same time window. Surprisingly, comparing gene expression at P30 and P60 in isolated C-DGCR-KO cones showed that 96.7% (RNA-seq; Figures 5A, S6A, and S6B) or 99.7% (mRNA arrays; Figure S5A) of expressed genes changed less than 2-fold; the vast majority of genes involved in regulation of apoptosis belonged to this category (Figures 5B and S5B). A small set of genes was, however, up- or downregulated more than 2-fold.

We first looked into the downregulated genes, unlikely to represent primary miRNA targets, which act as negative regulators of gene expression. To determine whether downregulated genes were members of known pathways, we performed molecular pathway analysis of these genes. This analysis identified the genes from the phototransduction pathway as significantly downregulated (Figures 5C, 5D, S5C, and S5D), whereas genes related to synaptic transmission were not affected significantly (Figures S6A–S6F). In order to get a dynamic picture of the changes, we plotted the expression of the phototransduction pathway genes as a function of time in C-DGCR-KO and wild-type mice from P30 to P90 (Figures 5C–5E and S5C–S5E). In C-DGCR-KO cones, several phototransduction genes followed the same time course: unchanged or even upregulated at P40 and decreasing gradually between P50 and P90. We then investigated whether the loss of DGCR8 influences cone-specific genes more generally. A recent screen identified cone-specific genes in adult mice in an unbiased way (Siebert et al., 2012), and we plotted the expression of these genes as a function of time in C-DGCR-KO and wild-type mice. Remarkably, a large fraction, 34% (RNA-seq) and 38% (mRNA array), of cone-specific genes had been significantly downregulated (Figures 5F–5H and S5F–S5H). The downregulation of cone-specific genes is highly significant, since any randomly selected similar number of genes showed no downregulation but a slight upregulation (Figures 5H and S5H). The decrease in expression followed two different time course patterns: most genes showed the same pattern as the five phototransduction genes, while a few genes decreased gradually from P30 to P90 (Figures 5F and S5F). The progression of the downregulation of most cone-specific genes was delayed compared to the start of outer segment loss (see Figures 2E and 2F), making it unlikely that the

(B) Top views of cone cell bodies stained for DGCR8 (blue, top row) and OPN1SW/MW-positive outer segments (green, bottom row) of WT (left), KO (middle), and DGCR8-rescue KO (right) mice.

(C) Quantification of immunostained OPN1SW/MW foci shown in (B).

(D) Mature miRNA profile (RNA-seq) of P60 WT cones.

(E) Conditional sh-miR AAV expression cassette driven by the CMV promoter. In the presence of Cre, the DNA segment flanked by loxP sites (triangles) is inverted, turning off the Tet repressor (TetR) and activating GFP expression. In the absence of TetR, sh-miRs are expressed from the H1-TetO2 promoter.

(F) Rescue of cone outer segments and opsin expression by sh-miR-183/182. Confocal side projections of OPN1SW/MW (green) merged with AAV-infected cones (yellow; left), merged with tdTomato-labeled cones (magenta; middle), and all channels merged (right). Sh-Control (top row), sh-miR-124 (middle row), and sh-miR-183/182 (bottom row) are shown. The dashed line indicates the location of outer segments (OS).

(G) Top views of OPN1SW/MW-positive outer segments (green) of sh-Control (left), sh-miR-124 (middle), and sh-miR-183/182 (right).

(H) Quantification of OPN1SW/MW foci shown in (G).

(I) qPCR measurement of selected mature miRNA levels from wild-type (white) and C-DGCR-KO cones, transfected with sh-miR-183/182 (gray) or sh-Control (black) AAVs (data from three biological replicates). Error bars, SEM. See also Figures S3 and S4.

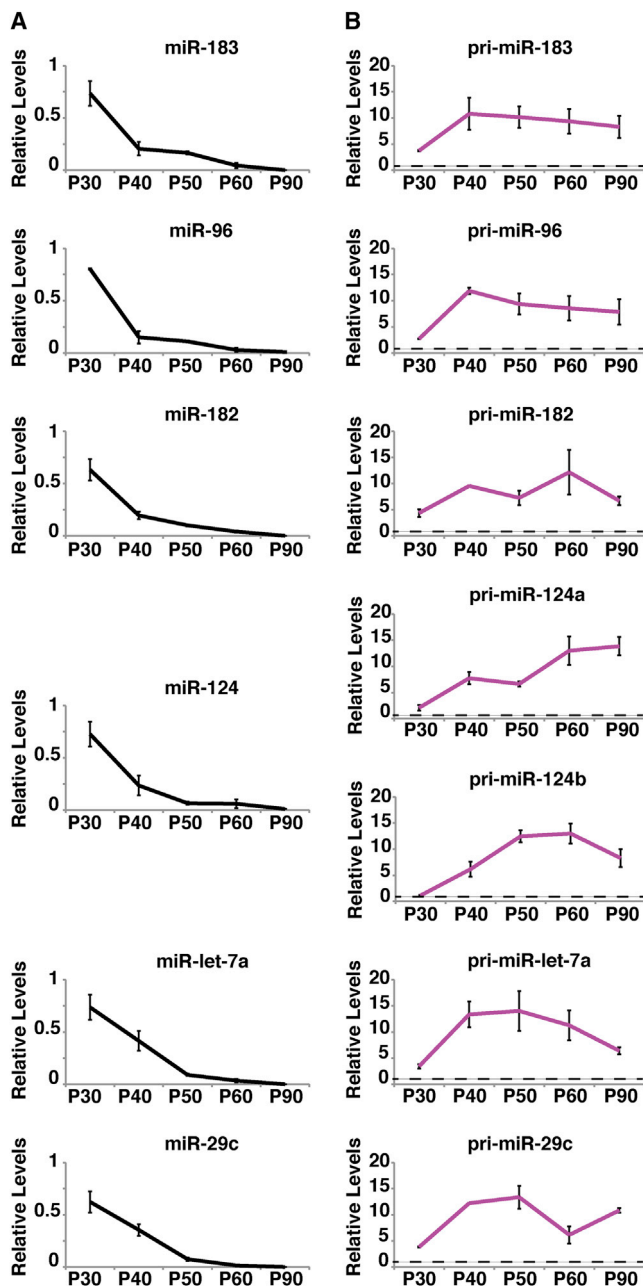


Figure 4. Mature miRNA Levels Gradually Decrease in C-DGCR-KO Cones

qPCR analysis of selected mature miRNAs (A) and pri-miRNAs (B) over time. C-DGCR-KO levels relative to wild-type levels from isolated cones are shown. The dashed line in (B) represents 1. Error bars, SEM (n = 3).

decreasing expression of these genes is the cause of outer segment loss. The downregulation could be a secondary effect caused by increased expression of genes normally controlled by miRNAs or directly by the Drosha/DGCR8 complex; alternatively, it could be a consequence of outer segment loss via a mechanism that regulates cone-specific gene expression depending on the length of cone outer segments.

To analyze the molecular pathways that can be directly regulated by miR-182 or miR-183 and that therefore cause the loss of outer segments, we first plotted the distribution of relative expression levels of the predicted miR-182 and miR-183 targets compared to levels at P30 (Figure S7A). As time progressed from P30 to P90, the relative distribution shifted gradually to the right, showing that the levels of predicted miR-182 and miR-183 targets progressively increased in C-DGCR-KO mice. In wild-type mice, the relative distribution did not change (Figure S7B). We then plotted the time course of the expression levels of individual genes, which are upregulated from P30 to P90 and are predicted to be targets of miR-182 (47 genes) or miR-183 (12 genes) (Figures 6A and 6B). We ordered these genes according to their fold change between P30 and P40, the time window in which the outer segments began to shorten. Among these upregulated and predicted target genes were those encoding components of intracellular membrane trafficking pathways (*Wasf2* [Yamashita et al., 2011], *Frmd4a* [Ikenouchi and Umeda, 2010], *Snap23* [Veale et al., 2011], *Cd2ap* [Kobayashi et al., 2004], *Vamp3* [Kwok et al., 2008], *Fcho2* [Henne et al., 2010]), one of which has been detected in outer segment proteomes (*Vamp3*), and others that lead to increased endocytosis (*Cd2ap*, *Fcho2*). Cilium (*Esy1* [Sang et al., 2011], *Kif19a* [Niwa et al., 2012], *Gnai3* [Ezan et al., 2013]), centrosome (*Tacc1* [Peset and Vernos, 2008], *Hook3* [Ge et al., 2010]), and microtubule (*Itgb1* [Lei et al., 2012]) associated genes, as well as cholesterol or lipid metabolism pathway genes (*Dhcr24* [Sarajärvi et al., 2009], *Insig1* [Yang et al., 2002], *Npc2* [Deffieu and Pfeffer, 2011]) were also detected. The presence of multiple genes related to membrane trafficking, lipid metabolism, and cilium formation indicate the complexity of the misregulated network (Figures 6C, S7C, and S7D).

miR-183/96/182 Cluster Induces the Formation of Short Outer Segments as Well as Light Responses In Vitro

To understand the effect of the miR-183/96/182 cluster expression on photoreceptor cells that have not yet developed distal structures such as inner segments, connecting cilia, and outer segments, we used an in vitro model system in which retinas are formed in 3D cultures of mouse ES cells (Eiraku et al., 2011). In these in-vitro-built retinas, no outer segments have been detected before (Gonzalez-Cordero et al., 2013). In control retinas, a well-separated photoreceptor layer, containing mostly rod-like cells, developed by day 25 (n = 5). At this stage, the miR-183/96/182 cluster miRNAs were expressed at a low level (Figures 7A and 7B), no distal photoreceptor structures were visible, and rhodopsin and peripherin (an outer segment protein [Kevany et al., 2013]) expression was low and confined to the cell bodies (Figure 7D). In agreement with previous work (Gonzalez-Cordero et al., 2013), we detected inner segments at day 35 (n = 7) (Figure 7F). Importantly, at day 35 the miR-183/96/182 cluster was expressed at a higher level. Rhodopsin and peripherin expression was also higher and was confined to the tip of the inner segments (Figures 7A and 7D). To find out whether there is a causal relationship between the miR-183/96/182 cluster expression and the formation of distal photoreceptor structures, we infected the retinal cultures (n = 9) at day 7 with the cluster-expressing AAVs (Figure 7C). At day 25, the miR-183/96/182 miRNAs had

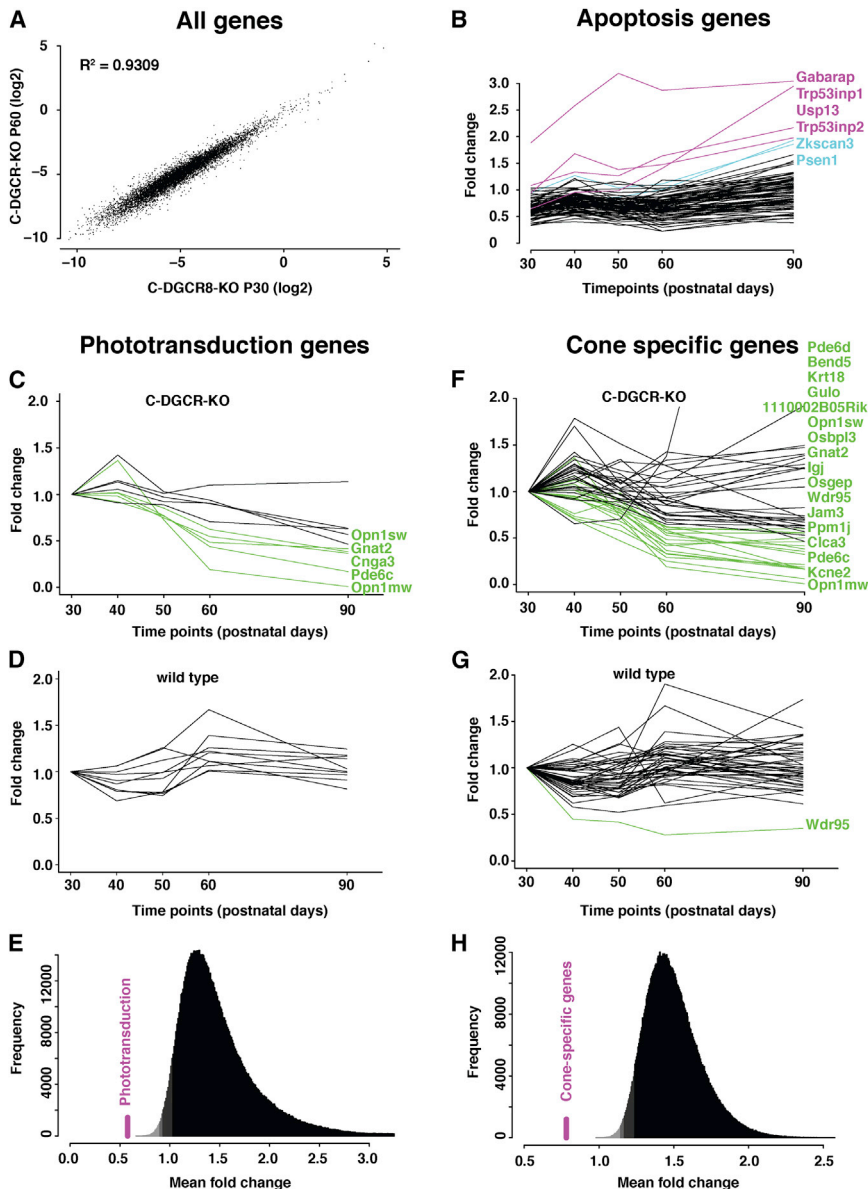


Figure 5. C-DGCR-KO Cones Lose Their Genetic Signature

(A) Scatterplot of expression levels comparing isolated C-DGCR-KO P60 with C-DGCR-KO P30 cones as measured by RNA-seq. Values are in log₂ scale.

(B) Expression of genes belonging to the Gene Ontology pathway “positive regulation of apoptotic process” over time for isolated C-DGCR-KO cone samples normalized to P30 wild-type. Fold changes over time were measured using RNA-seq data. Genes that were significantly upregulated at P90 only are shown in cyan, whereas those significantly upregulated at P60 and P90 are shown in magenta.

(C–E) RNA-seq analyses of cone phototransduction cascade genes expressed over time in isolated C-DGCR-KO (C) and WT (D) cones. Expression values are normalized to expression at P30. Significantly downregulated genes are highlighted in green. (E) Bootstrap fold change distribution at P60 in which the value for the phototransduction genes is highlighted in magenta. Confidence intervals (<0.05, <0.005, and <0.001) are shown in different shades of gray, with <0.001 with lightest gray. Note $p < 0.001$ values for phototransduction genes.

(F–H) RNA-seq analyses of cone-specific genes expressed over time in isolated C-DGCR-KO (F) and WT (G) cones. Expression values are normalized to expression at P30. Significantly downregulated genes are highlighted in green. (H) Bootstrap fold change distribution of cone-specific genes at P60. Note the $p < 0.001$ values for cone-specific genes. See also Figures S5 and S6.

accumulated at high levels (Figure 7A) and we observed a robust outgrowth of inner segments. Rhodopsin was expressed diffusely in the inner segments, and peripherin was localized to the tips of the inner segments (Figure 7D).

Next, we used a loss-of-function approach to find out whether the miR-183/96/182 miRNAs were necessary for formation of the inner segments and the rhodopsin/peripherin-positive foci that “naturally” appear on day 35. We used a miR-183/96/182-specific “triple sponge” construct (Figure 7E), which has previously been shown to effectively block miR-183/96/182 activity both in vivo and in vitro (Krol et al., 2010b). We infected retinal cultures ($n = 5$) at day 15 with AAVs expressing either the sponge or a control RNA under a rhodopsin promoter. At day 35, no distal photoreceptor structures were observed in retinal cultures infected with the miR-183/96/182 sponge AAVs, in contrast to

controls (Figure 7F). Taken together, these experiments suggest that miRNAs of the miR-183/96/182 cluster are necessary and sufficient for the formation of distal photoreceptor structures in ES-cell-derived retinal cultures. Does the miR-183/96/182 cluster induce outer segment formation and light responses? At day 25, we examined in more detail the distal structures of retinal cultures that were induced by expression of the cluster miRNAs, using 3D EM reconstruction. We found inner segments filled with mitochondria, as well as long connecting cilia. We also detected a small region at the tip of the connecting cilia with electron-dense material. Using high-resolution EM techniques (Supplemental Experimental Procedures), we found that this electron-dense material contained a stack of membrane disks, which are the characteristic structures of normal photoreceptor outer segments (Figure 8A). Outer segments were not detected in control retinal cultures. To test whether the short outer segments induced by miR-183/96/182 cluster expression are capable of mediating light responses, we recorded from photoreceptors of the miR-183/96/182-transduced and control ES-cell-derived cultures using whole-cell patch clamp and stimulated the

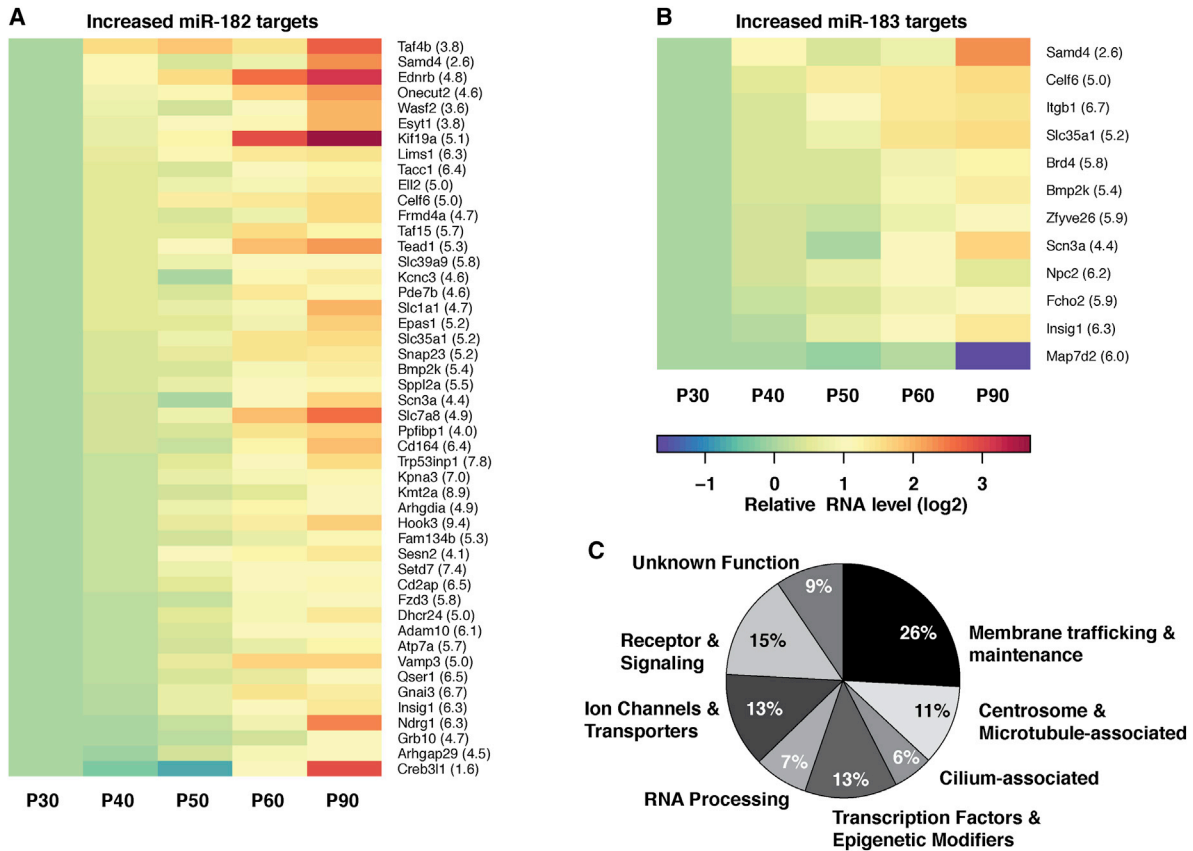


Figure 6. Increased Expression Levels of miR-182 and miR-183 Target Genes in C-DGCR-KO Cones

(A and B) Heat maps showing significantly ($p < 0.05$) increased miR-182 (A) and miR-183 (B) target genes, ranked by highest fold increase in log₂ scale between P30 and P40. Fold increase in log₂ scale is indicated in brackets. The numbers following gene symbols correspond to the log₂ number of counts per gene per million reads in the library at P30.

(C) Summary of miR-182 and miR-183 targets grouped by cellular functions. See also [Figure S7](#).

cultures with light ([Figures 8B and 8C](#)). We recorded light-evoked hyperpolarizing responses in miR-183/96/182-transduced cultures ($n = 7$) in a large fraction of the recorded cells (29%, 7/24). None of the cells in control cultures responded to light. In conclusion, the miR-183/96/182 cluster induces the formation of short outer segments in ES-cell-derived retinal cultures, which generate light responses with a polarity, hyperpolarization, that matches the response polarity of normal vertebrate photoreceptors.

DISCUSSION

Using an *in vivo* model system that we set up to study the role of miRNAs in mature cones, we found that the depletion of miRNAs, resulting from the knockout of DGCR8 in adult cones, led to the loss of outer segments. The outer segment loss was prevented by reexpression of miR-182 and miR-183, suggesting that these miRNA species are important for the maintenance of outer segments. We cannot rule out that other miRNA species may also contribute to this process since overexpressed miR-182/183 may functionally compensate for the loss of these other miRNAs. However, miR-182/183 consti-

tutes 68% of all cone miRNAs, and therefore it is likely that miR-182/183 is a major factor responsible for outer segment maintenance.

The observed phenotype in C-DGCR-KO mice was distinct from the ones reported in previous studies in which the genetic perturbation of specific miRNAs was established during development. We found a gradual loss of outer segments as the miRNA levels decreased between P30 and P60, without any change in the number of cones or any systematic increase in proapoptotic gene expression. Although it is possible that cones degenerate at later times, our data demonstrate that the loss of the outer segment is not caused by an apoptotic process but is controlled independently. Interestingly, a pronounced phenotype caused by the loss of the miR-183/96/182 cluster during development is a defect at the synapses and the alteration of genes related to synaptogenesis and synaptic contacts ([Lumayag et al., 2013](#)). We have not found a significant systematic alteration in gene expression related to synapses, even at P90, when comparing C-DGCR8-KO and wild-type animals, suggesting that this aspect of the miR-183/96/182-mediated regulation may occur during development.

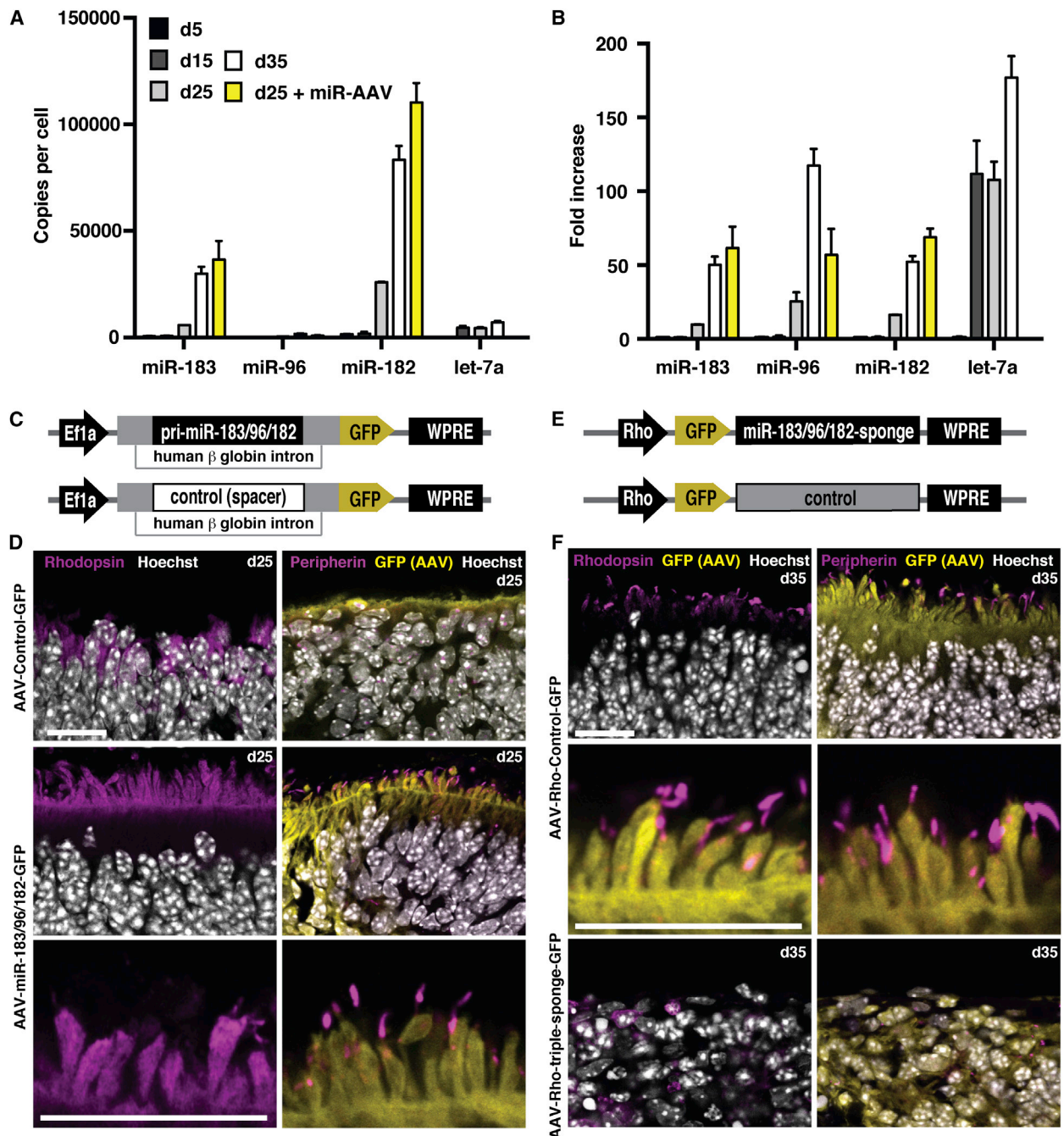


Figure 7. miRNAs of the miR-183/96/182 Cluster Are Necessary and Sufficient for the Formation of Distal Photoreceptor Structures in ES-Cell-Derived Retinal Cultures

(A and B) Bar charts showing the copies per cell (A) and fold increases (B) of indicated miRNAs relative to day 5 (d5) ES-cell-derived retinal cultures at different time points as measured by qPCR (data from three biological replicates). Samples infected at d7 with AAVs overexpressing the miR-183/96/182 cluster are shown in yellow.

(C) AAV-based miR-183/96/182 and control expression cassettes driven by the elongation factor 1 α (Ef1 α) promoter. The pri-miRNA precursors or a control spacer sequence were inserted into the human β globin intron upstream of a GFP.

(D) The microscope images show upper parts of the photoreceptor layer of ES-cell-derived retinas. Sections at d25 of culture following infection at d7 treated with either control AAV-expressing GFP (top row) or AAV-expressing GFP and miR-182/96/183 (middle row) are shown. Zoomed images of distal photoreceptor structures of retinas infected with GFP- and miR-183/96/182-expressing AAV are shown at the bottom. Rhodopsin (magenta, left), peripherin (magenta, right), and GFP (yellow, right) immunostainings are shown. Cell nuclei are labeled with Hoechst (white). Scale bars, 20 μ m.

(E) AAV-based miR-183/96/182 sponge (triple sponge) and control cassettes driven by the human Rhodopsin (Rho) promoter. The sponge and control sequences were inserted in the 3' untranslated region of a GFP reporter gene.

(legend continued on next page)

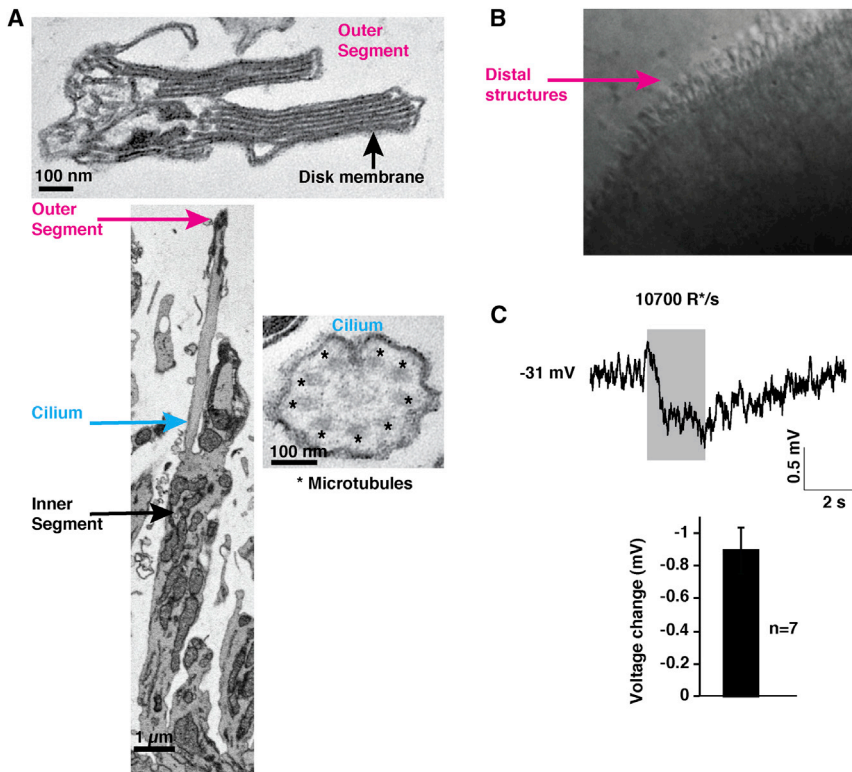


Figure 8. miR-183/96/182 Cluster Induces the Formation of Short Outer Segments as Well as Light Responses in ES-Cell-Derived Retinal Cultures

(A) Representative EM images of distal structures in the d25 ES-cell-derived retina culture that was infected at d7 with AAV expressing pri-miR-183/96/182. Top picture shows an enlarged EM image of a short outer segment including disk membranes. A longitudinal section of an entire inner segment, connecting cilium and outer segment (bottom left) and a cross-section of the connecting cilium (bottom right), are also shown, with asterisks highlighting the nine microtubule bundles. Scale bars are as indicated.

(B) Infrared image of a slice of an ES-cell-derived retinal culture.

(C) An example of a hyperpolarizing response from a recorded photoreceptor in response to full-field light stimulation. The gray bar indicates the timing of the stimulation (top). Quantification of peak responses (bottom). Error bar, SEM.

Previous work has identified a decrease in expression of some cone phototransduction genes, such as *Arr3* and *Opn1mw*, in the miR-183/96/182 cluster knockout animals (Lumayag et al., 2013). Similarly, we found that expression of these and other phototransduction genes decreased between P30 and P60. Interestingly, the decrease was not limited to the phototransduction cascade genes but also applied to many other genes known to be specifically expressed in cones (Siegert et al., 2012). Therefore, it appears that in the absence of miR-182 and miR-183, cones largely lose their genetic signature, i.e., the expression of cell-type-specific genes. This change in gene expression was delayed compared to the shortening of outer segments, and it is therefore unlikely that the outer segment loss is due to the aforementioned general decrease in cone-specific gene expression. It is possible that the loss of outer segments induces a feedback signal to the nucleus that reduces the expression of cone-specific genes. Alternatively, these two phenotypes are independent of each other.

Using an in vitro model system, stem-cell-derived retinal cultures, we found that the miR-183/96/182 cluster miRNAs were necessary and sufficient for the formation of inner segments, connecting cilia and short outer segments, as well as light-induced hyperpolarization. These retinal cultures were grown in the absence of retinal pigment epithelium (RPE), suggesting

and the model system presented here, namely the retinal culture in combination with an AAV expressing the miR-183/96/182 cluster, will allow future mechanistic investigations of both outer segment formation and, when applied to ES cells modified to model retinal diseases, outer segment pathology.

The miR-183/96/182 cluster is needed for the maintenance of cone outer segments in vivo, and for the formation of inner segments, connecting cilia, and outer segments in a developing retina culture model in vitro. Both of these functions could be explained if the effect of the cluster miRNAs is to optimize the supply of molecular components for the assembly of distal photoreceptor structures. The outer segments of both rods and cones are dynamically maintained in adults: the pigment epithelial cells phagocytize the distal membrane disks, and the proximal disks are continuously renewed by the photoreceptors. In adult C-DGCR8-KO cones, a reduced supply of essential outer segment components would lead to an imbalance between the pace of phagocytosis at the distal tip and the formation of new outer segment membrane and protein components at the base of the outer segment. The continued phagocytosis and sub-optimal regeneration would lead to a shortening of the outer segments. Similarly, in the photoreceptors developing in vitro, miRNAs of the miR-183/96/182 cluster might control the supply of components to the apical membrane, accelerating the

(F) Sections of the ES-cell-derived retinas at d35 in culture, following infection with control GFP-expressing AAV at d15 (top row); zoomed images of GFP-labeled distal photoreceptor structures are in a middle row. Sections of the ES-cell-derived retinas at d35 in culture, following infections at d15 with AAV-expressing GFP and miR-183/96/182 sponge (bottom row). $n = 5$ retinas for each investigated condition. Photoreceptors are labeled for rhodopsin (magenta, left), peripherin (magenta, right), and GFP (yellow), using specific antibodies. Cell nuclei are labeled with Hoechst (white). Scale bars, 20 μm . Error bars, SEM.

formation of distal structures. Among the upregulated and predicted targets of miR-182 and miR-183 were many genes involved in membrane trafficking, lipid metabolism, and cilium formation pathways. To explain the shortening of the outer segments, one would predict an overall decrease or misregulation in membrane flow toward the distal tip of cones. The increased expression of genes encoding proteins that activate endocytosis provides a possible explanation of a deficiency in membrane flow.

The miR-183/96/182 cluster is also expressed in other sensory organs, not just the retina (Xu et al., 2007). In hair cells of the inner ear, the miR-183/96/182 cluster miRNAs are expressed in a gradient: high on the apical side and low on the basal side of the cochlea (Groves et al., 2013; Soukup, 2009). Correlating with this miRNA gradient, the distal structures of hair cells, including the cilium bundle, are longer on the apical than the basal side, and in the Dicer knockout mouse model the residual miR-183/96/182 cluster expression correlates with the extent of hair bundle length (Soukup, 2009). Therefore the “increased supply” mechanism proposed above for retinal photoreceptors may also apply to hair cells.

The loss of cone outer segments is a common outcome for a number of retinal diseases and can lead to blindness. The finding that miR-183/96/182 cluster expression leads to the induction of outer segments in ES-cell-derived retinal cultures, and that the same cluster is downregulated in several mouse models of the blinding disease retinitis pigmentosa (Loscher et al., 2008), suggests that reexpression of these miRNAs, either alone or in combination with other factors that keep cones alive (Léveillard and Sahel, 2010; Punzo et al., 2009; Wen et al., 2012), could be a potential strategy for outer segment regeneration.

EXPERIMENTAL PROCEDURES

Animals

All animal experiments and procedures were approved by the Swiss Veterinary Office. The animals were maintained under a 12 hr light-dark cycle. Conditional DGCR8 knockout mice (Yi et al., 2009) were crossed to the cone photoreceptor-specific Cre recombinase driver line D4-cre (Le et al., 2004), resulting in C-DGCR-KO mice. In D4-Cre line the human red/green opsin promoter drives expression of Cre in cones. To visualize cones, we further crossed C-DGCR-KO mice to the floxed tdTomato reporter line Ai9 (Madisen et al., 2010) (JAX mice B6.Cg-Gt(ROSA)26Sor^{tm9(CAG-tdTomato)Hze}/J, Stock Number 007909, Jackson Laboratory). D4-cre or D4-cre/Ai9 animals served as wild-type controls.

ES-Cell-Derived Retina-like Structure Formation

The retina-like structures from ES cells were generated as previously described (Eiraku and Sasai, 2012; Eiraku et al., 2011).

Subretinal AAV Delivery

The injection of viral particles was performed as previously described (Busskamp et al., 2010).

Statistical Analysis.

The nonparametric Mann-Whitney U test was used to compare data. Significance levels are indicated by * for $p < 0.05$, ** for $p < 0.01$, and *** for $p < 0.001$. n.s. (not significant) means $p \geq 0.05$. The error bars and \pm values represent SEM.

Additional information about Experimental Procedures can be found in the Supplemental Experimental Procedures and Table S1. External links to

RNA-seq and Gene Array data as well as serial block-face scanning electron microscopy image stacks are included in the Supplemental Information.

SUPPLEMENTAL INFORMATION

Supplemental Information includes Supplemental Experimental Procedures, seven figures, and one table and can be found with this article online at <http://dx.doi.org/10.1016/j.neuron.2014.06.020>.

AUTHOR CONTRIBUTIONS

V.B. observed the loss of outer segment phenotype in DGCR8 KO mice. J.K. designed the DGCR8-independent miRNA mimics, collected cells for RNA sequencing and array experiments, performed western blots, and performed ES-cell-based retina experiments. V.B. and J.K. designed AAVs, performed injections, qPCR, and immunohistochemistry, analyzed data, designed experiments, and wrote the manuscript. D.N. and J.D. performed immunohistochemistry, B.T. analyzed RNA sequencing and microarray data, J.J. designed and made AAVs, K.F. performed patch-clamp recordings, B.G.S. made and analyzed ES-cell-derived retinas, C.P.P.A. made ES-cell-derived retinas, C.G. and J.D. performed electron microscopy experiments, V.S. and N.T. performed electroretinogram experiments, M. Stadler analyzed RNA sequencing and microarray data, M. Seeliger designed electroretinogram experiments, M. Stoffel provided DGCR8 KO mice, and T.S.Z. performed electrophysiological recordings from stem-cell-derived retinas. W.F. designed experiments and wrote the manuscript, B.R. analyzed data, designed experiments, and wrote the manuscript.

ACKNOWLEDGMENTS

We thank Sabrina Djaffer, Gudrun Utz, and Pia Lacroix for technical support, Tim Roloff, Kirsten Jacobeit, and Stephane Thiry for help with microarrays and deep sequencing, Hubertus Kohler for cell sorting, and Laurent Gelman, Steven Bourke, and Moritz Kirschmann for help with microscopy. We thank Sara Oakeley for commenting on the manuscript. We thank V. Narry Kim for providing a DGCR8 antibody, and Mike O. Karl and Budd A. Tucker for advice about growing ES-cell-derived retinal cultures. We acknowledge the following grants: HFSP and SNSF fellowship to V.B., SNSF Ambizione fellowship to J.K., EC Sirocco Network to W.F., and Gebert-Ruf Foundation, SNSF, ERC, NCCR Molecular Systems Engineering, EU SEEBETTER, TREATRUSH, OPTONEURO and 3X3D Imaging grants to B.R. M. Stoffel is a member of the SAB of Regulus Therapeutics. B.R. is a member of the SAB of GenSight.

Accepted: June 19, 2014

Published: July 3, 2014

REFERENCES

- Atasoy, D., Aponte, Y., Su, H.H., and Sternson, S.M. (2008). A FLEX switch targets Channelrhodopsin-2 to multiple cell types for imaging and long-range circuit mapping. *J. Neurosci.* 28, 7025–7030.
- Busskamp, V., Duebel, J., Balya, D., Fradot, M., Viney, T.J., Siebert, S., Groner, A.C., Cabuy, E., Forster, V., Seeliger, M., et al. (2010). Genetic reactivation of cone photoreceptors restores visual responses in retinitis pigmentosa. *Science* 329, 413–417.
- Carter-Dawson, L.D., and LaVail, M.M. (1979). Rods and cones in the mouse retina. I. Structural analysis using light and electron microscopy. *J. Comp. Neurol.* 188, 245–262.
- Cheng, T.-L., Wang, Z., Liao, Q., Zhu, Y., Zhou, W.-H., Xu, W., and Qiu, Z. (2014). MeCP2 suppresses nuclear microRNA processing and dendritic growth by regulating the DGCR8/Drosha complex. *Dev. Cell* 28, 547–560.
- Damiani, D., Alexander, J.J., O'Rourke, J.R., McManus, M., Jadhav, A.P., Cepko, C.L., Hauswirth, W.W., Harfe, B.D., and Strettoi, E. (2008). Dicer inactivation leads to progressive functional and structural degeneration of the mouse retina. *J. Neurosci.* 28, 4878–4887.

- Deffieux, M.S., and Pfeffer, S.R. (2011). Niemann-Pick type C 1 function requires luminal domain residues that mediate cholesterol-dependent NPC2 binding. *Proc. Natl. Acad. Sci. USA* *108*, 18932–18936.
- Denk, W., and Horstmann, H. (2004). Serial block-face scanning electron microscopy to reconstruct three-dimensional tissue nanostructure. *PLoS Biol.* *2*, e329.
- Eiraku, M., and Sasai, Y. (2012). Mouse embryonic stem cell culture for generation of three-dimensional retinal and cortical tissues. *Nat. Protoc.* *7*, 69–79.
- Eiraku, M., Takata, N., Ishibashi, H., Kawada, M., Sakakura, E., Okuda, S., Sekiguchi, K., Adachi, T., and Sasai, Y. (2011). Self-organizing optic-cup morphogenesis in three-dimensional culture. *Nature* *472*, 51–56.
- Ezan, J., Lasvaux, L., Gezer, A., Novakovic, A., May-Simera, H., Belotti, E., Lhoumeau, A.-C., Birnbaumer, L., Beer-Hammer, S., Borg, J.-P., et al. (2013). Primary cilium migration depends on G-protein signalling control of subapical cytoskeleton. *Nat. Cell Biol.* *15*, 1107–1115.
- Ge, X., Frank, C.L., Calderon de Anda, F., and Tsai, L.-H. (2010). Hook3 interacts with PCM1 to regulate pericentriolar material assembly and the timing of neurogenesis. *Neuron* *65*, 191–203.
- Gonzalez-Cordero, A., West, E.L., Pearson, R.A., Duran, Y., Carvalho, L.S., Chu, C.J., Naeem, A., Blackford, S.J.I., Georgiadis, A., Lakowski, J., et al. (2013). Photoreceptor precursors derived from three-dimensional embryonic stem cell cultures integrate and mature within adult degenerate retina. *Nat. Biotechnol.* *31*, 741–747.
- Groves, A.K., Zhang, K.D., and Fekete, D.M. (2013). The genetics of hair cell development and regeneration. *Annu. Rev. Neurosci.* *36*, 361–381.
- Han, J., Pedersen, J.S., Kwon, S.C., Belair, C.D., Kim, Y.-K., Yeom, K.-H., Yang, W.-Y., Haussler, D., Belloch, R., and Kim, V.N. (2009). Posttranscriptional cross-regulation between Drosophila and DGC8. *Cell* *136*, 75–84.
- Henne, W.M., Boucrot, E., Meinecke, M., Evergren, E., Vallis, Y., Mittal, R., and McMahon, H.T. (2010). FCHO proteins are nucleators of clathrin-mediated endocytosis. *Science* *328*, 1281–1284.
- Herbert, K.M., Pimienta, G., DeGregorio, S.J., Alexandrov, A., and Steitz, J.A. (2013). Phosphorylation of DGCR8 increases its intracellular stability and induces a progrowth miRNA profile. *Cell Rep.* *5*, 1070–1081.
- Ikenouchi, J., and Umeda, M. (2010). FRMD4A regulates epithelial polarity by connecting Arf6 activation with the PAR complex. *Proc. Natl. Acad. Sci. USA* *107*, 748–753.
- Jin, Z.-B., Hirokawa, G., Gui, L., Takahashi, R., Osakada, F., Hiura, Y., Takahashi, M., Yasuhara, O., and Iwai, N. (2009). Targeted deletion of miR-182, an abundant retinal microRNA. *Mol. Vis.* *15*, 523–533.
- Karali, M., Peluso, I., Marigo, V., and Banfi, S. (2007). Identification and characterization of microRNAs expressed in the mouse eye. *Invest. Ophthalmol. Vis. Sci.* *48*, 509–515.
- Kevany, B.M., Tsybovsky, Y., Campuzano, I.D.G., Schnier, P.D., Engel, A., and Palczewski, K. (2013). Structural and functional analysis of the native peripherin-ROM1 complex isolated from photoreceptor cells. *J. Biol. Chem.* *288*, 36272–36284.
- Kobayashi, S., Sawano, A., Nojima, Y., Shibuya, M., and Maru, Y. (2004). The c-Cbl/CD2AP complex regulates VEGF-induced endocytosis and degradation of Flt-1 (VEGFR-1). *FASEB J.* *18*, 929–931.
- Krol, J., Loedige, I., and Filipowicz, W. (2010a). The widespread regulation of microRNA biogenesis, function and decay. *Nat. Rev. Genet.* *11*, 597–610.
- Krol, J., Busskamp, V., Markiewicz, I., Stadler, M.B., Ribi, S., Richter, J., Duebel, J., Bicker, S., Fehling, H.J., Schübeler, D., et al. (2010b). Characterizing light-regulated retinal microRNAs reveals rapid turnover as a common property of neuronal microRNAs. *Cell* *141*, 618–631.
- Kwok, M.C.M., Holopainen, J.M., Molday, L.L., Foster, L.J., and Molday, R.S. (2008). Proteomics of photoreceptor outer segments identifies a subset of SNARE and Rab proteins implicated in membrane vesicle trafficking and fusion. *Mol. Cell. Proteomics* *7*, 1053–1066.
- Le, Y.-Z., Ash, J.D., Al-Ubaidi, M.R., Chen, Y., Ma, J.-X., and Anderson, R.E. (2004). Targeted expression of Cre recombinase to cone photoreceptors in transgenic mice. *Mol. Vis.* *10*, 1011–1018.
- Lei, W.-L., Xing, S.-G., Deng, C.-Y., Ju, X.-C., Jiang, X.-Y., and Luo, Z.-G. (2012). Laminin/ β 1 integrin signal triggers axon formation by promoting microtubule assembly and stabilization. *Cell Res.* *22*, 954–972.
- Léveillard, T., and Sahel, J.-A. (2010). Rod-derived cone viability factor for treating blinding diseases: from clinic to redox signaling. *Sci. Transl. Med.* *2*, 26ps16.
- Loscher, C.J., Hokamp, K., Wilson, J.H., Li, T., Humphries, P., Farrar, G.J., and Palfi, A. (2008). A common microRNA signature in mouse models of retinal degeneration. *Exp. Eye Res.* *87*, 529–534.
- Lumayag, S., Haldin, C.E., Corbett, N.J., Wahlin, K.J., Cowan, C., Turturro, S., Larsen, P.E., Kovacs, B., Witmer, P.D., Valle, D., et al. (2013). Inactivation of the microRNA-183/96/182 cluster results in syndromic retinal degeneration. *Proc. Natl. Acad. Sci. USA* *110*, E507–E516.
- Macias, S., Plass, M., Stajuda, A., Michlewski, G., Eyras, E., and Cáceres, J.F. (2012). DGCR8 HITS-CLIP reveals novel functions for the Microprocessor. *Nat. Struct. Mol. Biol.* *19*, 760–766.
- Madisen, L., Zwingman, T.A., Sunkin, S.M., Oh, S.W., Zariwala, H.A., Gu, H., Ng, L.L., Palmiter, R.D., Hawrylycz, M.J., Jones, A.R., et al. (2010). A robust and high-throughput Cre reporting and characterization system for the whole mouse brain. *Nat. Neurosci.* *13*, 133–140.
- Martinez, N.J., and Gregory, R.I. (2013). Argonaute2 expression is post-transcriptionally coupled to microRNA abundance. *RNA* *19*, 605–612.
- Mustafi, D., Engel, A.H., and Palczewski, K. (2009). Structure of cone photoreceptors. *Prog. Retin. Eye Res.* *28*, 289–302.
- Niwa, S., Nakajima, K., Miki, H., Minato, Y., Wang, D., and Hirokawa, N. (2012). KIF19A is a microtubule-depolymerizing kinesin for ciliary length control. *Dev. Cell* *23*, 1167–1175.
- Pearring, J.N., Salinas, R.Y., Baker, S.A., and Arshavsky, V.Y. (2013). Protein sorting, targeting and trafficking in photoreceptor cells. *Prog. Retin. Eye Res.* *36*, 24–51.
- Peset, I., and Vernos, I. (2008). The TACC proteins: TACC-ling microtubule dynamics and centrosome function. *Trends Cell Biol.* *18*, 379–388.
- Punzo, C., Kornacker, K., and Cepko, C.L. (2009). Stimulation of the insulin/mTOR pathway delays cone death in a mouse model of retinitis pigmentosa. *Nat. Neurosci.* *12*, 44–52.
- Ryan, D.G., Oliveira-Fernandes, M., and Lavker, R.M. (2006). MicroRNAs of the mammalian eye display distinct and overlapping tissue specificity. *Mol. Vis.* *12*, 1175–1184.
- Sahel, J.-A., and Roska, B. (2013). Gene therapy for blindness. *Annu. Rev. Neurosci.* *36*, 467–488.
- Sang, L., Miller, J.J., Corbit, K.C., Giles, R.H., Brauer, M.J., Otto, E.A., Baye, L.M., Wen, X., Scales, S.J., Kwong, M., et al. (2011). Mapping the NPHP-JBTS-MKS protein network reveals ciliopathy disease genes and pathways. *Cell* *145*, 513–528.
- Sanuki, R., Onishi, A., Koike, C., Muramatsu, R., Watanabe, S., Muranishi, Y., Irie, S., Uneo, S., Koyasu, T., Matsui, R., et al. (2011). miR-124a is required for hippocampal axogenesis and retinal cone survival through Lhx2 suppression. *Nat. Neurosci.* *14*, 1125–1134.
- Sarajärvi, T., Haapasalo, A., Viswanathan, J., Mäkinen, P., Laitinen, M., Soininen, H., and Hiltunen, M. (2009). Down-regulation of seladin-1 increases BACE1 levels and activity through enhanced GGA3 depletion during apoptosis. *J. Biol. Chem.* *284*, 34433–34443.
- Siegert, S., Cabuy, E., Scherf, B.G., Kohler, H., Panda, S., Le, Y.-Z., Fehling, H.J., Gaidatzis, D., Stadler, M.B., and Roska, B. (2012). Transcriptional code and disease map for adult retinal cell types. *Nat. Neurosci.* *15*, 487–495, S1–S2.
- Solovei, I., Kreysing, M., Lanctôt, C., Kösem, S., Peichl, L., Cremer, T., Guck, J., and Joffe, B. (2009). Nuclear architecture of rod photoreceptor cells adapts to vision in mammalian evolution. *Cell* *137*, 356–368.
- Soukup, G.A. (2009). Little but loud: small RNAs have a resounding affect on ear development. *Brain Res.* *1277*, 104–114.

- Sundermeier, T.R., and Palczewski, K. (2012). The physiological impact of microRNA gene regulation in the retina. *Cell. Mol. Life Sci.* 69, 2739–2750.
- Thompson, S., Blodi, F.R., Lee, S., Welder, C.R., Mullins, R.F., Tucker, B.A., Stasheff, S.F., and Stone, E.M. (2014). Photoreceptor cells with profound structural deficits can support useful vision in mice. *Invest. Ophthalmol. Vis. Sci.* 55, 1859–1866.
- Veale, K.J., Offenhäuser, C., Lei, N., Stanley, A.C., Stow, J.L., and Murray, R.Z. (2011). VAMP3 regulates podosome organisation in macrophages and together with Stx4/SNAP23 mediates adhesion, cell spreading and persistent migration. *Exp. Cell Res.* 317, 1817–1829.
- Wen, R., Tao, W., Luo, L., Huang, D., Kauper, K., Stabila, P., LaVail, M.M., Laties, A.M., and Li, Y. (2012). Regeneration of cone outer segments induced by CNTF. *Adv. Exp. Med. Biol.* 723, 93–99.
- Xu, S., Witmer, P.D., Lumayag, S., Kovacs, B., and Valle, D. (2007). MicroRNA (miRNA) transcriptome of mouse retina and identification of a sensory organ-specific miRNA cluster. *J. Biol. Chem.* 282, 25053–25066.
- Yamashita, H., Ueda, K., and Kioka, N. (2011). WAVE2 forms a complex with PKA and is involved in PKA enhancement of membrane protrusions. *J. Biol. Chem.* 286, 3907–3914.
- Yang, T., Espenshade, P.J., Wright, M.E., Yabe, D., Gong, Y., Aebersold, R., Goldstein, J.L., and Brown, M.S. (2002). Crucial step in cholesterol homeostasis: sterols promote binding of SCAP to INSIG-1, a membrane protein that facilitates retention of SREBPs in ER. *Cell* 110, 489–500.
- Yi, R., Pasolli, H.A., Landthaler, M., Hafner, M., Ojo, T., Sheridan, R., Sander, C., O'Carroll, D., Stoffel, M., Tuschl, T., and Fuchs, E. (2009). DGCR8-dependent microRNA biogenesis is essential for skin development. *Proc. Natl. Acad. Sci. USA* 106, 498–502.
- Zhu, Q., Sun, W., Okano, K., Chen, Y., Zhang, N., Maeda, T., and Palczewski, K. (2011). Sponge transgenic mouse model reveals important roles for the microRNA-183 (miR-183)/96/182 cluster in postmitotic photoreceptors of the retina. *J. Biol. Chem.* 286, 31749–31760.